# LOCALIZED EXCITATION FLUORESCENCE IMAGING (LEFI)

Matthias Colin Hofmann

A dissertation submitted to the faculty of the
Virginia Polytechnic Institute and State University
in partial fulfillment of the requirements for the degree of

Doctor of Philosophy

in

Electrical Engineering

Yong Xu, Chair
Anbo Wang
William Baumann
Ge Wang
Shay Soker

May 4, 2012
Blacksburg, VA

Keywords: Deep Tissue Imaging, Blood Vessel, Fiber Optics

# Localized Excitation Fluorescence Imaging (LEFI)

Matthias Colin Hofmann

(ABSTRACT)

A major limitation in tissue engineering is the lack of nondestructive methods to assess the development of tissue scaffolds undergoing preconditioning in bioreactors. Due to significant optical scattering in most scaffolding materials, current microscope-based imaging methods cannot "see" through thick and optically opaque tissue constructs. To address this deficiency, we developed a scanning fiber imaging method capable of nondestructive imaging of fluorescently labeled cells through a thick and optically opaque vascular scaffold, contained in a bioreactor. This imaging modality is based on local excitation of fluorescent cells, acquisition of fluorescence through the scaffold, and fluorescence mapping based on the position of the excitation light. To evaluate the capability and accuracy of the imaging system, human endothelial cells, stably expressing green fluorescent protein (GFP), were imaged through a fibrous scaffold. Without sacrificing the scaffolds, we nondestructively visualized the distribution of GFP-labeled endothelial cells on the luminal surface through a ~500 μm thick tubular scaffold at cell-level resolutions and distinct localization. These results were similar to control images obtained using an optical microscope with direct line-of-sight access. Through a detailed quantitative analysis, we demonstrated that this method achieved a resolution of the order of 20-30 μm, with 10% or less deviation from standard optical microscopy. Furthermore, we demonstrated that the penetration depth of the imaging method exceeded that of confocal laser scanning microscopy by more than a factor of 2. Our imaging method also possesses a working distance (up to 8 cm) much longer than that of a standard confocal microscopy system, which can significantly facilitate bioreactor integration. This method will enable nondestructive monitoring of endothelial cells seeded on the lumen of a tissue-engineered vascular graft during preconditioning *in vitro*, as well as for other tissue-engineered constructs in the future.

# Contents

# List of Figures

# Chapter 1

# Introduction

Tissue engineering (TE) aims to develop functional tissues and organs to replace or restore those damaged by disease and trauma [1, 2, 3, 4]. In recent years, a bottom-up approach to tissue design has become increasingly popular, where custom-fabricated scaffolds are combined with appropriate cells and bioactive molecules to emulate the structure and function of the target tissue [5][6]. The *in vivo* success or failure of such engineered tissues depends on the critical *in vitro* preconditioning phase during which seeded cells can proliferate, differentiate towards a specific phenotype, and deposit native extracellular matrices. Specialized bioreactors are often utilized during preconditioning to provide the necessary mechanical and biochemical stimuli to cell-seeded constructs to enhance tissue development (i.e. cellularity, cell differentiation, protein expression and organization, etc.) prior to implantation [7, 8, 9].

Optimizing the preconditioning phase is often a challenging and time consuming process during which a cell-seeded construct must be assessed periodically with regards to the progress of tissue development. Conventional scaffold assessment methods typically require removal of the sample from the bioreactor followed by fixation, histological sectioning, and staining at a given time point. This method, however, destroys the sample and can only provide "snapshots" of tissue development at a limited number of time points [10][11]. This inefficiency severely limits our understanding of the biological processes associated with tissue growth during the *in vitro* preconditioning phase and is resource and time-intensive.

Due to the aforementioned limitations, researchers have begun developing alternative nondestructive methods for assessing tissue development [12]. Often times, the region of interest (ROI) is

subjected within the specimen or is obstructed by thick and opaque tissue requiring the use of a deep-tissue imaging method. Accomplishing high resolution, deep-tissue, imaging is a difficult challenge that goes far beyond tissue engineering. In fact, a major problem in biophotonics is the conflict between imaging depth and imaging resolution. The difficulty in simultaneously achieving a high imaging resolution and a large imaging depth can be traced to this observation: Most biological tissues are turbid media and therefore strongly scatter light. Consequently, current microscope-based methods for nondestructive tissue assessment remain constrained by two major drawbacks: a limited imaging depth and a short working distance.

The main focus of this study is to develop a an imaging method based on fiber optics that can significantly extend the depth of cell-level resolution imaging as well as greatly improve the working distance of the imaging system. In particular, we focus on developing a novel imaging method to evaluate bioengineered vascular grafts, where the assessment endothelialization on the lumen (inner surface) of synthetic bioengineered blood vessels is of significant interest [13]. From an imaging standpoint, it is exceedingly difficult to monitor endothelialization on the lumen through a thick and optically opaque tubular vessel using conventional microscopy techniques. Furthermore, the preconditioning of such vessels in pulsatile-flow bioreactors poses additional geometrical constraints on the objective's working distance. Therefore, the key significance of this study is the design and validation of an entirely new imaging technique that is capable of performing nondestructive imaging of endothelial cells (ECs) through a thick and optically opaque electrospun scaffold housed within a bioreactor.

Our approach is based on embedding flexible micro-imaging channels (MICs) directly into a vascular scaffold. Each MIC serves as a guiding channel through which we can insert a fiber mirror and locally scan fluorescence pump light across a region of interest (ROI) on the scaffold lumen. After collecting fluorescent signals generated during fiber scanning, we can map the values of these signals onto a digital grid and reconstruct the spatial distributions of the fluorescently labeled ECs. A major advantage of this method is that the link between imaging resolution and imaging depth is "decoupled", making it possible to greatly increase imaging depth without sacrificing imaging resolution. Through a variety of imaging studies using scaffolds and tissue phantoms, we demonstrate that our imaging system can deliver a minimum of 20-30 μm imaging resolution at an imaging depth greater than 10 photon transport mean free paths (TMFPs). Furthermore, we show that the resolution of our imaging system remains essentially unchanged regardless of tissue

thickness. Given the results of this study, our imaging method has the potential to find a wide range of tissue engineering applications.

## Engineering a Vascular Substitute

At the time of this writing, coronary heart disease is the leading cause behind 1 of every 6 deaths in the United States [14]. The development of coronary vascular grafts viable for transplantation has thus gained significant interest in the domain of tissue engineering. To engineer large diameter blood vessels, the prevailing paradigm for developing tissues in the laboratory remains, where first a tube-shaped biomimetic scaffold is fabricated, then seeded with the appropriate cells, and finally subjected to a specialized *in vitro* preconditioning environment provided by a bioreactor. Figure 1.1A shows a pulsatile-flow bioreactor housing a vascular scaffold intended as a replacement for defective carotid arteries. In this example, the neo-tissue is being "trained" for its desired function by pumping culturing media with the applicable growth factors through the vessel to simulate normal blood flow.

Even with such sophisticated methods, to this day, no specimens have been made with the necessary maturity for human transplantation. Although short-term viability has been shown in sheep, the failure of such synthetic grafts has been associated with the lack of functionality of vascular cells and poor integration between host vessel and graft, leading to thrombosis and intimal hyperplasia after transplantation [13]. Achieving an intact endothelial layer on the luminal (inside) surface of vascular grafts is found to be a key component to success due to the ability of endothelial cells (ECs) to provide a continuous thromboresistant barrier between circulating blood and the arterial wall. To investigate the activity of ECs during *in vitro* preconditioning without removing the scaffold from the bioreactor, one has to find a method that can either be applied directly from within the vessel, or enable imaging *through* the vessel wall to the luminal surface. The discussion on the viability of these two options is the subject of the next chapter.

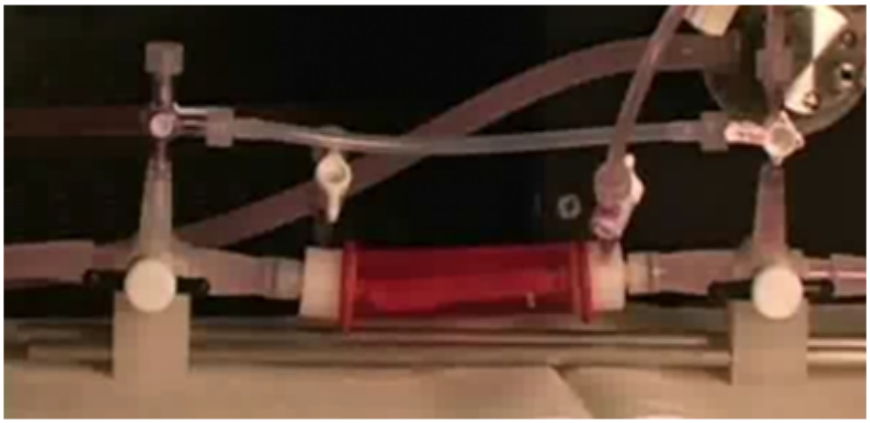

Figure 1.1: The seeded vascular scaffold is seeded with appropriate cells and subjected to an *in vitro* sterile growth environment (bioreactor) for preconditioning. A bioreactor can provide biochemical and physical stimuli to the neo-tissue, such as pulsatile-flow of culturing media, and "train" it to maturity. Once the tissue has achieved the desired maturity, it is transplanted to the target site (e.g. sheep neck).

# Chapter 2

# Related Work

## 2.1 Problem Description

Monitoring the activity of ECs in real time and at cellular level resolutions during *in vitro* precondition presents a particularly difficult problem for the following reasons: First, the method requires to be compatible or integratable with the bioreactor. Although some modifications to the bioreactor can be made, ideally the imaging method should require only minimal bioreactor adjustments so that proper function does not become impaired. Second, the imaging method requires the ability to acquire images semi-continuously over longer periods between a couple of hours to several weeks. To minimize the chances of contamination, the imaging over this extended period should not require opening the bioreactor, nor making many manual adjustments - in short, the method should be fully automated and "hands off". Third, in the interest of automation and the intent of producing high quality time-lapse images, the chosen region of interest (ROI) should remain targeted unambiguously without shifting or motion blurring. Lastly, and arguably the most difficult requirement, is that the imaging method should be adaptable to *in vivo* studies.

### Potential Approaches:

As illustrated in Fig. 2.1A, the nondestructive imaging of ECs on the luminal surface can be approached in two distinct ways. The first is the use of an endoscope which could potentially

provide a direct-line-of-sight view of the cells on the lumen. As is discussed in Section 2.2, microendoscopy poses as an alluring solution to imaging blood vessels, but it comes with several not so apparent drawbacks. The second approach is to image *through* the vessel wall and evaluate the endothelialization using an imaging system located at the vessel's exterior. This requires a deep tissue imaging technology capable of overcoming the information loss induced by the highly scattering scaffold wall. Further obstructive elements may need to be overcome as well, such as opaque bioreactor components or the skin covering the animal at the site of transplantation (e.g. neck) during *in vivo* studies. With these considerations, we embarked on a survey for an applicable imaging methodology. Figure 2.1B briefly outlines current imaging technologies. Upon completion of our survey, we reached the conclusion that an entirely new imaging method is needed that can meet all the aforementioned requirements. Over the course of three years of development, a distinctly unique imaging method was developed - a localized excitation fluorescence imaging (LEFI) method based on fiber optics and micro-imaging channels (MICs) - that enables the real time imaging of endothelialization *in vitro* and eventually *in vivo*.

## 2.2 Microendoscopy

Endoscopes are instruments used to examine the interior of hollow organs or cavities. By directly inserting the device through a patient's body orifice to the region of interest, a close up view of epithelial structures can be provided [15]. Endoscopy is most often associated with gastrointestinal and respiratory examinations, but in recent years, development has progressed towards the miniaturization of the endoscope headpiece. By decreasing the diameter of the headpiece, endoscopy has been applied for small cavity environments, such as bronchial capillaries or the urinary tract and even vasculature in vivo [16, 17, 18]. These devices often make use of fiber optics to decrease the overall footprint of the device and combine microscopy techniques to increase the imaging resolution, giving way to microendoscopy.

Development of microendoscopy has progressed to combine optical coherence tomography [19] and fluorescence imaging modalities such as confocal and multiphoton microscopy. These devices used to be limited to visualizing macroscopic epithelial structures, but have now progressed to visualizing single fluorescence labeled cells in their microenvironment [20, 21, 22]. The diameter of these devices has been reported to be as low as 1.25 mm – small enough to fit into a vascular

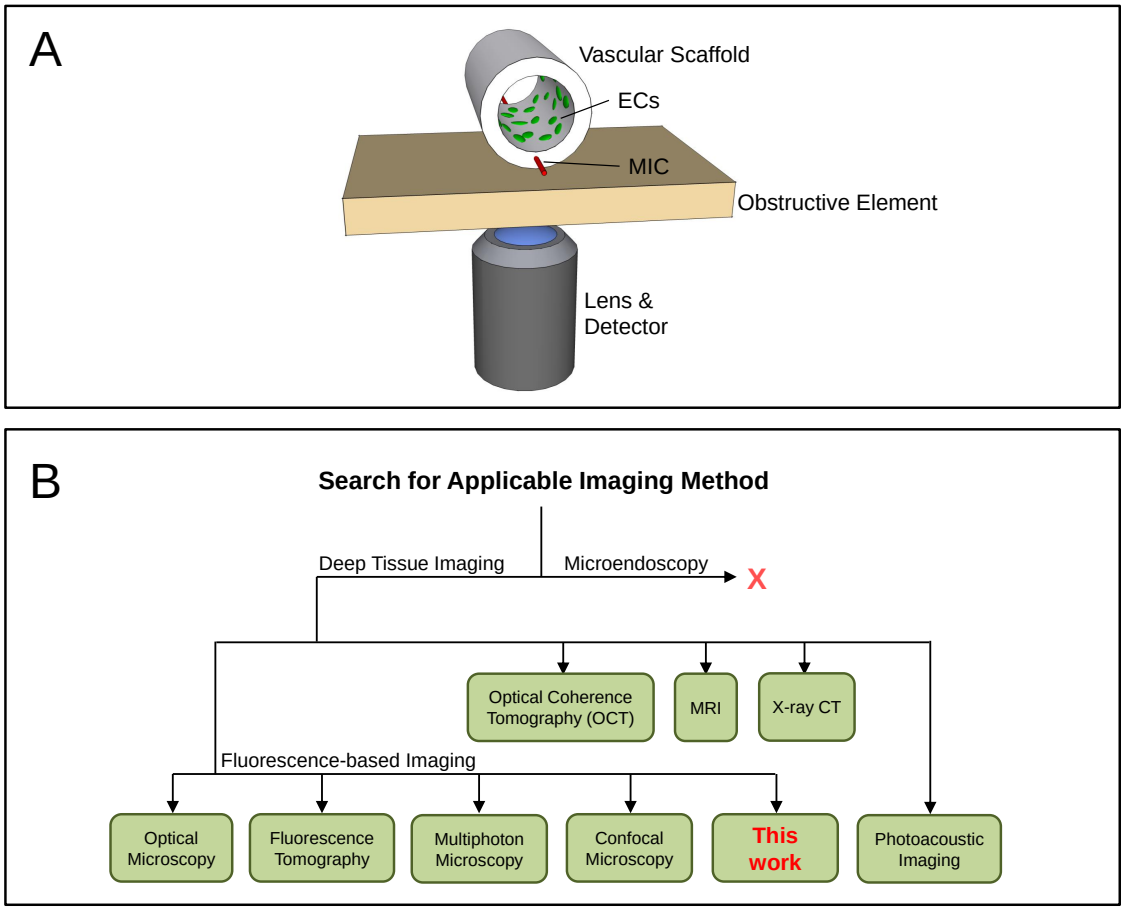


Figure 2.1: (A) The organization and activity of endothelial cells (ECs) on the lumen surface of vascular grafts is of particular interest to vascular tissue engineers. A method is sought that can image the response specific stimuli on endothelialization in real time. A vascular scaffold consists of a thick and opaque wall which poses a significant difficulty for many imaging techniques that are applied from the exterior. Further obstructive elements, such as bioreactor components or the animal's skin post-transplantation may produce additional difficulties. (B) A diagram overview of a selection of imaging methods available for tissue imaging. Upon examining the capabilities of each method, we concluded that an entirely new imaging technique was needed.

scaffold. The optics of many of these systems is based on front view imaging, thus impractical for our use. For tight cavities such as the vascular scaffold, a side-view microendoscope would be needed. Such a device has been recently reported by Kim [23] that offers single-cell resolution.

From an optical imaging standpoint, using a side-view microendoscope such as that by Kim to image the endothelialization of the vascular lumen would seem like an ideal solution. However, from a tissue engineering standpoint, there are several issues that would need to be addressed. First, inserting a physical device into the vascular scaffold prior to imaging can have significant adverse effects for the development of the endothelial layer. Besides potentially introducing contamination to the sterile microenvironment, the cellular proliferation and subsequent organization is highly sensitive to mechanical abrasion, such as that caused by the endoscope headpiece if it were to touch the lumen. Second, assuming this problem were solved, then applying the appropriate growth media flow for in vitro preconditioning becomes an issue. Vascular scaffold development requires the application of physical sheer forces provided the media, as discussed in Ref. [13]. This process would be made significantly more difficult with the presence of an endoscope headpiece, since the diameter of microendoscopy devices cannot be further reduced below ˜1 mm (due to physical optic constraints such as numerical aperture). Third, for the eventual in vivo transplantation of the vessel, the endoscope would cause an issue for suturing the neo-vessel to the native tissue.

Due to the aforementioned issues when using an endoscope for *in vitro* or *in vivo* vascular imaging, we decided to look for alternatives in the realm of optical imaging. Without the ability for direct-line-of sight access to the luminal surface, an method is required that can image *through* the vessel wall to the ECs. This requirement lead to the search of a suitable deep tissue imaging technique as illustrated in Fig. B2.1.

## 2.3 Deep Tissue Imaging

As a consequence of deciding to image *through* the vessel wall to visualize ECs in their microenvironment during vascular scaffold preconditioning, we need to employ a deep tissue imaging technique. The primary issue is overcoming the optically turbid and thick (˜0.5 mm) scaffold composition that makes up the vascular scaffold wall. Several potential deep tissue imaging technologies have been examined which will be briefly discussed, and why they are, or are not, suitable for our purpose. Since the use of fluorescent cell markers has become the state of the art method

for high contrast cellular imaging, we can group deep tissue imaging techniques into fluorescence-based and non-fluorescence based systems.

### 2.3.1 Non-Fluorescence Based Imaging

**Optical Coherence Tomography:**

Optical coherence tomography (OCT) has established itself as a powerful high resolution and non-destructive diagnostic technique for cross-sectional imaging in a variety of medical fields. The principle of operation behind OCT can be loosely regarded as "optical ultrasound", where reflections from within the tissue are used to produce a cross-sectional view. Specifically, the tissue is illuminated externally using low coherence light and the back-reflected light is subsequently detected based on coherence matching between the reflected and incidence beams using interferometry. Since the degree of tissue scattering is the essential component to the detection process for OCT , the method cannot be used for fluorescence imaging. OCT is primarily used for anatomical imaging where contrast is needed for resolving different tissue layers and substructures [24]. Distinctly resolving single cells beyond the immediate tissue surface is difficult using OCT, unless the cells are marked with scattering nanoparticles [25]. Using particles, however, is typically regarded as too invasive for tissue engineering studies, so we required to look for a different imaging technology.

**MRI / X-ray CT / PET:**

The clinical need for large imaging penetration depths has led to the development of magnetic resonance imaging (MRI), X-ray computed tomography (X-ray CT) and nuclear imaging techniques, such as positron emission tomography (PET). These techniques are widely used for deep tissue *in vivo* imaging, but cannot provide the microscopic resolutions needed for imaging single cells. The typical resolution of MRI is between 10 – 100 mm, CT between 50 - 200 mm, and PET between 1 - 2 mm [26].

**Photoacoustic Imaging:**

An exciting development in biomedical imaging is the recent advancement of photoacoustic imaging (PAI). PAI is a hybrid imaging technology based on the photoacoustic effect. Nanosecond-range laser pulses are delivered into the tissue during which some of the energy is absorbed and converted into heat, leading to transient thermoelastic expansions. These rapid expansions result in wide-band ultrasonic pulse emissions which are measured with sensitive transducers that convert the mechanical acoustic waves to electric signals to form two- or three-dimensional subsurface images [27].

The close association of optical absorption with the tissue's physiological properties allows the magnitude of the ultrasonic emission (which is proportional to the local energy deposition) to be used in revealing physiological features at high-resolutions. Because ultrasonic scattering is 2 to 3 orders of magnitudes lower than optical scattering in biological tissues, acoustic imaging can provide better spatial resolution than methods based on electromagnetic irradiation. This circumstance has allowed PAI to image at tissue depths beyond one photon TMFP [26]. Newer developments have shown *in vivo* imaging of microvasculature in skin, where resolutions up to ˜ 10 μm at depths below 1 TMFP have been achieved. However, the resolution degraded to 120 μm within 1.2 mm of skin depth [28].

PAI has shown tremendous potential in simultaneously providing structural and functional information and has been extended to molecular imaging. Through multispectral photoacoustic tomography (MPT), optical reporters such as fluorophores, chromophoric molecules, or nanoparticles, can be used to as contrast agents. Although using biocompatible reporters as contrast agents has lead to imaging macroscopic features, reaching resolutions at the cell level beyond 1 mm imaging depth is yet to be shown [29][30].

Imaging based on photoacoustic interactions in tissues has become the fastest-growing area of biomedical imaging technology with a promising future to extend high resolution sensing at high contrast *in vivo* beyond the TMFP range. For our purposes, however, PAI and MPT are both not well suited. For one, the resolution provided at the single cell level is not sufficient at the depths required to image ECs on the luminal surface. In Section 5.4, we show that an imaging penetration depth of at least 3 TMFP is needed, which both PAI and MPT cannot provide as of now. Even if the required level of sophistication is reached, there still remains the relatively high equipment

cost of the opto-acoustic instrumentation since these systems are not commercially available, thus rendering these systems not economically viable for our purpose [31].

### 2.3.2 Fluorescence-Based Imaging

Fluorescent labeling, when combined with an appropriate imaging instrument, is a powerful and sensitive method that is widely used in molecular biology and biochemistry. In fluorescence-based imaging systems, the sample is first illuminated with light at a wavelength that induces fluorescence in the target (i.e. cell or macroscopic structure). The emitted light, which is usually at a longer wavelength than the incident light, is then measured using a detector. Filters are normally employed to ensure that only the emitted light reaches the detector, and that the excitation light is blocked. The excitation light is often termed "pump light", because it effectively supplies the fluorescent reporter with electromagnetic energy, upon which emission light at a lower energy level is released. This mechanism allows for very high contrast images of both macroscopic and molecular-level targets, since only light from the fluorophore is detected, and all elements without fluorescence are canceled out.

**Optical Microscopy:**

Although not technically a deep tissue imaging technique, fluorescence microscopy is the most ubiquitous implementation of fluorescence-based imaging. After simple integration into a standard optical microscope using the appropriate filters and pump light, fluorescence microscopy is widely used to study organic or inorganic substances using a variety of fluorescent reporters that include dyes, organic or inorganic particles such as quantum dots, or biological tagging based on fluorescent genes [32]. With fluorescence microscopy, the typical imaging depth that can be achieved is one photon mean free path (MFP), which is not sufficient for blood vessel imaging [33]. It does, however, present itself as a valuable direct-line-of-sight technology which we employ for result verification and quantification (e.g. Section 6.4.2).

**Fluorescence Tomography:**

Fluorescence tomography is a form of computed tomography that reconstructs images based on diffuse fluorescence signals that transmit and scatter through the tissue to the surface. The back-calculated origin of a fluorescent signal is then plotted in a digital volumetric model to form a three-dimensional image. Often in fluorescence tomography, forward mathematical models are used to describe the distribution of photons inside the tissue. The inverse problem then seeks to reconstruct the fluorophore parameters from the boundary measurements to find its concentration or life-time. Finding solutions to the inverse problem is often ill-posed requiring the incorporation of initial conditions into the algorithms which may not be known prior to reconstruction [34].

Optical projection tomography has shown promising advancements. This evolution of fluorescence tomography is based on tissue trans-illumination over multiple projections using unfocused light sources analogous to X-ray CT. The collected images are fed into algorithms that back-calculate the location and concentration of fluorescent sources using inverse mathematical models. The recording of multiple images from various angles assists in providing additional information to the algorithms resulting in an increase in accuracy[35].

The use of fluorescence tomography is an interesting prospect due to its noninvasive nature. Since only broad illumination for fluorescence excitation is needed - or no source at all if based on bioluminescence [36] - the method would be well suited for *in vitro* and *in vivo* vascular imaging. Although great imaging penetration depths can be achieved beyond 5 TMFP, the reconstruction resolution is often greater than 100 - 200 μm and not at the cellular level [26].

**Confocal & Nonlinear Microscopy:**

The most widely used technologies for *in vitro* and *in vivo* imaging of tissues are confocal and non-linear microscopy. These imaging techniques can achieve ultrahigh resolution up to the diffraction limit near the tissue surface and achieve cell level resolutions up to nearly 1 TMFP.

Scanning laser confocal microscopy (CLSM) scans a focused laser beam into the tissue specimen and uses a pinhole to reject light that arrives out-of-focus with respect to the detector. By scanning the focused beam over the ROI inside the tissue and entering signal values that are in focus into a digital grid, a two-dimensional tissue section can be rendered into an image. By repeating this

procedure at different depths, a three-dimensional image can be acquired. CLSM imaging depth is typically restricted to 5 MFPs for cell level resolutions [26].

Nonlinear microscopy methods such as two-photon microscopy (TPM) employ a similar laser scanning method, but instead make use of femtosecond laser pulses for target illumination. These short pulses are needed to achieve the necessary level of energy absorption within the spatially confined area of the focus point. Since a certain threshold is needed to undergo the two-photon absorption process, all fluorescence photons are generated from a highly localized volume. By knowing the relative location of the focused beam, the fluorescence response signals can be mapped into a digital grid much like CLSM. Using TPM, state of the art systems can achieve up to 8 MFPs at cell level resolutions [26].

The a promising deep tissue resolution, methods based on confocal or nonlinear microscopy have been employed to nondestructively monitor cells in their microenvironment [37, 38, 39, 26, 40]. Of particular relevance are two recently reported methods that can monitor tissue development during preconditioning in bioreactors [12, 41]. Specifically, Kluge et al. imaged GFP-tagged fibroblasts in a bioreactor system capable of applying mechanical stretch to the silk fibroin sponge scaffolds over several consecutive days using confocal and nonlinear microscopy. In a similar manner, Niklason et al. used a nonlinear optical microscope to assess smooth muscle cell-seeded poly (glycolic acid) vessel scaffolds housed within a specialized pulsatile-flow bioreactor. However, since these methods are based on standard confocal/multiphoton microscopy, they are less than ideal for imaging optically opaque biomaterials. In particular, since engineered tissue scaffolds typically require very high porosities (i.e. electrospun scaffolds [13, 42, 43]) for cell migration and proliferation, such scaffolds tend to induce very strong optical scattering and are consequently highly opaque. As a result, it is very difficult to achieve a large imaging depth in such scaffolds using either confocal or multiphoton microscopy. With a limited imaging depth, the methods reported in Ref. [12, 41] may not be suitable for the evaluation of a clinically relevant vascular graft, where the graft must possess sufficient thickness to maintain structural integrity in the presence of pulsatile blood flow. An additionally drawback of the methods presented in Ref. [12, 41] is the extremely short working distances of the objective lenses. Since any tissue construct under evaluation must be placed within the working distance of the objective lens, the bioreactors reported in Ref. [12, 41] must be specially designed to meet this requirement. For many bioreactors, it would be very difficult to overcome such a stringent constraint on scaffold placement.

**Our fiber optic method**

From the aforementioned discussion on a variety imaging techniques, we find that none are entirely suited for imaging ECs in real time at cellular level resolutions. To overcome this challenge, we have developed an imaging method based on fiber optics. We investigated the potential of using fiber-guided pump light to locally excite fluorescent cells and to capture the emission light externally to produce mapped images in highly scattering scaffolds. This requires the embedding of flexible micro-imaging channels (MICs) as depicted in Fig. 2.1 directly into a vascular scaffold. Each MIC serves as a guiding channel through which we can insert a fiber micro-mirror and locally scan excitation light across a region of interest (ROI) on the scaffold lumen. After collecting fluorescent signals generated during fiber scanning, we can map the values of these signals onto a digital grid and reconstruct the spatial distributions of the fluorescently labeled ECs. A major advantage of our method is that the link between imaging resolution and imaging depth is "decoupled", making it possible to greatly increase imaging depth without significantly sacrificing imaging resolution.

## 2.4 Conclusion

Imaging the cell activity along the luminal surface of vascular scaffolds inside a bioreactor presents itself as a unique challenge. Accomplishing this in real time at cellular resolutions while the tissue is being preconditioned turn this into an even more daunting task. An obvious first candidate is using microendoscopy, but due to size limitations and contamination issues, this route was not pursued. As a consequence of avoiding vessel imaging internally (i.e. direct-line-of-sight to the lumen), we required to image *through* the vessel wall which lead to the examination of state of the art deep tissue imaging techniques. Finding a deep tissue imaging method that is compatible or integratable with a bioreactor presents its own set of problems. Due to the long working distances required from the tissue being subjected inside a bioreactor, the use of nonlinear or confocal microscopy techniques is impractical. Other techniques such as OCT are formidable at imaging deep within a tissue at high resolutions, but suffer from a limited contrast between individual cells. Other methods such as MRI/X-ray CT, PET, or fluorescence tomography do not have the required resolutions for imaging individual ECs in their microenvironment. Finally, the most promising candidate is PAI, which with further development using spectrally resolved systems in conjunction

with cell reporters to for celular contrast, could see applicability for vascular scaffolds. Until the desired sophistication, contrast, and resolution is reached with PAI systems, we required to develop a novel imaging method.

The method presented in the following chapters shows how we designed a system that possesses the ability to acquire images semi-continuously over extended periods. Our method does not require opening of the bioreactor, nor making many manual adjustments, and is fully automated and "hands off", just as we sought out to do.

# Chapter 3

# Methods & System Design

## 3.1 Scaffold Fabrication

### 3.1.1 Introduction to Electrospinning

An increasingly popular approach to tissue design is to fabricate and culture the tissue or organ from the "bottom-up" [44]. This is often accomplished by implanting or "seeding" cells into an artificial tissue template capable of supporting three-dimensional tissue formation. These structures, typically called scaffolds, are designed to provide similar mechanical and biological support as the native tissue's extracellular matrix. A high porosity and adequate pore size is necessary to facilitate cell seeding and diffusion throughout the whole structure for both cells and growth nutrients. Further, biodegradability is often an essential factor since scaffolds should preferably be absorbed by the surrounding tissues without the necessity of surgical removal [45, 46].

A number of different methods have been described in the literature for fabricating porous scaffolds. The process of electrospinning, as introduced to tissue engineering by Li [47], is employed exclusively for the scope of this work due to its practical applications to vascular tissue design. Specifically, electrospun scaffolds can provide the necessary mechanical strength and flexibility to withstand the normal blood pressure of native vessels (e.g. carotid arteries) while being simple, reproducible, and inexpensive to make in the laboratory.

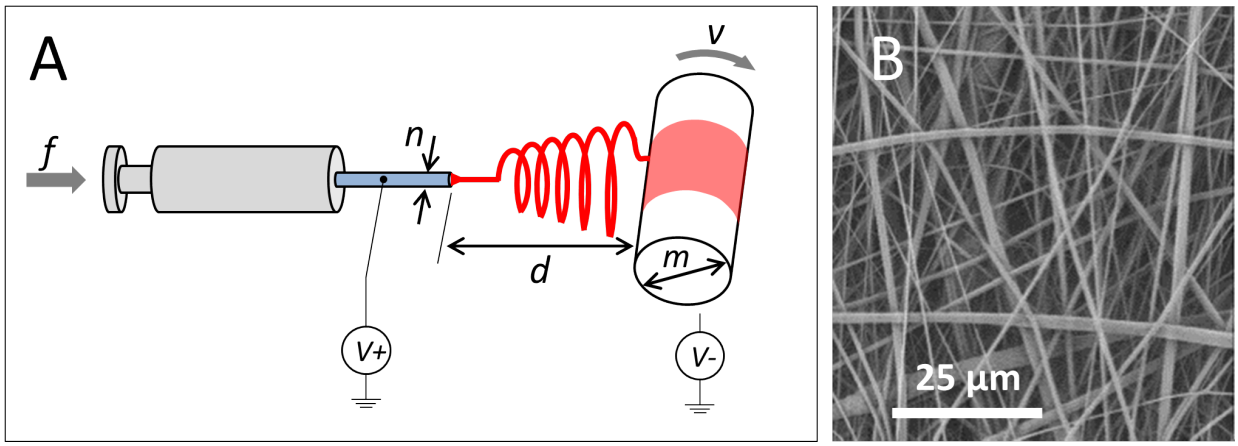


Figure 3.1: (A) Electrospinning setup using a spinning mandrel or rod as a collector. The needle tip is positively charged and the collector is negatively charged with high voltage sources causing the polymer to be drawn to the collector. The jet is a single solidified string of polymer and is wound around the spinning collector. (B) An SEM image of a biodegradable PDLLA scaffold mesh showing the highly porous structure.

An electrospinning setup typically consists of a syringe pump, a high voltage source, and a collector such as a metal plate or a spinning metal rod or mandrel (Fig. 3.1). Prior to electrospinning, the natural or synthetic polymer is liquefied with a solvent at the desired concentration and then poured into the syringe. During the electrospinning process, the polymer extruded from the syringe's needle tip is positively charged by the high-voltage source causing the initiation of a jet that is "sprayed" towards the negatively charged collector area. Upon traveling from the needle tip to the collector, the solvent evaporates and the polymer solidifies. Although it appears as a spray, the polymer jet is in fact a single, continuous, and rapidly whipping polymer fiber.

The diameter of the polymer fiber can be adjusted by manipulating a number of electrospinning parameters. These include solution properties such as viscosity, conductivity, and polymer molecular weight. Controlled variables include syringe flow rate, electric field strength, distance between tip and collector and collector composition and geometry. Ambient temperatures can also influence the outcome, so temperature and humidity should be kept constant. By adjusting the appropriate electrospinning parameters, a densely packed or highly porous scaffold mat can be fabricated with fiber diameters ranging from 50 nm to 5 µm. An SEM image of scaffold is shown in Figure.

### 3.1.2 Choice of Scaffold Polymer

For prototyping, we used bioabsorbable poly-(DL)-lactic acid (PDLLA). Ideally, we would want to use a blend of poly(3-caprolactone) (PCL) and collagen type I to form PCL/Collagen vascular scaffolds as is done in Refs. [48, 49]. There are, however, two benefits to using PDLLA for prototyping over PCL/Collagen: First, the parameter tolerances such as collector distance, applied charge, and ambient temperature are quite forgiving for PDLLA, allowing the fabrication of reproducible samples with relative ease. Having the ability do re-fabricate nearly identical scaffold samples has proven to be a valuable asset to the prototyping phase. The second benefit for using PDLLA for prototyping is its sintering ability, allowing us to meld scaffold sheets together using the appropriate ambient temperature to form planar scaffolds for testing. The PDLLA scaffold sintering method is discussed in Section 3.1.4.1.

### 3.1.3 Electrospinning Parameters

PDLLA (Mw = 80,000 g/mol, SurModics Pharmaceuticals, Birmingham, AL) was suspended in a 22% w/v solution with a 3:1 ratio of tetrahydrofuran:dimethylformamide (Fisher Scientific, Fair Lawn, NJ) under gentle stirring for four hours. Next, the polymer solution was poured into a syringe and delivered at a flow rate of f = 5 ml/hr through an 18G blunt-tip needle (n = 0.838 inner diameter). A charge of V+ = 13 kV was then applied to the needle tip and a charge of V- = -2 kV to the collector using two DC power supplies (Gamma High Voltage Research, Ormond Beach, FL). The collector was placed d = 15 cm away from the needle tip. Once the scaffold sheet reached its desired thickness, it was removed from the collector and placed in a desiccator for 10 hours to remove any residual solvent. Refer to the labels in Fig. 3.1 for clarity on the parameter values.

### 3.1.4 Scaffold Designs

The electrospinning setup in Fig. 3.1 was used to fabricate scaffolds in two different configurations. The first is a planar design intended to simulate the wall thickness of a vascular scaffold. The second type is a tubular shaped vascular scaffold design based on Ref. [50]. For experiments requiring the embedding of one or multiple MICs, a separate fabrication method was used for either the planar scaffold or vascular scaffold design.

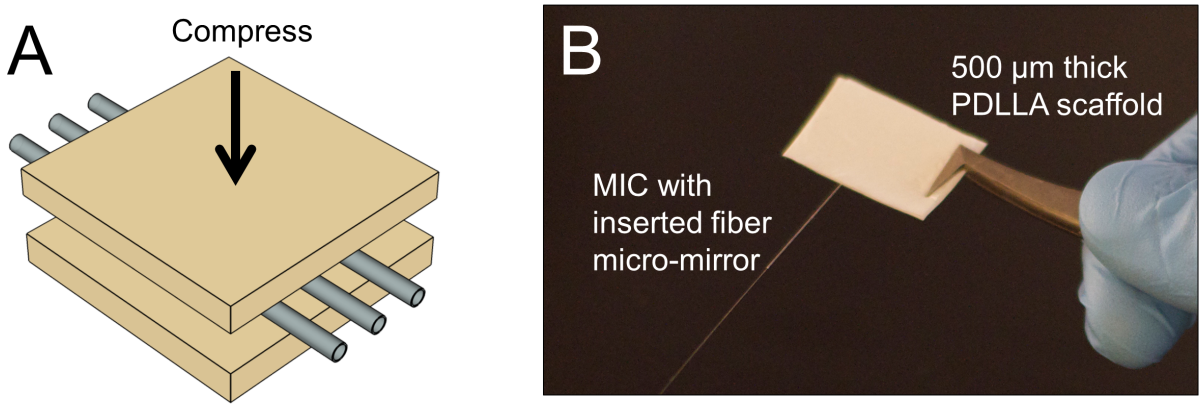


Figure 3.2: (A) A thinly woven PDLLA scaffold mat was electrospun and then cut into 3 cm × 2cm rectangular mats. The planar scaffold was fabricated by placing MICs between two scaffold mats and heat sintering them together. (B) A photograph of a sintered planar scaffold with an embedded MIC. The fiber mirror is inserted into the MIC.

#### 3.1.4.1 Planer Scaffold

To create planar scaffold mats, the polymers were electrospun onto a spinning aluminum mandrel with a diameter m = 5 cm rotating at v = 60 rpm. Once the desired thickness was reached, the scaffold was cut along the axis of the mandrel and carefully removed resulting in a 20 x 15 cm mat. This mat was then cut into appropriate sized sections. To embed the MICs into a PDLLA scaffold, we used the heat sintering method as reported in Ref. [42]. The MICs were placed between two scaffold mats as illustrated in Fig. 3.2(A) and then compressed between glass slides and a 32 g weight in an oven at 54°C for 15 minutes. This technique effectively fused the scaffold mats together to produce a one-piece planar scaffold with MICs securely embedded. Figure 3.2(B) shows a PDLLA scaffold with a single embedded MIC and a fiber mirror inserted.

#### 3.1.4.2 Vascular Scaffold

Scaffolds with a tubular structure were fabricated by electrospinning the polymer onto a spinning 303 stainless steel rod (m = 4.75 mm). The rod effectively defined the inside diameter of the finished vessel. Due to the shrinkage of the mesh during electrospinning, the scaffold may tighten onto the rod and become difficult to remove without physically damaging it. To solve this problem, a thin layer of polyethelyn oxide (PEO) that acts as a release layer was electrospun onto the rod

prior to making the vessel. The water solubility of PEO allows for easy removal of the vessel after submerging the rod in sterile water for 1 hour. To fabricate a tubular scaffold vessel with one or more embedded MICs, we use a five step process as illustrated in Fig. 3.3. First, a ˜ 10 µm thin layer of PEO is electrospun on to the rod. Next, a layer of PDLLA is electrospun on top of the PEO layer. This formed the lumen layer of the scaffold. The MICs were then placed on top of the scaffold. The electrostatic charge of the scaffold was enough to hold the MICs in place without the need of tape or glue. The second polymer layer was then electrospun with the desired thickness. The combined thickness of the inside and outside electrospun layers thus form the total thickness of the vascular scaffold's wall. Finally, the rod holding the scaffold was submerged in sterile water in order to dissolve the PEO and remove the vessel from the rod. Once finalized, the tubular geometry ensures that the MICs are embedded tightly as shown in the photograph in Fig. 3.3(B).

## 3.2 Bioreactor Design

### 3.2.1 Overview

A key component for tissue engineering is the use of bioreactors for controlled tissue cultivation. This has been defined as "a system that simulates physiological environments for the creation, physical conditioning, and testing of cells, tissues, precursors, support structures, and organs in vitro" (Barron et al., 2003) [51]. These are systems in which biological and/or biochemical processes can be closely controlled in order to induce a certain behavior in living cells or tissues. Particularly for tissue and organ preconditioning, bioreactors are often designed to provide an *in vitro* environment that closely mimics one or multiple *in vivo* conditions found in the native tissue environment. Despite the inherent complexity in recreating the optimal growth environment and conditions, several studies have been reported in recent years demonstrating the successful use of bioreactors in growing functional tissues with sufficient maturity for human transplantation [2, 4, 52, 53].

The requirements that a bioreactor must fulfill vary depending on the goals of the study as well as the dimensions, complexity, and physiological environment of the tissue to be engineered. The overall goal is to have a system that reliably and reproducibly delivers environmental conditions

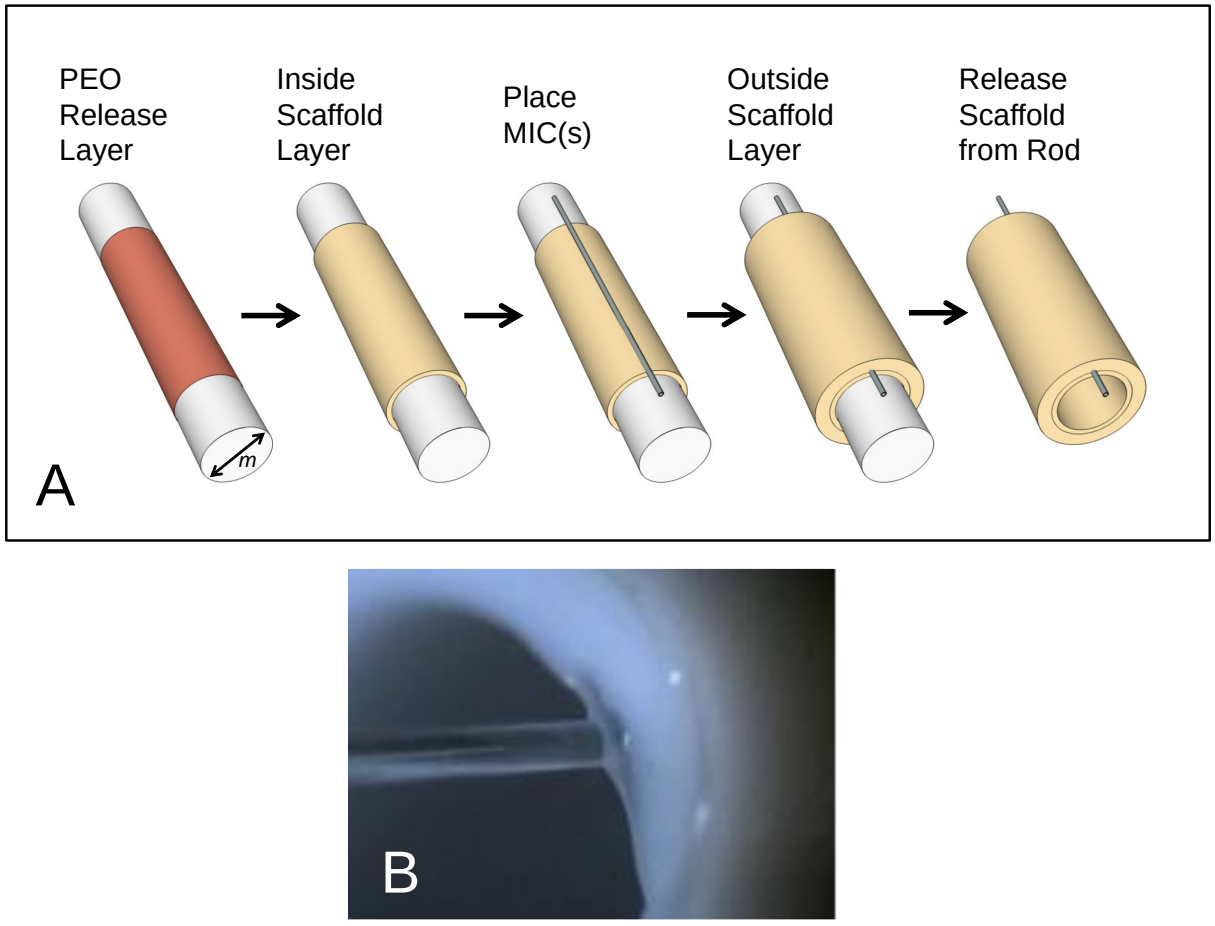


Figure 3.3: (A) Embedding of MICs is done in a multistep process. First, a PEO release layer is electrospun on to the rod. This will aid in removing the vascular scaffold after fabrication. Next, the inside layer is electrospun over the PEO layer. The MICs are then placed onto the inside layer. The electrostatic attraction of the PDLLA is enough to hold the MICs in place. Next, the outside layer is electrospun on top of the MICs. After securely embedding the MICs and after the desired vessel thickness is reached, the rod is removed from the rotational motor and placed into a sterile water bath. Once the PEO is dissolved in the water, the vascular scaffold can easily be removed from the rod. (B) A finished vascular scaffold with an embedded MIC. After drying, the scaffold is put into a desiccator overnight to remove any residual solvent.

such as gas (i.e., oxygen, nitrogen, carbon dioxide), media flow rates, temperature, pH, nutrients in the culture medium (e.g. glucose, amino acids), as well as continuous removal of waste products produced by cellular metabolism. Further, the bioreactor is required to be operating over long periods of time without bacterial contamination since maturation of a functional tissue may take several weeks to months.

Exposing the developing tissue to appropriate physical stimuli within the bioreactor has also shown to have a profound effect on cellular behavior. By exposing the cellularized tissue to physiological and/or hydrodynamic stimulation such as stress/strain or shear forces, the behavior, spatial distribution, secretion of bioactive compounds, and phenotype of the cells can be modulated [13][48]. This can be used to form ideal cell distributions throughout the tissue and to "train" the construct to perform for its intended function.

The primary use of bioreactors in this work is for the study of vascular graft preconditioning. In particular, studying the formation of the endothelial lining on the luminal (inside) surface of blood vessels presents an important step towards the successful design of arterial grafts. Therefore, we require a bioreactor design that can recreate the hemodynamic forces acting on the endothelium, such as tensile stress acting along the vessel wall and shear stress acting along the length of the vessel. We can recreate this action by applying pulsatile flow using the appropriate culturing media along the inside of the cell-seeded vessel to simulate natural cardiac blood flow [13].

In order to study and improve the effect of the applied biochemical and physical stimuli to the formation of the endothelium, we require a bioreactor that not only satisfies the above mentioned requirements, but also enables the integration of our novel imaging method. We designed two bioreactor systems for the work presented here. The first is a parallel plate bioreactor used primarily for the imaging prototyping experiments. The second is a pulsatile flow bioreactor that integrates non-invasive imaging of endothelium formation.

### 3.2.2 Parallel Plate Bioreactor

A bioreactor was designed to house planar scaffolds in a growth chamber while simultaneously accommodating the embedded MICs for prototyping. The concept of the bioreactor is based on a parallel plate flow chamber as reported previously by Kreke & Goldstein [54]. This established a base expectation that our experiments on live cell imaging are done in a system that has successfully

shown cell proliferation on scaffolds. The key design change to the bioreactor is the integration of the MICs. The major difference was the use of biocompatible silicone adhesive (Dow Corning, Midland, MI) to seal the portion of MIC that extended beyond the scaffold between a series of polydimethylsiloxane (PDMS) (Specialty Manufacturing Inc., Saginaw, MI) gaskets and glass slides. The cavity created by the PDMS gaskets formed a sterile growth chamber while the glass slides provided viewing access for cameras to record optical signals on both sides of the scaffold. A photograph of the bioreactor with a planar scaffold sample inside is shown in Fig. 3.4(A).

#### 3.2.2.1 Assembly

We construct the parallel plate bioreactor according to the steps illustrated in Fig. 3.4(B). There are three primary components making up the bioreactor – an aluminum bracket, a 75 x 25mm microscope slide (Corning, NY), and a gasket cut from a larger sheet of PDMS that circumscribes the glass slide. Prior to the construction, every bioreactor component is sterilized in 70% ethanol in order to eliminate biological contamination. All assembly must be done in a sterile environment and ideally in a laminar flow hood. First (1), a glass slide is placed on an aluminum bracket, and then a gasket is placed on top of the glass slide. The gasket and the slide thus form the lower half of the growth chamber. The scaffold sample is then placed into the chamber with the protruding MICs facing outwards as shown in the diagram. Next (2), a line of silicone adhesive is pasted along the gasket surface (yellow line in diagram). A second gasket is then added on top of the first gasket and carefully padded down making sure there are no air bubbles. The MICs should now be sealed air-tight between the two gaskets once the silicone adhesive has dried (6-8 hours). The lower half of the bioreactor holding the planar scaffold sample is then ready for sterilization with ethanol. After sterilization, the scaffold is seeded with cells using the appropriate cell culture and seeding protocol. In the next step (3), a glass slide is placed on top of the gaskets and then the whole construct is pressed together with a second aluminum bracket. The brackets are held together by four screws that are carefully tightened without breaking the glass. Once assembled, the scaffold is subject to an air-tight tissue growth chamber. To inject the growth media into the chamber, two 22G needles are inserted between the gaskets which form media inlets as shown in Fig. 3.4(A). The silicone glue between the gaskets is pliable enough so that the needle circumference does not create any hermetical inconsistency. By injecting the media through one inlet while tilting the bioreactor sideways such that the second inlet faces up, the growth chamber can be slowly filled with media

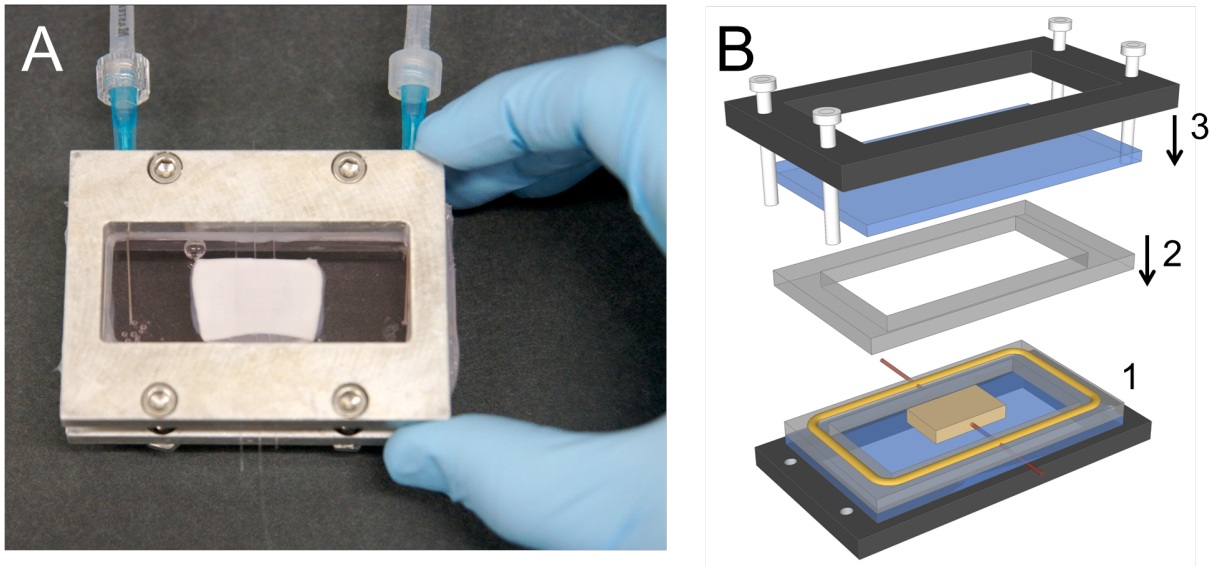


Figure 3.4: (A) Photograph of a planar scaffold with several MICs housed inside the parallel-plate bioreactor (B) Construction of the parallel plate bioreactor is carried out in following steps: (1) The lower half of the bioreactor chamber is assembled and the scaffold sample is place inside making sure the MICs face outwards. (2) The MIC(s) are sealed air-tight between two gaskets with biocompatible silicone glue (yellow line). (3) The scaffold is then sterilized and seeded with cells. After seeding, the rest of the bioreactor assembly is finalized by subjecting the glass slides and growth chamber between two aluminum brackets that are held together with screws.

without any air bubbles inside. The inlets are then closed off with standard fluidic valves. Note: Ensuring that there are no significant air pockets inside the bioreactor chamber is important since air bubbles may interfere with the image quality or collection efficiency of the cameras. Once the inlets are closed off, the media remains in a static environment for testing. Our experience has shown that the parallel plate bioreactor can sustain a state of cell proliferation of at least 12 hours (hTIME cells) without exchanging the media and the bioreactor is consistently heated to 37 °C.

### 3.2.3 Pulsatile Bioreactor

A pulsatile-flow bioreactor was designed for preconditioning vascular scaffolds that simultaneously accommodates the the scaffold-embedded MICs for imaging. The design is based on the bioreacotor in Ref. [13]. By making minor adjustments to the design, we were able to develop a bioreactor who's function was not impaired by the MICs and was easy to assemble and handle. Since seeding is often a time sensitive procedure, assembly time of the bioreactor has to be taken

into consideration. The photograph in Fig. 3.5(A) shows the pulsatile-flow bioreactor with a vascular scaffold housed inside. The chamber holding the vessel is hermetically sealed so that it remains sterile for extended periods. Testing has shown that the design can keep a sterile growth chamber environment when subjected to normal outside conditions over two days. Ideally, for longer term experiments, the bioreactor would be placed in a sterile chamber, such as an incubator.

The major design element of the bioreactor is that the vessel is held securely in place between two conical ports. These ports are slightly smaller in diameter than the vessel inside diameter so that the vessels can be fitted over with slight pressure. The conical design ensures that the vessel is tightly arrested onto the ports so that there is no need for sutures. In order to integrate the scaffold-MIC composite with the bioreactor, a critical design feature has been implemented. The ports that hold the vessels have a distinct notch along the boring as illustrated in Fig. 3.5(B). These notches allow the MICs to thread through the ports during bioreactor is assembly. After bioreactor assembly, the open sections by the notches are sealed using biocompatible silicone adhesive as indicated in the yellow in Fig. 3.5(B).

Growth media can be pumped continuously or in pulsatile-flow through the interior of the vessel by attaching media supply tubes to the center inlets (Fig. 3.5(C)). This allows the vessel to be "trained" by supplying physical stimuli in the form of sheer forces and lateral pressure along the lumen as well as biochemical stimuli through the media. The outer media inlets are used to supply culture media to the outside of the vessel and to fill up the main bioreactor chamber. In fact, the media in the vessel's interior and that of the main chamber is virtually separated by the vessel wall itself. This allows for using two different types of media to tailor to the cells seeded on the inside of the vessel, such as ECs, and to the outside of the vessel (e.g. smooth muscle cells). The bioreactor was tested under extreme flow rate conditions to see if it can sustain normal operation. A flow rate of 300+ ml/min was applied without any leakage, which is enough for most vascular scaffold preconditioning experiments.

#### 3.2.3.1 Assembly

The assembly of the pulsatile-flow bioreactor is performed in the following steps: First, the vascular scaffold is inserted into a bioreactor port making sure the MICs thread through the notches as illustrated in Fig. 3.5(D). Next, the silicone cover is added and arrested onto the port by a sealing ring (Fig. 3.5(E)). The second port is threaded through the MICs on the opposite end and onto

the vessel. The bioreactor is then closed with the sealing ring and lastly, the gaskets for tube attachment are put into the holes of the ports as illustrated in Fig. 3.5(F). Once the main bioreactor chamber is assembled, it is ready to be snapped onto the holder. The silicone adhesive is then applied to seal the notches (Fig.3.5(G)).

## 3.3 Excitation light delivery

Delivery of pump light for fluorescence excitation (pump light) was achieved by inserting an angle-polished fiber mirror into the transparent MIC as shown in the image in Fig. 3.6(A). The mirror was fabricated by polishing the tip of a standard single mode fiber (SMF430, Nufern Inc., East Granby, CT) at a 45° angle with a 0.1 μm grit diamond lapping film (Pace Technologies, Tucson, AR). Excitation light was coupled into the optical fiber and perpendicularly redirected by the 45° air-silica interface via total internal reflection as shown in Fig. 3.6(B). After inserting the micro-mirror into the MIC, the propagation direction of the excitation light was controlled through the translational and angular position of the inserted fiber mirror. In order to enhance the reflection of the pump light off the mirror surface, an additional metal coating can be sputtered on. This has shown to eliminate unwanted evanescent light that travels along the silica-air interface and launches at a 45° angle instead of the desired 90° angle.

## 3.4 Scanning and Mapping Algorithm

The key feature of the scanning fiber mapping method is the localized fluorophore excitation. More specifically, after using the fiber mirror to deliver pump light into the scaffold, we can assume all fluorescent signals are generated within this highly localized light spot on the luminal surface. This local light spot is referred to as an “pump spot” and its location on the lumen is controlled by the fiber mirror position within the MIC. The illustration in Fig. 3.7(A) shows the excitation spot as it appears on the lumen.

The scanning system possesses two degrees of freedom: one is the forward/backward translation x and the other is angular rotation $\vartheta$ of the fiber inside the MIC defined in Fig. 3.7(B). As the

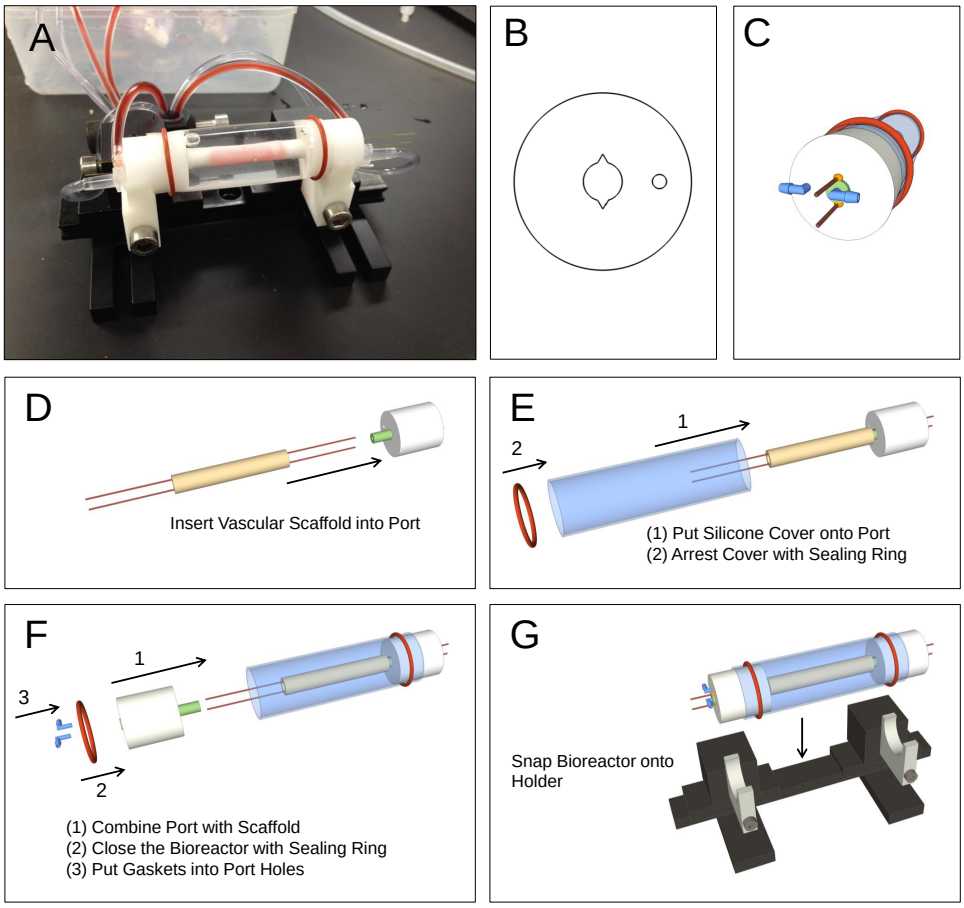


Figure 3.5: (A) Pulsatile-flow bioreactor enabling the preconditioning of vascular scaffold grafts. This bioreactor is adapted from a previous design with minimal adjustments to allow the inclusion of MICs during assembly. The photograph shows the MICs standing out from the side of the bioreactor. Through these MICs, we can insert the fiber mirrors and locally deliver fluorescence pump light. (B) The side profile of a bioreactor port. These main ports hold the vessel in place on each end while allowing the MICs to pass through. This is accomplished by tiny notches in the inner boring. (C) Once assembled, the notches are sealed using biocompatible silicone adhesive (yellow). BIOREACTOR ASSEMBLY: The bioreactor is assembled in four steps. First, the vascular scaffold is inserted into a bioreactor port making sure the MICs thread through the notches (D). Next, the silicone cover is added and arrested onto the port by a sealing ring (E). The second port is threaded through the MICs on the opposite end and onto the vessel. The bioreactor is closed with the sealing ring. Lastly, the gaskets for tube attachment are put into the holes of the ports (F). Once the main bioreactor chamber is assembled, it is ready to be snapped onto the holder. The silicone adhesive is now applied to seal the notches (G).

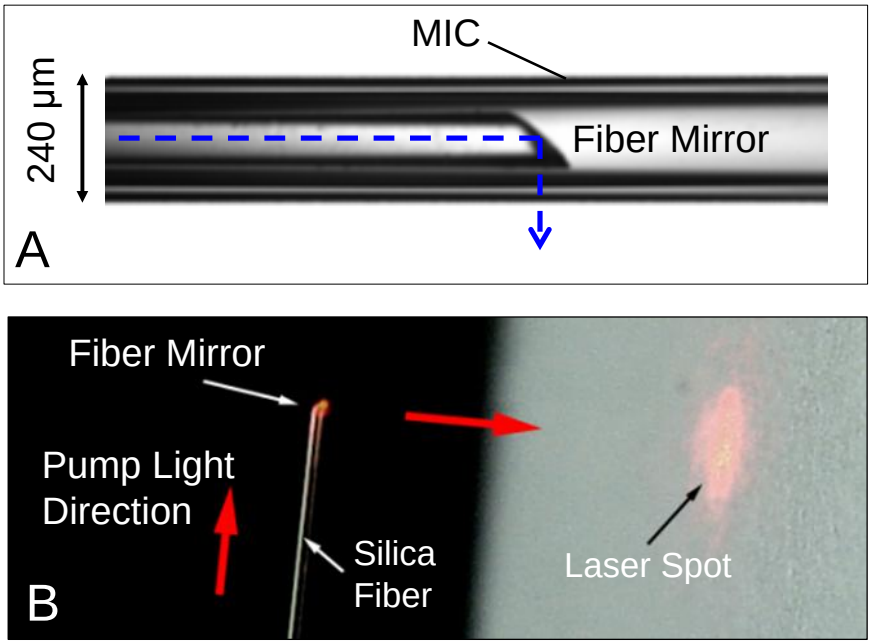


Figure 3.6: (A) Delivery of fluorescence pump light into the scaffold is achieved by using an angle polished fiber mirror. (B) Demonstration of how the 45° angle polish causes the incident pump light to reflect away from the fiber at a 90° angle. This is effectively used to deliver pump light perpendicularly to the fiber axis and to scan the ROI according to the mapping algorithm.

excitation spot is scanned across the lumen, a fluorescence response is generated if the spot overlaps with a fluorophore. A portion of the fluorescent signal travels through the optically opaque phantom and is captured by the detector. Since all fluorescent signals are produced within the spatially-localized excitation spot, we can "reconstruct" the fluorophore distribution by using the intensity of the fluorescence signal captured by the detector. This reconstruction process is referred to as "fluorescence mapping", and is described in detail below.

First, we selected a ROI on the lumen and divided it into a grid of imaging pixels (IP) as illustrated in Fig. 3.7(C). Every IP in the grid can be selectively illuminated by the excitation spot by establishing a one-to-one correspondence between the center of the spot (e.g., R axis and T axis) and the corresponding fiber mirror position (x, $\vartheta$). In Fig. 3.7(C), we define the R axis as parallel to the MIC and the T axis as perpendicular to the MIC. Note that the coordinate R is a function of the fiber rotation angle $\vartheta$ and T is directly given by the linear translation x of the fiber mirror. Furthermore, $\vartheta = 0$ denotes the case where the excitation light is launched directly towards the lumen.

To begin an experiment, the excitation spot is first positioned to IP = 1. The resulting fluorescence signal response value is then collected by the detector and assigned to IP = 1. This process is repeated for each IP in the pixel grid by discretely scanning the excitation spot across the luminal surface. By plotting the response intensities of each IP in the pixel grid as a 2D intensity array, we obtain a mapped image of the fluorophore distribution on the luminal surface.

To intuitively understand the validity of this imaging method, let us consider an ideal case that satisfies the following assumptions: 1) the excitation spot is contained entirely within any given IP, 2) the excitation light intensity remains constant across the lumen surface for all fiber mirror locations, and 3) the scaffold does not generate any background fluorescence (i.e., autofluorescence) as "noise". In this ideal case, the fluorescent response assigned to each IP should be directly proportional to the brightness of the fluorophores within the corresponding IP. As a result, the image obtained through fluorescence mapping should accurately reflect the spatial distributions of fluorophores over the lumen.

This intuitive analysis also identifies three factors that may limit the performance of the fluorescence mapping method including: 1) the excitation spot may exceed the size of an IP; 2) the excitation light intensity may not remain constant over the luminal surface; and 3) the scaffold may generate autofluorescence that overwhelms the fluorescent signals produced by the fluorophores.

As shown in the following chapters, such fluorescence-mapped images can provide an accurate depiction of EC distributions on the luminal surface nondestructively and in real time.

## 3.5 System Design

The scanning fiber imaging method requires local excitation of the fluorophores using the fiber mirror and the detection of fluorescent signals generated at each mirror location. A diagram and photograph of the imaging platform that can accommodate the mapping algorithm in Section 3.4 is shown in Fig. 3.8(A) and Fig. 3.8(B), respectively. $\lambda$=473 nm laser light was coupled into an optical fiber and delivered to the sample's ROI by the fiber micro-mirror within the MIC. The laser was operated at a continuous 1mW, with a fiber injection efficiency of ˜15%. The movement of the fiber mirror was controlled by a custom-built two-axis motorized scanning system consisting of a 0.1-µm-resolution translation stage (UTM100PP.1HL, Newport, Irvine, CA) and a 20 deg/sec rotation stage (URM80PE, Newport). A fiber clamp was mounted to the scanner that held the fiber in place. The distance from the fiber micro-mirror to the clamp was 15 cm. This system enabled the control of both the angular and the translational forward/backward movement of the fiber micro-mirror using a custom Labview program (National Instruments, Austin TX). The fluorescent responses generated by the fluorophores were collected by a 2x long working distance lens (M Plan Apo 2, Mitutoyo) and captured by the EM-CCD camera (iXon, Andor Inc., Belfast). The distance between the lens and the phantom was 10 cm. For fluorescence mapping, the camera was set to a full-binning mode where the EM-CCD chip's pixels were internally summed together to provide the total fluorescence intensity. In principle, we can replace the camera with a single detector such as a photomultiplier tube. However, a camera is required quantify fluorescence distributions on the scaffold exterior surface for several experiments. A bandpass filter (525/45 BrightLine, Semrock, Rochester, NY) was used to remove the excitation light from fluorescence signals. Figure 3.8(C) shows a parallel plate bioreactor housing a planar scaffold on the imaging platform during the execution of the mapping algorithm.

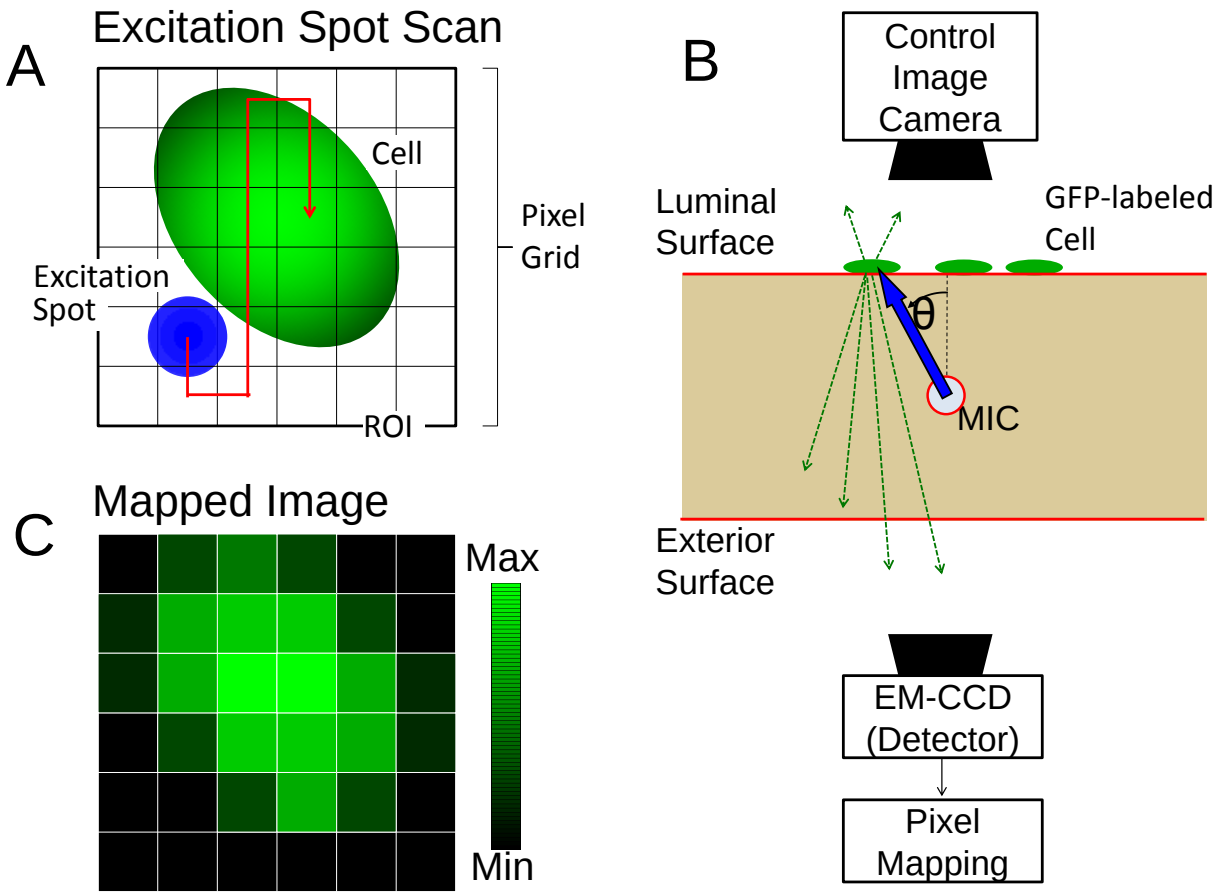


Figure 3.7: Illustration of a 2D pixel grid on the luminal surface of the scaffold containing a GFP-labeled EC (represented by the green oval) and the excitation spot (represented by the blue circle). (B) A schematic drawing illustrating the principle of the imaging method. Through fiber mirror delivery via a MIC, a micron-scale excitation spot is generated on the luminal surface. Within any given excitation spot, a different amount of green fluorescence is generated depending on whether a GFP-labeled EC overlaps with the local pump spot. An EM-CCD camera is used as a sensitive detector to capture the portion of fluorescence light that transmits through the scaffold to the exterior surface. The amount of fluorescence detected by the EM-CCD camera is then assigned to the corresponding imaging pixel. After sequentially scanning the excitation spot over all imaging pixels within the ROI followed by assigning fluorescence intensity measured by EM-CCD camera to each imaging pixel, a mapped image is obtained that depicts the distribution of GFP-labeled ECs on the luminal surface. Note that all imaging instruments required for this process are located on the side of the exterior surface. (C) An illustration of fluorescence-mapped image that corresponds to the configuration shown in (A).

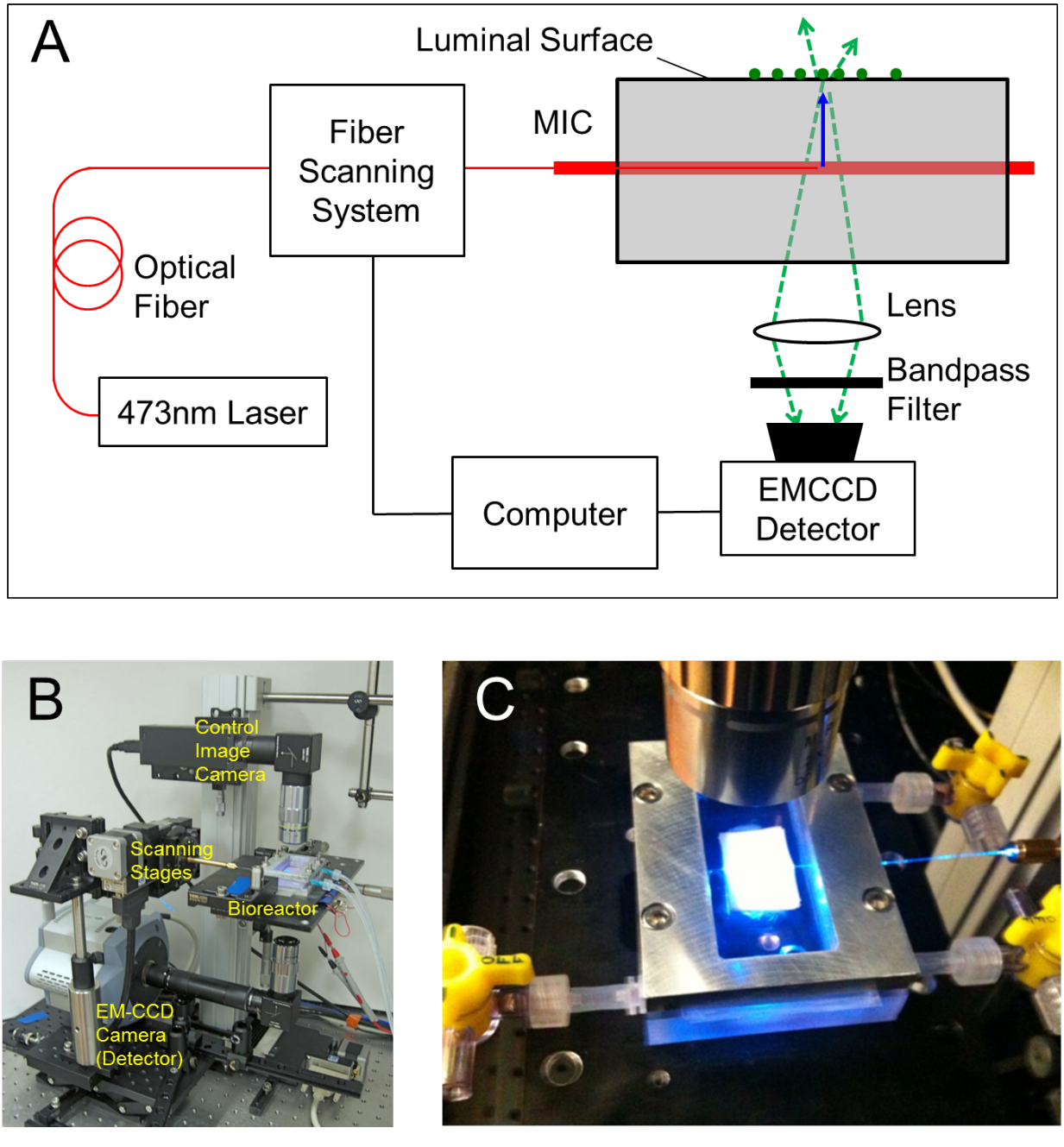


Figure 3.8: (A) Schematic and (B) photograph of the scanning fiber imaging system. (C) A parallel-plate bioreactor on the imaging platform. The fiber mirror is inserted into the MIC.

## 3.6 Control Image Capture

To evaluate the accuracy of the mapped images and to acquire pump light characteristic data, a CCD camera (XCD-X710, Sony, Japan) with a GFP bandpass filter in front was mounted above the bioreactor to capture control images. In Fig. 3.7(B) and Fig. 3.8(B), this CCD camera is represented by the "control image camera". An external 473 nm light source (not shown) was used to illuminate the entire luminal surface and provided excitation light for the control images. The control images were obtained using conventional, direct-line-of-sight fluorescence microscopy, and can therefore be used as the gold standard for image comparison and analysis. By quantitatively comparing the fluorescence-mapped images to the control images, the quality and reliability of the imaging system was calculated using a custom image comparison script written in MATLAB (MathWorks, Natick, MA).

# Chapter 4

# Prototyping

## 4.1 Design Flow

Starting from merely an idea, the imaging system was built from the ground up and refined through the course of four phases in order to meet the design requirements. Briefly speaking, we want to image endothelial cell activity in real time on the lumen of tissue engineered vascular grafts during in vitro preconditioning. There were, however, many untested ideas and concepts in the early phases of imaging system construction. This included testing the feasibility of delivering uniform fluorescence pump light to the luminal surface through the embedded MIC, being able to scan a large enough area to consider the technology practical for its intended use, and testing if a high enough resolution could be achieved to follow cell level interactions. To verify that these important considerations were feasible or at least lent themselves to refinements, we required to go through several testing phases which are outlined in Fig. 4.1. For the first three development phases, we used planar scaffolds to perform a multitude of imaging and characterization tests. After reaching a sufficient level of system refinements, we performed real time *in vitro* vessel imaging using vascular scaffolds.

The first phase was Prototyping (Chapter 4), which involved measuring the pump light behavior of our first scaffold-MIC composite and the implications on resolution. After having a basic understanding of system capabilities, we performed the first image reconstruction experiments using fluorescent microspheres.

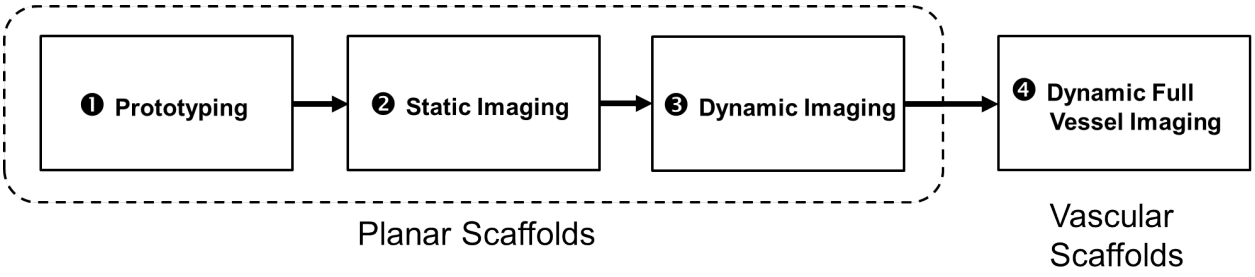


Figure 4.1: Flow diagram outlining the steps taken from the initial imaging prototype phase to the final vascular scaffold imaging experiments.

In the second phase, Static Imaging (Chapter 5), we performed imaging depth measurements with fluorescent microspheres, signal-to-noise and resolution measurements, and finally produced our first reconstructed images of cells in a bioreactor at a single, static, time point.

The third phase, Dynamic Imaging (Chapter 6), followed up from the previous chapter by using a heated bioreactor, enabling the image reconstruction of cells over multiple hours time points. By producing time lapse reconstructed images of the cells over the luminal surface, we were able to monitor cell morphological behavior in real time. The accuracy of our reconstructed images were cross verified using control images taken with a separate camera.

Finally, in the last phase, Imaging the Vascular Lumen, (Chapter 7), we performed the image reconstruction of endothelial cells in vascular grafts in both parallel plate bioreactors and in a specially designed pulsatile-flow bioreactor. Upon producing the time lapse reconstructed images in these bioreactors, we achieved the desired result for which this project was set out to solve.

## 4.2 Planar versus Vascular Scaffold

In the first three phases, we used planar scaffolds instead vascular (tubular) scaffolds to perform our tests. This was based on the experimental inconvenience of using vascular scaffolds. As illustrated in Fig. , fluorescent labeled ECs exist only on the innermost layer (i.e., lumen) of the vascular scaffold. Consequently, it is difficult to apply direct-line-of-sight optical microscopy to visualize luminal fluorophore distributions through the optically opaque scaffold. Yet, in order to perform the various tests, we needed to compare the results obtained through fiber scanning with a common standard such as direct-line-of-sight microscopy. To resolve this quandary, we created

an equivalent phantom by "flattening" the tubular vessel and converting it to a planar structure, as illustrated in Fig. X. Because ECs cover only the innermost surface of a blood vessel, they will exist only on one side of the "flat" vessel surface, which is referred to as the "luminal" surface.

Note that the objective lens and all other instruments required for MIC-imaging should be placed outside of the animal body as indicated by the "detector". Hence we denote the surface opposite of the luminal surface as the "exterior" surface. With these considerations, the scaffold used in phase , , and is composed of a planar scaffold with one or more embedded MICs and multiple fluorophores placed on the luminal surface. With the configuration depicted in Fig. X, we easily obtained the direct-line-of-sight control images that accurately depict the distributions of fluorophores on scaffold lumen. Physical properties of the phantom such as scaffold porosity and optical coefficients were kept equivalent to the vessel scaffolds used for carotid artery engineering.

## 4.3 Prototyping Overview

The prototyping experiments were performed in two steps. First, a preliminary test was performed to characterize the pump spot on the luminal surface using a planar scaffold with a single embedded MIC. This aided in the calibration of scaffold related parameters, in testing software performance (i.e. automation of translation and rotation stages), and in determining the potential resolution and dimensions of the ROI of the scaffold-MIC composite.

A second scaffold with identical thickness was then fabricated but with four MICs embedded in parallel. Using knowledge gained from the first test, the distance between individual MICs was determined by analyzing the pump spot measurements so that there was minimal overlap between each individual MIC's ROI. A random distribution of fluorescence microspheres was then placed on the planar scaffold's luminal surface. The microsphere spatial distribution was subsequently reconstructed using the fiber scanning protocol outlined in Section 3.4, which produced the first images obtained by "looking through" the optically thick and diffuse scaffold.

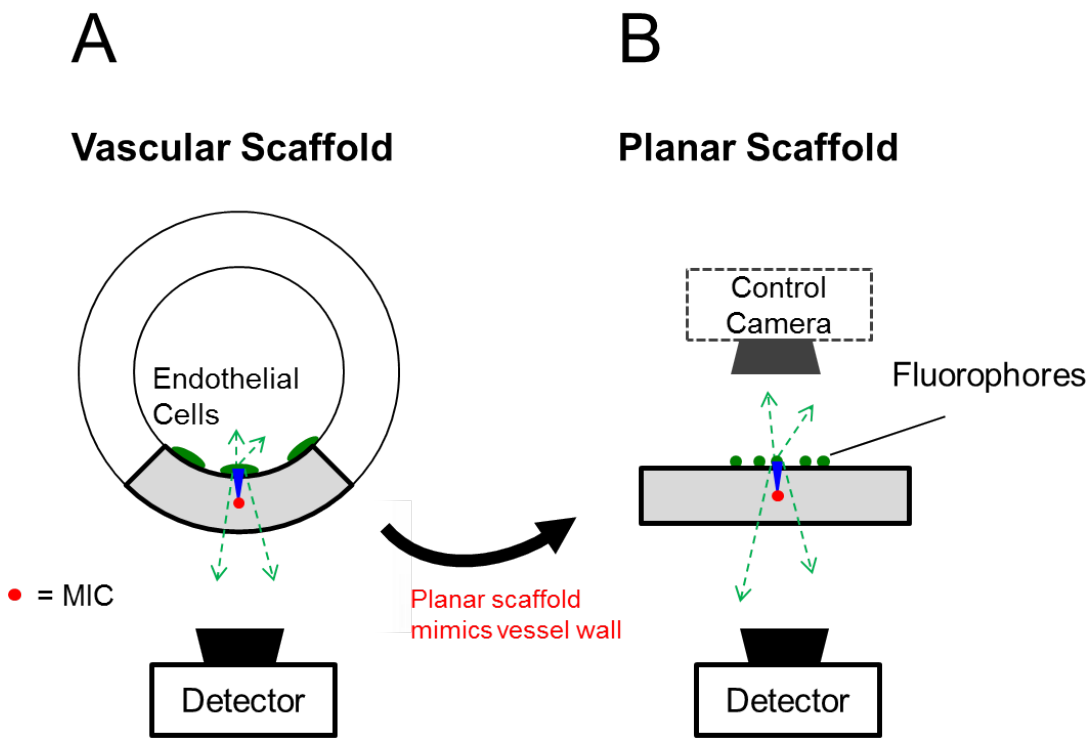


Figure 4.2: The model scaffold in (B) can be regarded as the result of "unwrapping" the tubular scaffold in (A). The MIC is embedded into the scaffold wall allowing controlled localized delivery of fluorescence excitation light. By scanning the excitation light across the lumen of the vessel and capturing the cell-emitted fluorescence responses from the exterior surface, the original cell distribution of the luminal surface can be reconstructed via signal processing. All imaging hardware for our imaging method is grouped in "imaging system" in the figure and is located on the side of the exterior surface. For quantitative comparison with the control images, a planar scaffold was fabricated to allow direct-line-of-sight access to the luminal surface using a conventional optical microscope (control image camera). Both before and after unwrapping, the imaging system configuration remains the same. The control image camera captured images of cell distribution using conventional, direct-line-of-sight, fluorescence microscopy. Such images were denoted as control images and used to validate our imaging method.

## 4.4 Pump Spot Characterization

Once pump light is launched from the micro-mirror inside the MIC towards the luminal surface, it immediately experiences optical absorption and scattering upon transitioning from the MIC to the scaffold. Consequently, the full-width half-maximum (FWHM) of the pump beam profile generally increases as a function of propagation distance in the scaffold. Since the spatial resolution of our imaging system is highly dependent on the pump profile on the luminal surface (pump spot), it is necessary to investigate the relationship between the fiber micro-mirror launching angle $\vartheta$ and the generated pump spot location and dimension. As defined in Section 3.4, the R axis is parallel to luminal surface and the T axis is parallel to the MIC, while the launching angle is defined such that $\vartheta = 0$ denotes the case where the pump light is launched directly towards the luminal surface. These parameters are again illustrated in Fig. 4.3A.

To measure the pump spot profile on the luminal surface when varying the launching angle, we used the configuration illustrated in Fig. 4.3B, where the red dot indicates the MIC placement relative to the luminal and exterior surface. The planar scaffold thickness was ~ 1 mm and the MIC was embedded ~ 0.5 mm from either surface using the fabrication method described in Section 3.1. The pump spot profiles were captured using the system's control camera. The optical filters were removed from the camera to allow the pump light to pass through. Prior to testing, we soaked the scaffold with DMEM/F-12 (Invitrogen) growth media (a common culture media used for cells) to provide realistic optical properties.

The fiber mirror was then scanned in 1° increments from $\vartheta$ = - 60° to + 60° to deliver pump light to the luminal surface while the control camera took images of the pump spot at every incremental position. Figure 4.4A shows several pump spot profiles with their peak cross section in the R axis and T axis, each obtained using a different launching angle $\vartheta$. We see that the pump spot intensity "flattens" out when the launching angle is moved from $\vartheta = 0°$. This behavior, which was expected due to scattering and absorption effects, shows the intrinsic limitation in the accessible pump spot positions on the R axis. Figure 4.4B shows in more detail that as $|\vartheta|$ increases, the FWHM of the pump spot profile increases while the overall intensity decreases. At larger launching angles $\vartheta$ the pump beam must travel a longer distance before it reaches the scaffold surface, thereby undergoing more scattering and absorption along the way. In our studies, we observed that the pump spot is slightly elongated along the R axis direction. We attribute this elliptical profile to a slight lensing effect caused by the cylindrical geometry of the MIC. Finally, in Fig. 4.4C we see that the center

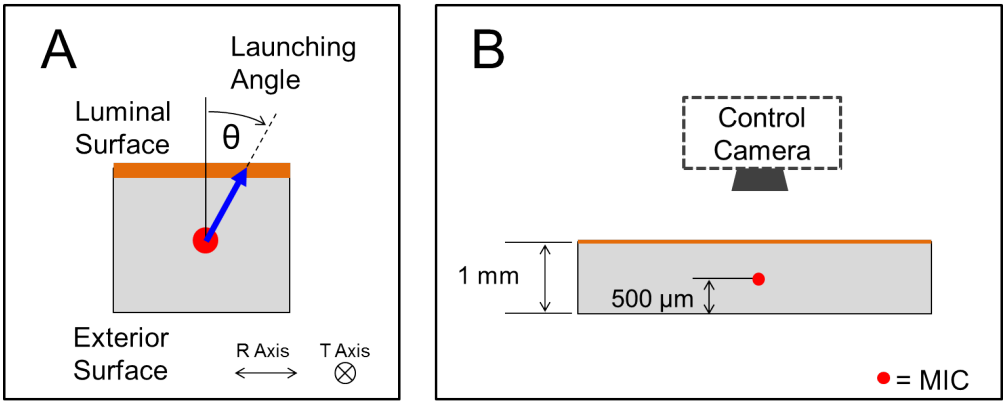


Figure 4.3: (A) Schematic of scanning parameters: The luminal surface mimics the inside of the vessel. The exterior surface represents the outside surface of the vessel. The launching angle $\vartheta$ is the direction at which the pump light enters the scaffold from the MIC, where $\vartheta = 0$ denotes the case where pump light is launched directly towards the luminal surface. The R Axis is parallel to the luminal surface and the T Axis is parallel to the MIC's axial direction. (B) Configuration of MIC-scaffold composite to characterize the pump spot in the prototyping experiments.

of the pump spot has an almost linear dependence on the launching angle $\vartheta$. Taken together, the results in Fig. 4.4 indicate that for a distance of 500 µm between MIC and luminal surface, the pump spot can be moved by about 700 µm (350 µm on either side of $\vartheta = 0°$) on the surface in the R axis. The pump spot dimension ranged between 200 - 300 µm, which is one order of magnitude greater than the size of endothelial cells.

## 4.5 Image Reconstruction

By using the information obtained in Fig. 4.4, we can link the fiber mirror's position and angular orientation inside the MIC with the center of the pump spot on the luminal surface. For any given MIC, the position of the fiber mirror can thus be uniquely identified by its T axis coordinate x and the its rotation angle $\vartheta$. The rotation (launching) angle $\vartheta$ is linked to the R axis and this relation is shown in Fig. 4.4C. From Fig. 4.4C, we see that the center of the pump spot depends nearly linearly on the fiber rotation angle $\vartheta$. Therefore, for any fiber mirror position (x, $\vartheta$), we can immediately deduce that the center of the pump spot on the lumen surface is located at (x, c $\times$ $\vartheta$), where c is 0.006 mm/°. This parameter is of significant importance for setting the scanning positions with the control software.

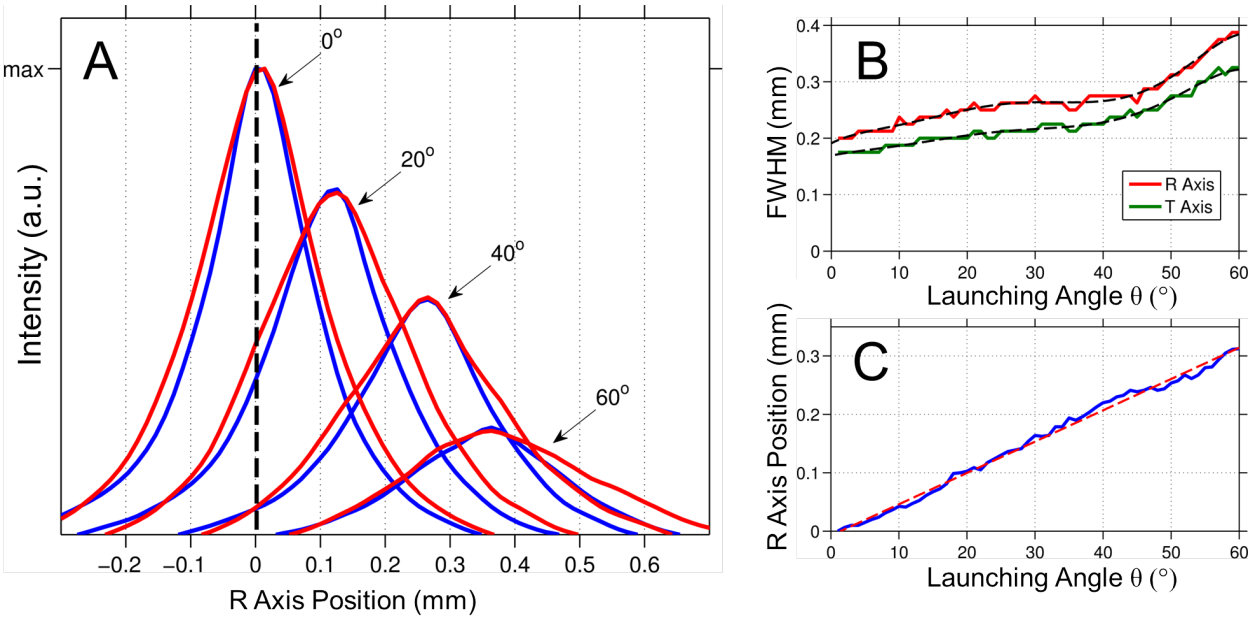


Figure 4.4: (A) Pump spot profiles at different launching angles $\vartheta$. (B) Full-Width-Half-Maximum of the pump spot profile versus $\vartheta$. The FWHM increases from 200 µm at $\vartheta = 0°$ to 300 µm at $\vartheta = 60°$ (C) The relationship between the center position of the pump spot versus the launching angle $\vartheta$ is nearly linear.

We further note that a MIC inside the scaffold can provide only a limited field of view along the R axis, since the radius of the pump spot increases as we increase the launching angle $\vartheta$. To ensure a sufficiently high imaging resolution for each MIC, we chose a rectangular imaging window (ROI) of 0.7 mm × 10 mm along the R and T axis, respectively. The 0.7 mm R axis dimension is selected such that that for each MIC, we only need to rotate the fiber mirror from -60° to 60°. If the fiber launching angle $\vartheta$ is greater than 60°, the pump light becomes too diffuse to achieve a useful imaging resolution.

Based on this information, we fabricated a new scaffold with the dimensions illustrated in Fig. 4.5A, but unlike in the previous experiment, we used four MICs in parallel. This allowed us to extend the effective ROI fourfold. The scaffold was fabricated according to Section 3.1. The MICs were placed 0.7 mm from each other to create minimal overlap between each MIC's ROI. Prior to sintering, the MICs were arranged and held together with silicone adhesive (Dow Corning), so that their relative distance does not shift during sintering and experimentation. Figure 4.5B shows a photograph of the scaffold with the four embedded MICs.

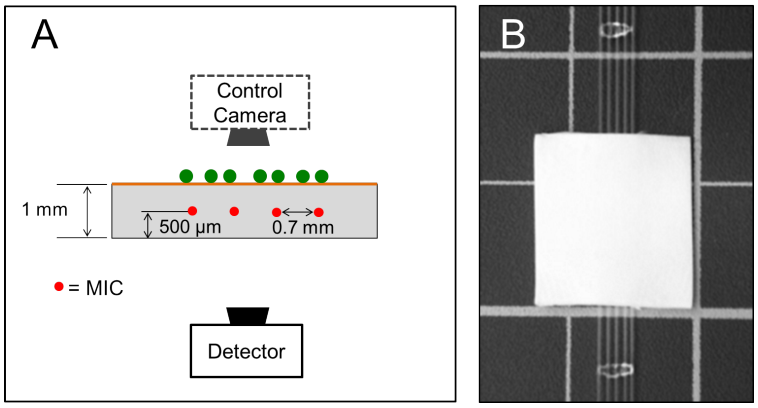


Figure 4.5: (A) Schematic showing the scaffold-MIC configuration used for imaging a random distribution of 90 µm dia. fluorescent microspheres on the luminal surface. Four MICs are placed in parallel to extend the effective ROI of the scanning devices. (B) Photograph of the fabricated planar scaffold with the four embedded MICs.

### 4.5.1 Microspheres as Reconstruction Targets

To test the system prototype's image reconstruction capability, we used green fluorescent microspheres (90 µm diameter, Spherotec Inc.) as reconstruction targets on the luminal surface. Using microspheres instead of cells significantly reduces the complexity during prototyping by avoiding the need for sterilization, cell nutrient delivery, and further important factors required for live-cell imaging, while maintaining a nearly identical system from an optical standpoint. Using a 20G needle tip, the microspheres were extracted from a water suspension and then brushed onto the luminal surface within the ROI of the MICs. The random distribution of green fluorescence microspheres then mimicked the distribution of GFP-labeled ECs on the luminal surface. To capture the microsphere distribution, we took a control image using the direct-line-of-sight control camera as illustrated in Fig. 4.5A, producing the microscopy image in Fig. 4.6A.

### 4.5.2 Image Reconstruction

By embedding four MICs in parallel within the scaffold (denoted as Channel 1 through 4), we extended the effective ROI fourfold as discussed above. Taken together, the four MICs in parallel provided a combined scanning window of 2.8 mm × 10 mm, which is sufficient for most of tissue engineering studies. This combined ROI was then divided into 52 × 200 imaging pixels (i.e. 13 ×

200 pixels per MIC in the R axis and T axis, respectively), which corresponds to a single pixel size of 54 μm × 50 μm. The pixel size was chosen to be approximately a fourth of the FWHM of the pump spot at $\vartheta = 0°$ to guarantee a smooth transition between the targeted imaging pixels. After running the scanning reconstruction protocol for each of the four MICs separately, we plotted the pixel response images. By placing the images side-by-side and merging them together into one image, we created the composite image shown in Fig. 4.6B. The individual MIC reconstructed images are labeled as Channel 1 through 4 and shifted along the T axis to match the control image in Fig. 4.6A.

When comparing the control image with the reconstructed image, we observe that the center position of each microsphere is in excellent agreement. In order to estimate the spatial resolution of our reconstruction method, we employ the following rationale: The scanning of the pump spot over the entire lumen surface is analogous to the control image being convolved by a two-dimensional Gaussian function (smoothing filter). Since, the pump spot intensity profile closely resembled a Gaussian copula (Fig. 4.4A), so we used a Gaussian filter kernel with a FWHM of 250 μm and convolved it over the digitized control image in Fig. 4.6A. The resulting theoretical image is shown in Fig. 4.6C, which matches well with the reconstructed image.

## 4.6 Conclusion

The study presented in this chapter gave us an initial estimate of the feasibility of our idea. There are several crucial pieces of information that we were able to extract. For one, if we were to use multiple MICs to extend the scanning window on the luminal surface, we would require a landmark on the T axis prior to scanning. This would enable us to line up individual reconstructed MIC images to match the actual fluorophore distribution without knowing the "solution" to the latter. Such a landmark could be provided using a different fluorescent color microsphere to signify the start or end location on the T axis. Other intrinsic features of the scaffold-MIC composite could be used as landmarks, such as the edge of the scaffold or a marking on each MIC.

Nonetheless, the reconstructed image in Fig. 4.6B demonstrates that the principle idea of reconstructing a fluorophore distribution using our imaging technique is indeed feasible. When comparing the reconstructed image with the control image, there is good overlap with the positions of the features. However, from simple observation, there clearly presents a need to improve the system

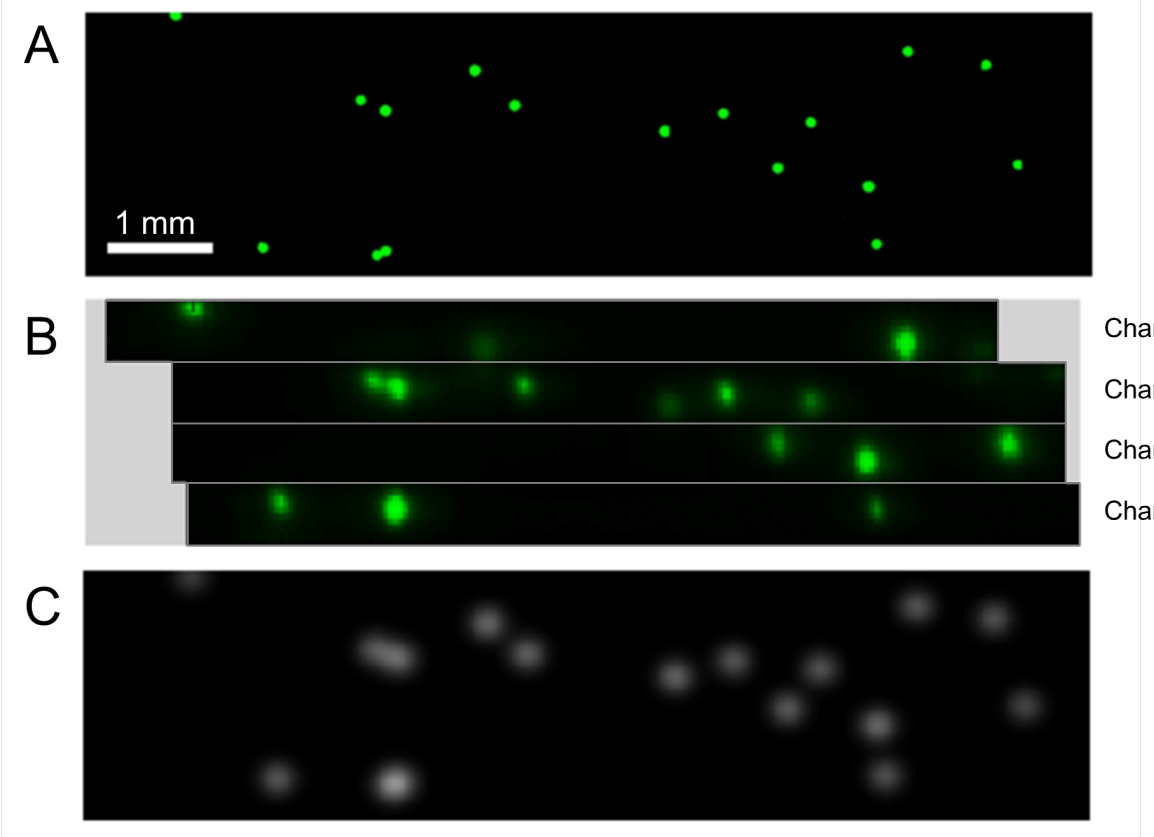


Figure 4.6: (A) Control image showing the spatial distribution of the randomly dispersed 90 μm green fluorescent microspheres. This image was taken with the direct-line-of-sight control camera for result verification. (B) Reconstructed images for each Channel after running the fiber scanning protocol by capturing the signals using the detector. The reconstructed image of each MIC is labeled Channel 1 through 4 and placed side-by-side. The position of each image in the T axis was adjusted to match the control image. By comparing the composite reconstructed image to the control image, we demonstrate that the positions of the microspheres could be determined accurately. (C) A theoretically reconstructed image obtained by convolving the control image in A with the average pump spot profile. The theoretical and experimentally reconstructed image matches well, indicating that the resolution of the imaging system depends on the pump spot dimension.

resolution in order to reach the required level to make our technology useful to tissue engineering studies. Ideally, the system should provide single-cell level resolutions, so the next step was to improve the reconstruction resolution.

When comparing the reconstructed image with the theoretical image, there is good overlap with the dimensions of the features. Although the microspheres are not ideal point sources (i.e. infinitely small one-dimensional sources), they behave very similar since the pump spot is roughly 2.5 larger in diameter than the microspheres, giving validity to the theoretical image in Fig. 4.6C. As a result, the pump spot profile in Fig. 4.4A effectively determines the resolution of our system, which is at around 250 μm. Consequently, in order to improve the spatial resolution of our system we require finding ways to decrease the FWHM of the pump spot. An improvement in resolution could be achieved by embedding the MIC closer to luminal surface, thereby having the pump light undergo less scattering on its path to the surface. This consideration was tested in the next phase of the project – Static Imaging.

# Chapter 5

# Static Imaging

## 5.1 Overview

From the prototyping experiments in the previous chapter, we concluded that in order to increase the image reconstruction resolution, we would require to reduce the size of the pump spot. A simple way of achieving this is to move the MIC closer to the luminal surface. This principle idea was tested by fabricating a new scaffold-MIC composite with the MIC shifted closer to the luminal surface and performing a pump spot characterization experiment.

Next, we used the new scaffold-MIC configuration and tested the effect of scaffold / tissue thickness on the image reconstruction resolution. Theoretically speaking, a major advantage of our method is that the link between imaging resolution and imaging depth is "decoupled", making it possible to greatly increase imaging depth without significantly sacrificing resolution. To confirm this, a test was performed in two steps: First, we used the planar scaffold to perform image reconstruction with fluorescent microspheres. The experiment was performed such that it mimicked a vessel inside a bioreactor during *in vitro* preconditioning. Next, a piece of thick porcine skin was added below the scaffold to simulate an *in vivo* configuration. After reconstructing the fluorophore distributions for both configurations, we compared the two results. The resolution and contrast (i.e. SNR) of the reconstructed images were subsequently determined and compared. To better understand the dominating factors that limit the imaging depth, we investigated the optical properties of

the scaffolds. From these measurements, we identified the theoretical maximum penetration depth for imaging.

Lastly, based on the ability to reconstruct microsphere distributions, we performed our first image reconstruction using cells. To reduce the complexity of the experiment, this was implemented in a static environment inside a bioreactor, but without providing the appropriate temperature for cell culture. After reconstructing cellular distributions at cell level resolutions, we drew our conclusions and prepared to move to dynamic imaging.

## 5.2 Pump Spot Characterization

A new scaffold-MIC composite was fabricated using the method in Section 3.1. The planar scaffold thickness was 500 μm and the MIC was embedded 250 μm from the luminal surface as illustrated in Fig. 5.1. By embedding the MIC closer to the luminal surface, we expected the pump spot diameter to decrease, thereby increasing the system resolution. This was verified by quantifying the parameters of the pump spot as a function of the fiber mirror launching angle $\vartheta$. The control camera in Fig. 5.1was then used to obtain the results shown in Fig. 5.2. Prior to the experiment, the scaffold was soaked in EGM-2 and then placed on a microscope slide on top of the imaging platform. After inserting the fiber mirror, the launching angle $\vartheta$ (defined in Fig. 4.3A) was swept from -50° to +50° in 1° increments on 5 different positions on the T axis. The characteristic data of the pump spot presented in Fig. 5.2 shows both the average as well as the standard deviation of the results obtained from the 5 distinct T axis locations.

Figure 5.2A shows the FWHM of the pump spot size as a function of the launching angle $\vartheta$. Several intensity profiles of the pump spot on the luminal surface are also shown in the figure as insets. It is clear that the FWHM increased as the launching angle deviated from $\vartheta = 0°$. As discussed previously, this phenomenon can be explained by the fact that at the angle of $\vartheta = 0°$, pump light photons encountered the least number of scattering events on their path through the scaffold to the luminal surface. As the angle $|\vartheta|$ increased, pump light photons traveled a longer distance to the lumen, thereby experiencing more scattering within the scaffold. As a result, the FWHM of the pump spot increased as a function of the launching angle $\vartheta$. For the scaffold-MIC composite illustrated in Fig. 5.1, the pump spot FWHM was 21 ± 0.8 μm at $\vartheta = 0°$ and increased by roughly 2.5 times to 50 ± 8.2 μm at $\vartheta = \pm 50°$.

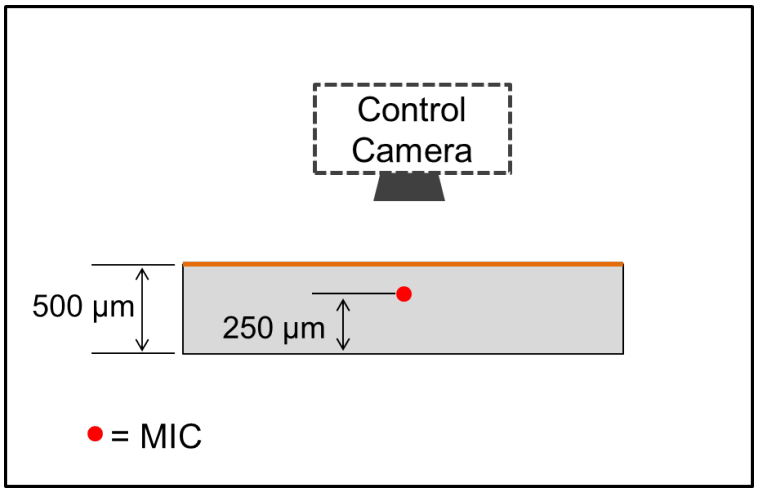


Figure 5.1: Configuration of MIC-scaffold composite to characterize the pump spot in the static imaging experiments. The MIC was moved closer to the luminal surface to decrease the pump spot diameter, which increases the reconstruction resolution.

In Fig. 5.2B, we show that the total intensity of the pump spot decreased as $|\vartheta|$ increased. The intensity value was calculated by summing all control camera pixel counts within the pump spot (i.e. inset in Figs. 5.2A). A possible explanation for this behavior is that at a larger launching angle $|\vartheta|$, the pump light photons traveled a longer distance, therefore experiencing more absorption before reaching scaffold lumen. Since the fluorescence response has a linear dependence on pump light intensity, the fluorescence signals captured during fluorescence mapping must be renormalized as follows: At each $|\vartheta|$ value, the magnitude of the fluorescent signal was boosted according to the curve in Fig. 5.2B so that the "renormalized" pump light intensity remains constant for all pixels.

Figure 5.2C shows that along the R axis, the center position of the pump spot depends almost linearly on the fiber mirror launching angle $\vartheta$. Using a linear fit, we can relate the position of the pump spot along the R axis versus the launching angle as $R(\vartheta) = 3.33 \times \vartheta$. This result indicates that for this phantom, the pump spot can scan across a distance of 400 μm (200 μm on either side of $\vartheta = 0$) on the lumen along the R axis, with a FWHM ranging from 21 to 50 μm. As in the previous experiments, the scanning range along the T axis is virtually unlimited.

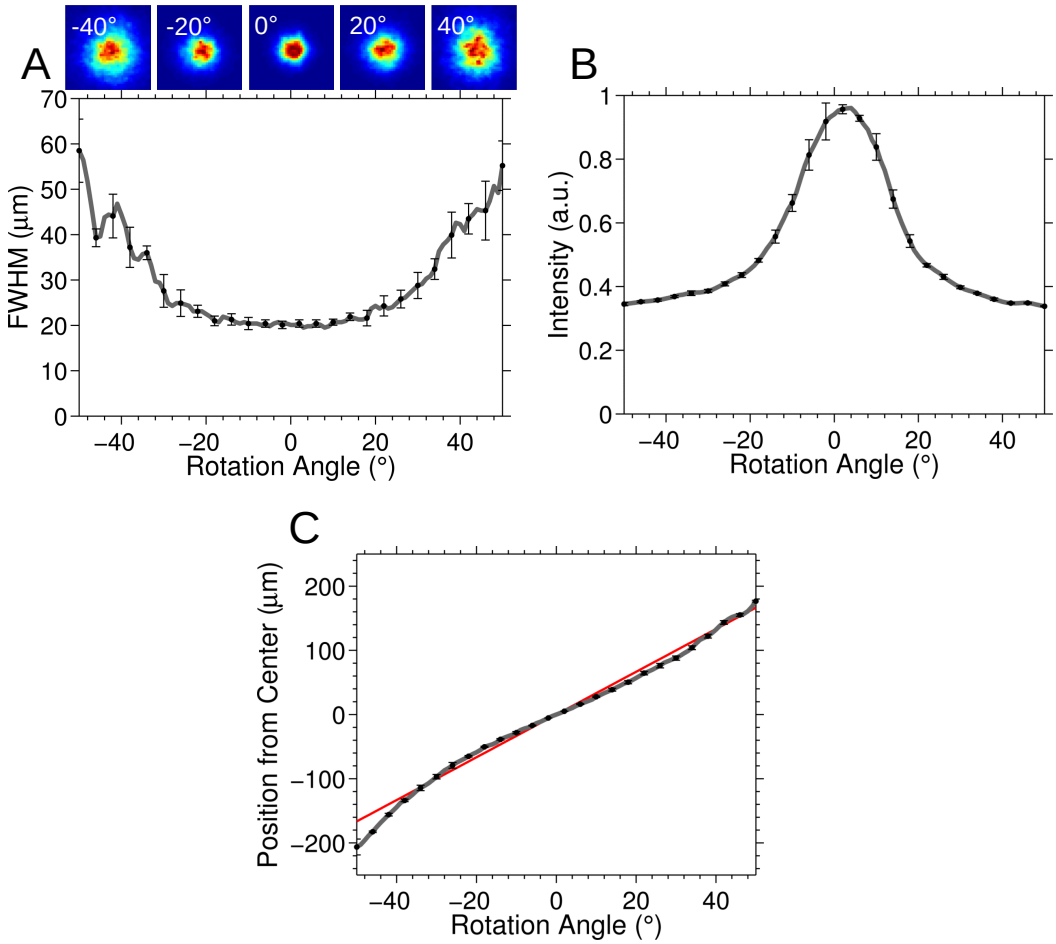


Figure 5.2: Pump spot characterization: The plot lines are in 1° increments and the error is shown at every 4th point to prevent plot overcrowding. Error bars represent ± one std. dev. centered at the mean of the 5 trials. (A) The FWHM of the pump spot intensity profile on scaffold lumen is shown with respect to the launching angle $\vartheta$. The insets depict the actual pump spot profile with $|\vartheta|$ equal to 0°, 20°, and 40°, respectively. (B) The intensity of the profile (summed pixels) shows a diminishing pump spot intensity at increasing angles $|\vartheta|$. (C) The pump spot profile center position on the R axis is shown to behave nearly linearly with respect to $|\vartheta|$. From the results, we find that $R(\vartheta) = 3.33 \times \vartheta$ based on a linear fit (red).

## 5.3 Imaging Depth versus Mapping Resolution

### 5.3.1 Procedure

To test the effect of tissue thickness on the image mapping resolution, we used the experimental configuration illustrated in Fig. 5.3. This experiment was performed in two steps with the same scaffold-MIC composite that was used during pump spot characterization (500 μm thick; 250 μm from MIC to luminal surface). First, the planar scaffold was used to perform image reconstruction using green fluorescent microspheres. This experiment configuration mimicked a vessel inside a bioreactor during in vitro preconditioning, assuming that the detector has a direct-line-of-sight to the exterior surface of the scaffold in a bioreactor. Next, a 3mm thick piece of porcine skin was added below the scaffold to form the phantom illustrated in Fig. 5.3. The presence of the optically thick porcine skin mimicked an *in vivo* condition, where the presence of additional obstructive biological tissues, such as the skin of an animal, must be included in order to account for additional photon scattering and autofluorescence. After reconstructing the fluorophore distributions for both configurations, we compared the difference between the two results in terms of resolution and contrast (i.e. SNR).

### 5.3.2 Incorporating Fluorescent Microspheres

The scaffold-MIC composite illustrated in Fig. 5.3 was covered in a random distribution of fluorescent microspheres. We used 28 μm diameter microspheres coated with a green fluorescent dye (FP-30052-5, Spherotech Inc., Lake Forest, IL) to mimic GFP-labeled ECs. First, the microspheres were suspended in deionized water at a 1:10 volume ratio. Next, we pipetted 1 ml of the solution onto the lumen of the phantom, which lead to a random dispersion of the microspheres. Due to experimental handling of the sample, we required to fix the microspheres to the luminal surface. To securely attach the microspheres to the scaffold surface, a thin ˜10 μm layer of additional PDLLA was electrospun on top of the microspheres. The added layer was thin enough to be optically transparent, yet sufficiently strong to eliminate any change in microsphere pattern during extended handling of the planar scaffold sample.

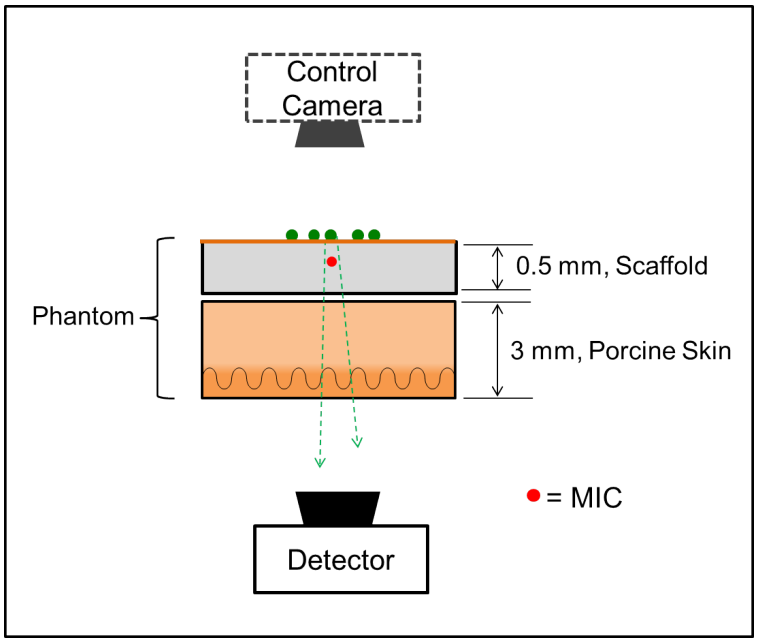


Figure 5.3: Experiment configuration mimicking a vascular preconditioning environment. Using only the scaffold, an in vitro configuration was achieved, where we assume the detector has direct-line-of-sight access to the exterior surface in a bioreactor. To mimic an in vivo configuration, a 3 mm thick piece of porcine skin was added between the scaffold and the detector. This configuration is similar to that found when the carotid artery graft were sutured into an animal and covered by the animal's neck skin, preventing the detector from directly accessing the graft.

### 5.3.3 Image Reconstruction

To cross validate the accuracy of our imaging method, we first captured a control image of the fluorescent microsphere distribution on the luminal surface. As discussed in Section 4.2, the control image was obtained using a standard optical microscope setup to provide an unobstructed, direct-line-of-sight, view of the luminal surface.

Prior to imaging, the sample was soaked with EGM-2. Next, the scaffold / phantom was securely fastened onto a glass slide. The slide with the scaffold was then placed on the imaging platform and the fiber mirror was inserted into the MIC. Fiber scanning was carried out in the ROI that coincided with the control image shown in Fig. 5.4A.2. After following the fiber scanning and mapping procedure described in Section 3.4, we obtained the mapped image shown in Fig. 5.4B.2. This configuration mimicked an *in vitro* environment of a bioengineered blood vessel with visual access to the outside surface of the vessel. When comparing the control image with the mapped image, we observe that the center position of each microsphere is in good agreement. Since the FWHM of the pump spot is at times larger than the microsphere diameter, individual microspheres are blurred together.

Next, a 3 mm thick piece of porcine skin with an intact dermis and epidermis layer was placed under the scaffold, thus further obstructing the luminal surface from the detector. This configuration is shown in the diagram of Fig. 5.4C.1, which mimics an *in vivo* environment for a carotid artery after transplanting into an animal. After the scanning algorithm was performed in the identical ROI, the fluorescence mapped image in Fig. 5.4C.2 was produced. When comparing the fluorescence mapped image using the 0.5 mm PDLLA configuration versus the 0.5 mm PDLLA + 3 mm skin configuration, we observe that there is no significant degradation in image resolution. Therefore, the results in Fig. 5.4 directly demonstrate that the fiber scanning method can decouple the link between imaging depth and image resolution. Fundamentally, this decoupling is due to the fact that our imaging system is not limited by the thickness of the turbid media between the lumen and the detector, but rather depends on the SNR of fluorescent signals. For a detailed analysis of SNR, refer to Section 5.3.5.

To compare how a standard fluorescence microscope performs in terms of resolution, we use the EMCCD camera (detector) to capture the fluorescence images on the exterior surface of the scaffold / skin, where the entire ROI on the scaffold lumen was illuminated using an external pump

light source. The images in Fig. 5.4B.3 and Fig. 5.43.C show the fluorescence response after traveling through 0.5 mm PDLLA and 0.5 mm PDLLA + 3 mm skin, respectively. Both images show that it is impossible to deduce the original microsphere distribution, and that adding an additional turbid medium (porcine skin) causes a significant spread in the spatial distributions of fluorescent signals on the exterior surface.

### 5.3.4 Resolution Analysis

We note that the fluorescence mapping result can be modeled as a convolution of the control image with a point spread function (PSF), where the PSF describes the image "blurring" due to the finite size of the pump spot. Mathematically, the spatial dimension of the PSF should correspond to the overall image resolution of our system. This conclusion was discussed briefly in Section 4.5.2, but is now investigated in more detail.

To quantify the overall image resolution of the fluorescence mapped images in Fig. 5.4, we carried out the following mathematical analysis. First, we convolved the control image with a variable-size Gaussian PSF. We note that the pump spot profile can be closely approximated by a Gaussian PSF. By sweeping the FWHM of the Gaussian PSF from 0 to 50 μm, we obtained various theoretically predicted fluorescence mapped images with an image resolution varying from 0 to 50 μm. Then, the mean square error (MSE) was calculated between the theoretically predicted fluorescence mapped images versus the actual mapped images (i.e., the results shown in Fig. 5.4B.2 or Fig. 5.4C.2). The percentage of MSE versus the FWHM of the Gaussian PSF is plotted in Fig. 5.5, which shows that the smallest MSE occurs at around a 24 μm FWHM for both with or without additional porcine skin. This matches very well with the experimental results shown at in Fig. XA from $|\vartheta| \tilde{}$ 0 – 30 μm. The inserts in Fig. 5.5 show the experimental mapped images (through 0.5 mm PDLLA or 0.5 mm PDLLA + 3 mm skin) as well as the theoretically predicted image using a 24 μm FWHM Gaussian PSF. With this result, we conclude that the resolution of our imaging system can reach the level of 20 – 30 μm with an imaging depth corresponding to 0.5 mm PDLLA scaffold plus 3 mm porcine skin.

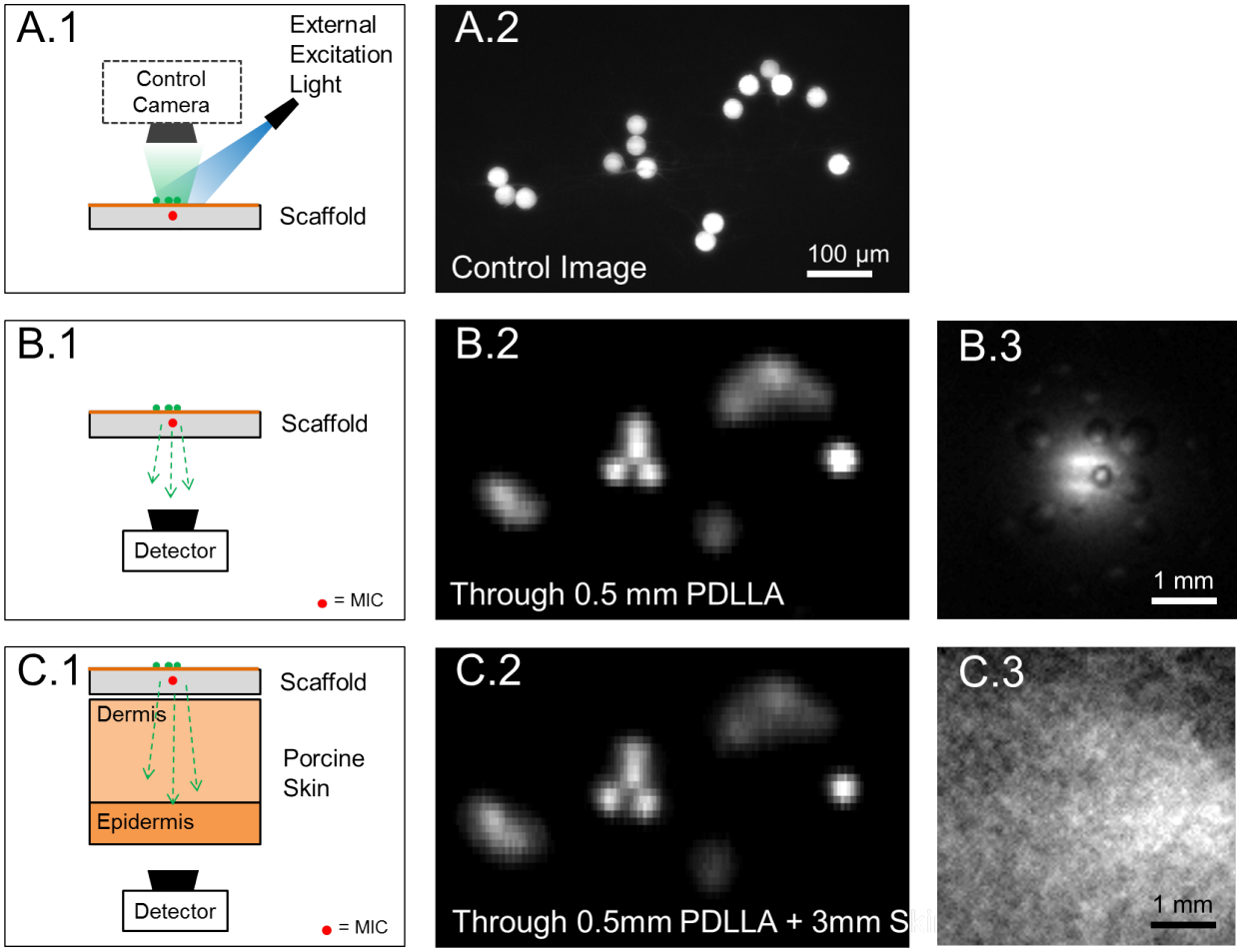


Figure 5.4: Results of fluorescence mapping. (A.1) A schematic showing how we obtain a direct-line-of-sight control image of the scaffold lumen. (A.2) A example of a co ntrol image. (B.1) Configuration for fluorescence mapping through the 0.5 mm thick PDLLA scaffold. (B.2) Mapping result through 0.5 mm PDLLA. (B.3) The spatial distribution of fluorescence signals on the bottom surface of the phantom, as captured by the EMCCD camera. The fluorescent signals were generated by the same ROI in (B.2) under illumination by the external pump light. (C.1) Configuration for fluorescence mapping through the same 0.5 mm thick PDLLA scaffold and a piece of 3 mm thick porcine skin. (C.2) Results of fluorescence mapping through 0.5 mm PDLLA + 3 mm skin. (C.3) Fluorescence image on the bottom surface of the porcine skin as captured by the EMCCD camera. We notice further "blurring" of the fluorescent signal in C.3, yet the result of fluorescence mapping in C.2 remain the same as the result in B.2, which was obtained using only PDLLA scaffold.

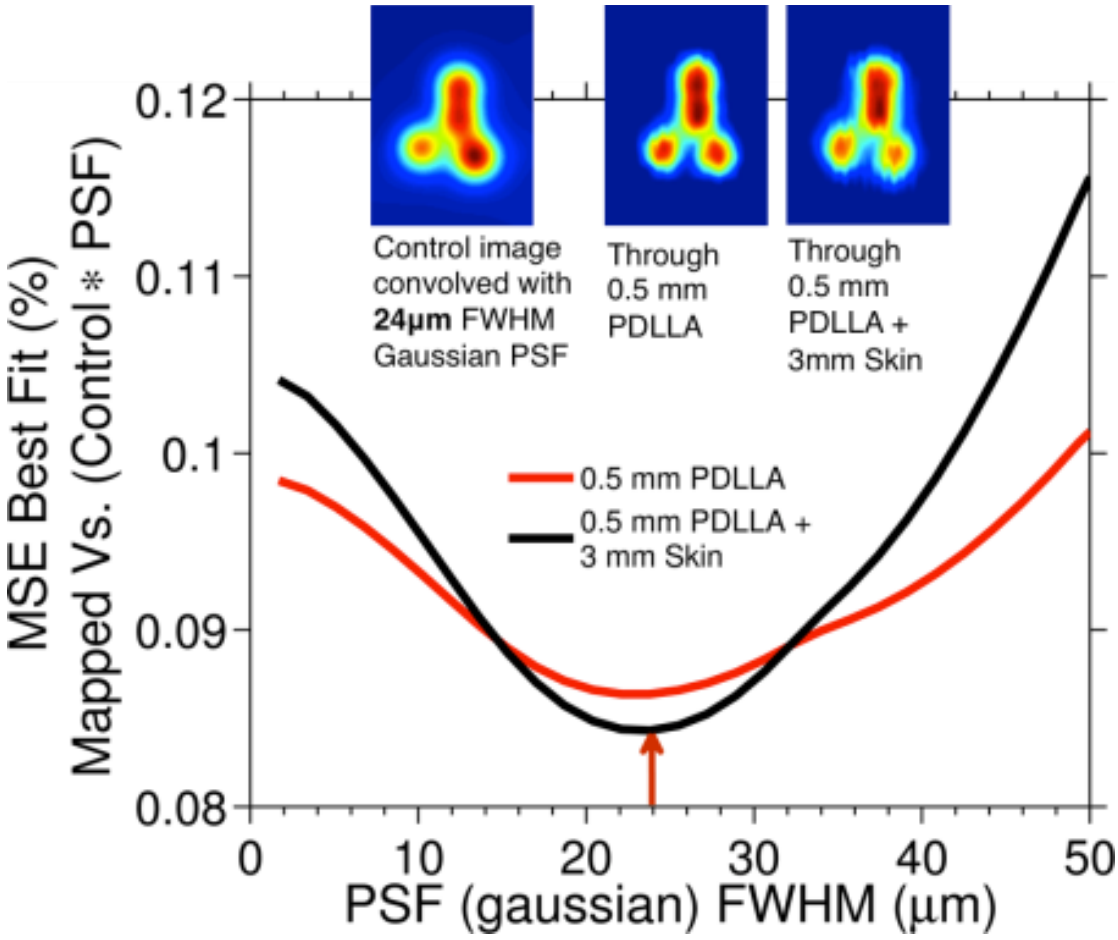


Figure 5.5: The resolution of the fiber scanning method is modeled by convolving the control image with a variable Gaussian PSF creating a theoretical mapped image. By finding the least mean square error of the difference between the theoretical and experimental results, we find the approximate resolution of the system. The result suggests that the imaging resolution is between 20 – 30 µm at an imaging depth corresponding to 0.5 mm PDLLA plus 3 mm porcine skin.

### 5.3.5 Signal Versus Noise

The change in photon fluence measured on the exterior surface is generally very minimal. This can be seen qualitatively by the EMCCD camera intensity plots (Fig. 5.6A) that are typically captured on the exterior surface during imaging. The difference between the pump spot being directly on a single microsphere (signal) and the pump spot being moved away from the microsphere (noise) is typically less than one order of magnitude. To investigate this effect in more detail, the spectra of fluorescent signals as well as "noises" generated by scaffold or porcine skin autofluorescence were measured at the exterior surface by replacing the EMCCD camera with a spectrometer (USB2000, OceanOptics, Dunedin, FL). The imaging system remained the same otherwise.

Figure 5.6 shows the spectral components of the fluorescent signals and noises generated by the microspheres and the two phantoms described in Fig. 5.4A.1 & 5.4B.1, respectively. Using the spectrometer, the microsphere signal was measured by positioning the pump spot to the center of a single standing microsphere and capturing the fluorescence emission spectrum. Then, we applied the same procedure to characterize noises generated by the optical phantoms . To ensure that only "noise" was captured by the spectrometer, we positioned the pump spot on a luminal surface location that was void of any microspheres (We used the control camera to ensure no fluorescent microspheres exist within the pump spot). The results are shown in Fig. 5.6A & Fig. 5.6B, where we normalized the intensity of all emission spectra such that the peaks of the spectral noise were set to be 1.

We define the SNR of the imaging system as the ratio between the microsphere signal and the background noise. For the 0.5 mm PDLLA experiment, the SNR is around 4 in the 510 – 540 nm range. After adding the 3 mm thick skin, the SNR dropped to 2. Although a SNR of 2 is relatively small, it is sufficient to separate the signal from the noise to obtain the fluorescence mapped image in Fig. 5.4C.2. However, if we place a significantly thick tissue between the phantom and the detector such that the SNR approaches unity, it would be very difficult to separate the microsphere signals from background "noises" generated by the scaffold as well as the surrounding tissue.

The results in Fig. 5.6 suggest that the main limitation on fluorescence mapping lies in making sure the intensity of fluorescence signals is greater than the background noise. In other words, the spatial profile of the fluorescent signal captured on the exterior surface of the scaffold or porcine skin plays no role in fluorescence mapping − only the total strength of the fluorescent signal does.

More specifically, after adding the porcine skin, the fluorescence light was distributed within a much wider spatial region (Fig. 5.4C.3) compared to the case without any porcine skin (Fig. 5.4B.3). Yet the images obtained through fluorescence mapping did not show any significant difference. Consider the following two observations: 1) for most biological tissues, optical scattering significantly exceeds optical absorption as shown in Fig. 5.6, and 2) the primary impact of photon scattering is the blurring of the fluorescent signal without significantly changing its total strength. With these considerations, it is clear that the resolution is no longer limited by the scattering of the fluorescent signal. As a result, the imaging resolution of the fiber scanning method is largely "decoupled" from the total imaging depth.

## 5.4 Scaffold Optical Properties

To quantify the optical characteristics of the electrospun PDLLA scaffold, a spectrophotometer (Cary 5000, Agilent Technologies, Santa Clara, CA) coupled with an integrating sphere (Labsphere, North Sutton, NH) was used to measure the reflectance and transmittance values from 450 – 750 nm. The optical measurements were repeated on three scaffold mats having the same thickness as the scaffold in Fig. X (±25 μm std.dev.) but without an embedded MIC. Prior to the measurements, the scaffolds were immersed and saturated in EGM-2, the same cell media used for EC culturing and phantom imaging. From the reflectance and transmittance values, the absorption coefficient $\mu_a$, and scattering coefficient $\mu_s$, were calculated using the inverse adding-doubling algorithm developed by Prahl [3]. For the calculations, we used commonly accepted values for the refractive index ($n$ = 1.38) and anisotropy number ($g$ = 0.9) of the scaffold [4, 5]. We calculate the mean free path (MFP) distance of the PDLLA by using

$$MFP = \frac{1}{\mu_s} \tag{5.1}$$

which models the average distance covered by a photon until a scattering event occurs. A photon undergoing several scattering events can be approximated by the TMFP based on the anisotropy number $g$ (which relates to the degree of forward scattering) and is defined as

$$TMFP = MFP \times \frac{1}{1-g} \tag{5.2}$$

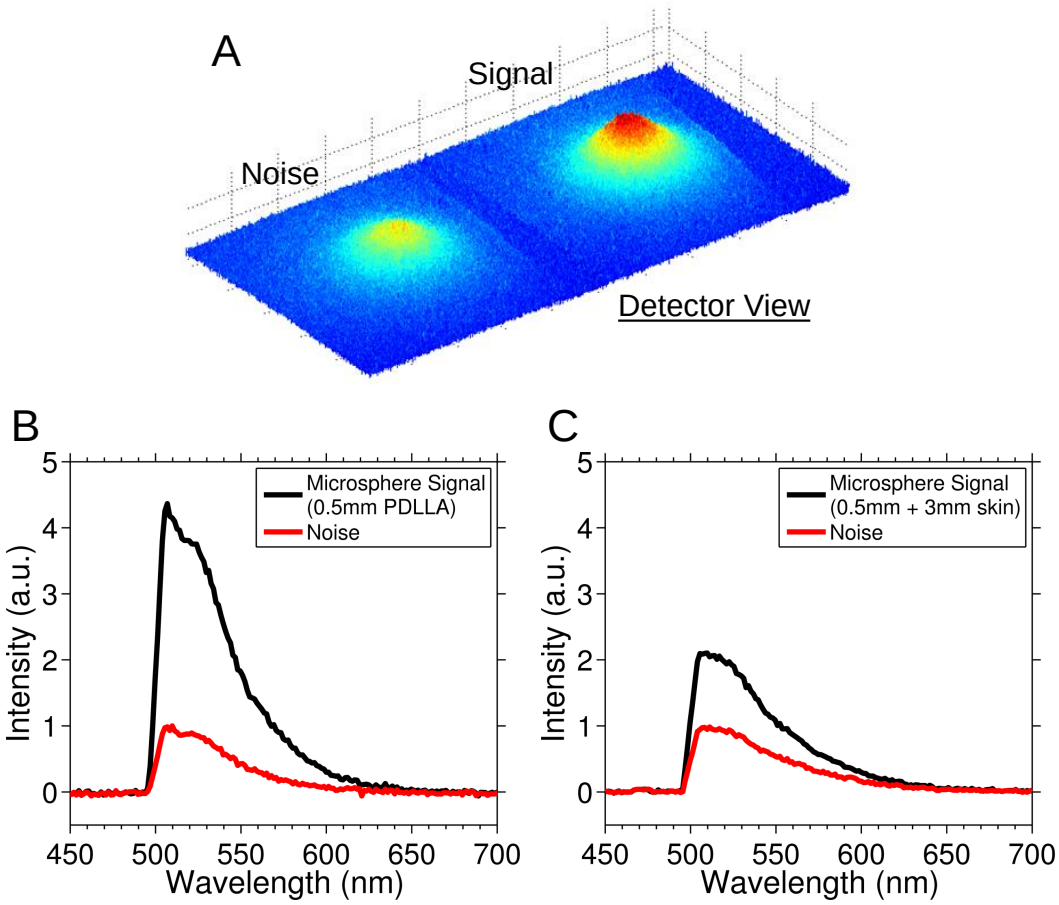


Figure 5.6: (A) Spectral responses of microsphere signals as well as autofluorescence noises. The microsphere signal was obtained by centering the pump spot on a single microsphere placed on the phantom lumen. The autofluorescence noise was obtained by moving the pump spot to a location on the lumen that was free of microspheres. The SNR is calculated as the microsphere signal divided by the autofluorescence. (B) The SNR through 0.5 mm PDLLA is around 4 between 510 – 545 nm. (C) The SNR through 0.5 mm PDLLA + 3 mm porcine skin is around 2 between 510 – 545 nm.

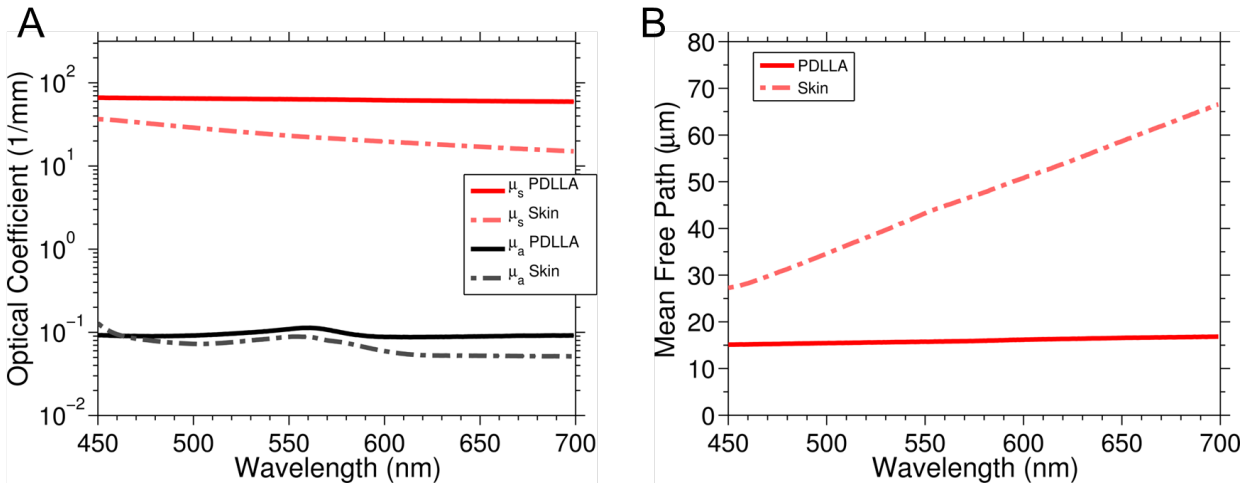


Figure 5.7: (A) The scattering coefficient ($\mu_s$) of PDLLA is found to be roughly double that of porcine skin over the 450 nm – 700 nm range. The results also show that scattering events ($\mu_s$) dominate over absorption events ($\mu_a$) by more than two orders of magnitude. (B) The MFP for PDLLA and for porcine skin.

The optical properties of electrospun PDLLA and porcine skin (dermis & epidermis) were measured between 450 nm – 700 nm to determine their absorption and scattering coefficients $\mu_a$ and $\mu_s$, respectively. Such values quantitatively indicate how strongly the medium absorbs and scatters light. In Fig. 5.7A we see that optical scattering is significantly stronger than optical absorption by more than two orders of magnitude. This result suggests that the resolution of optical imaging is primarily limited by optical scattering in highly turbid biological media.

Using Eq. 5.1, we can calculate the MFP of both the PDLLA and the porcine skin. The same anisotropy factor ($g$ = 0.9) for the $\mu_a$ and $\mu_s$ calculation was used to calculate the MFP, which translates to TMFP = 10 × MFP [3]. Figure 5.7B shows that at the peak fluorophore emission wavelength (510 nm – 530 nm), the MFP is roughly 16 μm for PDLLA and 37 μm for porcine skin. Based on these values, the TMFP is 160 μm for PDLLA and 370 μm for porcine skin. We note that even for advanced modalities such as confocal and two-photon microscopes, the imaging depth is roughly limited to 1 - 2 photon TMFP [5-7], which, in the case of our PDLLA scaffold and porcine skin phantom, is significantly less than their corresponding thickness: ˜ 0.5 mm for PDLLA scaffold and ˜3 mm for porcine skin.

## 5.5 Estimating Imaging Depth Limitations

After exciting a fluorophore with the pump spot, the back propagating light encounters significant amounts of scattering events if the scaffold thickness is greater than 100 μm according to the results in Fig. 5.6A. However, since we merely rely on the sum of the fluency as it appears on the exterior surface, we do not care how the signal profile "looks". Therefore, the amount of scattering encountered by the back propagating signal is largely irrelevant, making absorption the dominant limiting factor to the maximum imaging depth. In short, if all the backpropagating signal light is absorbed along its path to the exterior surface (i.e. if the scaffold is very thick), there is nothing left for the camera image.

Using the values in Fig. 5.6A, we can do a simple estimate of how thick the scaffold or tissue phantom can be without encountering signal ambiguity due to low SNR values. We can calculate the total power absorption $I_\alpha$ (%) using the inverse exponential power law $I_\alpha = I_0 \times (1 - exp(-\alpha \times d))$, where $\alpha$ is the absorption coefficient and $d$ is the distance propagated in the tissue. For example, in the 500 μm PDLLA scaffold-MIC composite illustrated in Fig. 5.3, only 6% of the signal is absorbed when traveling from the luminal surface to the exterior surface. The same calculation can be repeated for the porcine skin to estimate photon absorption. For the 3 mm thick porcine skin, the amount of power absorbed is roughly 26%.

Figure. 5.8 shows a plot of the approximate percent absorption uncounted in both types of tissue versus propagation distance $d$. Although this does not reflect a comprehensive study (i.e. an experimental validation would be more sound), we can estimate that the fluorescence signal light can propagate approximately 10 mm within the scaffold or porcine skin before it encounters significant absorption (˜60% power absorbed). Based on Fig. 5.8, it appears that 1 – 3 cm is a reasonable estimate for how deep the fiber scanning method can reconstruct images through biological tissues and / or scaffolds (at 3 cm, the total absorption is ˜95%).

## 5.6 Image Mapping of Endothelial Cells

After the successful image reconstruction experiments using microspheres, the next step was to use cells as reconstruction targets. Since our estimated resolution using the Scaffold-MIC composite in Fig. 5.1 was between 20 – 30 μm, our use of the similar sized ECs was appropriate. A simple static

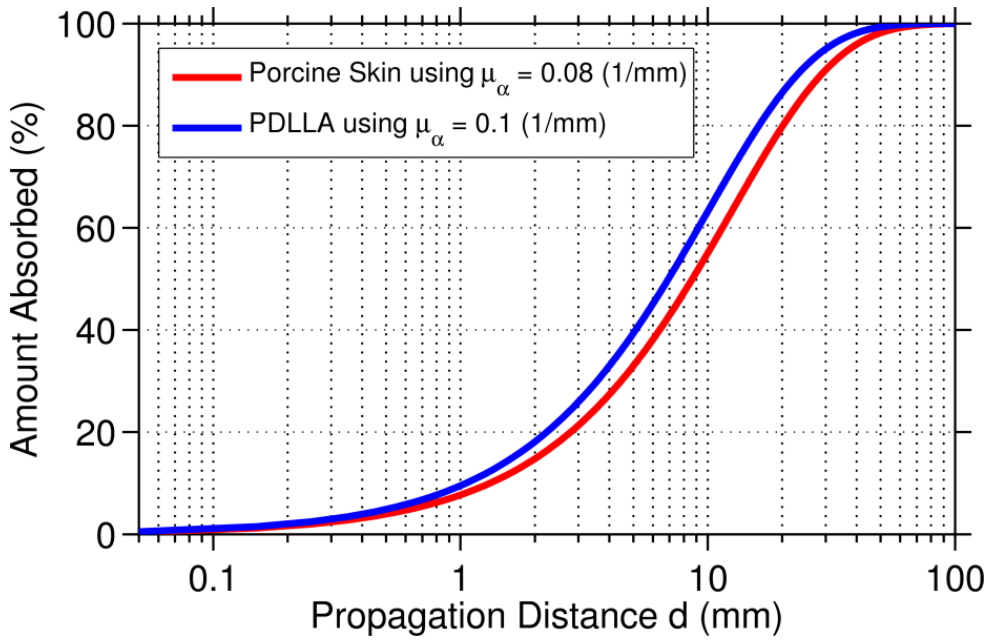


Figure 5.8: Maximum imaging depth calculation based on absorption coefficient values. Approximately 95% of light is absorbed after traveling through 3 cm of scaffold / porcine skin.

experiment was set up using the parallel plate bioreactor described in Section 3.2.2, but without providing the appropriate temperature (37°C). This gave us a short time window of ˜ 60 minutes for imaging before the cells became apoptotic (cell death).

### 5.6.1 Cell Culture

A human microvascular endothelium cell line (hTIME, American Type Culture Collection Manassas, VA) labeled with eGFP was used. All cells were cultured in EGM-2. The scaffold-MIC composite was sterilized using 70% ethanol for 30 min, followed by three sterile PBS washes for 10 min each. The ECs were then suspended in 100 μL of media and dropped onto the scaffold at a density of 1 × 10ˆ4 cells/cmˆ2. The scaffold was then placed in the incubator for 2 hours to allow cell attachment and then was gently washed with PBS to remove any unattached cells.

### 5.6.2 Results

To begin the experiment, the scaffold was housed in a parallel plate bioreactor and set onto the stage, where the fiber mirror was inserted into the MIC. Next, two control images of the cell distribution on the luminal surface at separate locations on the T axis were taken. Fig. 5.9A.1 and 5.9A.2 show direct-line-of-sight control images of the ECs on the scaffold lumen. The same ROI for both locations were then used for scanning fiber image mapping. Following the process described in Section 3.4, we obtained the reconstructed images shown in Fig. 5.9B.1 and 5.9B.2. Comparing the reconstructed images to the control images, it is clear that the spatial distribution of ECs obtained through mapping is in good agreement with the control images. This result confirms that the scanning fiber method can image through a 0.5 mm thick tissue scaffold and reveal the spatial distribution of ECs at single cell resolutions. Fig. 5.9C shows that the SNR of a single GFP-labeled EC is around 2 for the 0.5 mm thick PDLLA phantom, which also confirms the reliability of our fluorescence mapping results (the SNR measurements were done according to Section 5.3.5).

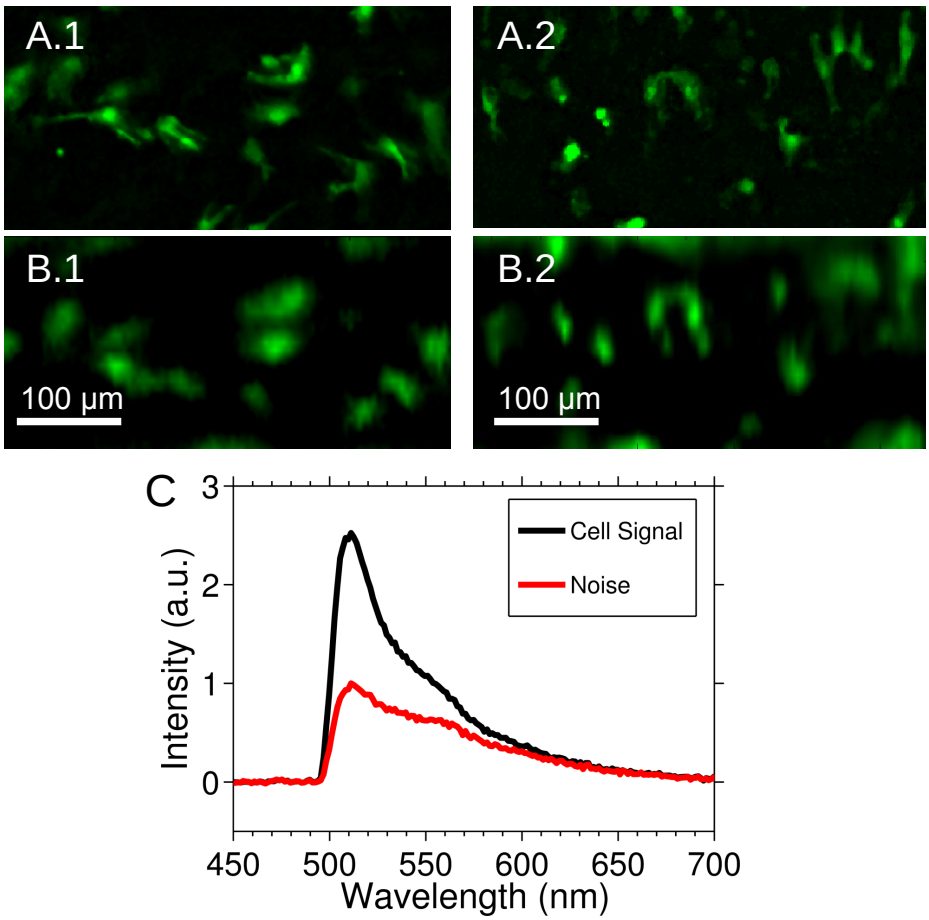


Figure 5.9: Comparison between control images and reconstructed images. Two separate sections using the same MIC were scanned with the fiber mirror. (A.1) Control image showing the actual EC distribution on the scaffold lumen in section 1. (A.2) The fluorescence mapped image of EC distribution in section 1. (B.1) Control image for section 2. (B.2) Fluorescence mapped image for section 2. When comparing the fluorescence mapped images with the corresponding control images, we see that our scanning method can "see" through a 0.5 mm thick PDLLA scaffold at cell level resolutions. (C) A SNR measurement for a single GFP-labeled EC on the luminal surface. The SNR is around 2 for a 0.5 mm thick scaffold.

## 5.7 Discussion

The study presented in this chapter provided valuable new information on the ability of our imaging method. First, we note that the scanning fiber method is well suited for tissue engineering applications. For example, the process of scaffold fabrication – a necessary step in tissue engineering – can be easily modified for embedding MICs anywhere within the tissue scaffold. Therefore, once a ROI is selected (e.g., luminal surface in the case of vessels), we can place the MIC in close proximity to the ROI to achieve cell level resolutions. This was demonstrated by reducing the distance between the MIC and the luminal surface from 500 μm (Chapter 4) to 250 μm (Chapter 5). Consequently, the pump spot on the luminal surface decreased from 250 μm to 25 μm and resulted in a resolution increase of one order of magnitude.

Next, we investigated the tissue imaging depth's impact on imaging resolution when using our method and compared it to other state of the art methods. Due to the significant photon scattering of most biological tissues, a major challenge for current deep tissue imaging technologies is the conflict between imaging depth and imaging resolution. For example, sophisticated techniques such as confocal or multiphoton microscopy can reach beyond conventional microscopy to achieve high resolution imaging within the depth of one photon TMFP [5]. Even in the case of photoacoustic imaging, the resolution remains closely linked with imaging depth, where one can realize a spatial resolution of $>$50 μm within a depth of 3 photon TMFP [8, 9]. In contrast with other imaging modalities, the method developed here can largely "decouple" the link between imaging depth and imaging resolution. The resolution of our imaging method is essentially determined by the distance between the MIC and the ROI and not by the entire thickness of the scaffold / tissue as demonstrated in Fig. 5.4. In principle, if system noise is sufficiently small compared with the signal strength generated by the fluorophore, we can maintain cell-level imaging resolution at a depth that exceeds the photon TFMP by at least one order of magnitude. In fact, using fluorescent microspheres as sources, we have shown that our imaging method is capable of achieving 20 - 30 μm imaging resolution at an imaging depth exceeding 10 photon TMFPs (0.5 mm thick PDLLA scaffold plus 3 mm thick porcine skin).

The proper functioning of the imaging method presented here requires that the system signal should be stronger than the noise. This requirement makes intuitive sense: If the fluorescence response of the detector does not change regardless of whether the excitation spot coincides with the fluorophore or not, then it would be very difficult to apply the fluorescence mapping procedure to

reconstruct the fluorophore distribution. Given this observation, it is worthwhile to consider several potential sources for system noise. First, we note that the spatial distribution of an excitation spot extends beyond its FWHM. Thus, during noise measurements, even though we moved the excitation spot away from any of the microspheres on the luminal surface, a small portion of the excitation light might overlap with microspheres and contribute towards the noise spectra in Fig. 5.6. However, noise generated by this effect should not depend significantly on the total thickness of the phantom and therefore cannot explain the reduction in system SNR after adding the porcine skin. Next, we note that during the fiber scanning process, the excitation light was directed towards the luminal surface which generates scaffold autofluorescence along the propagation path. However, the autofluorescence generated by such forward propagating excitation light would only depend on the distance between the MIC and the ROI on the luminal surface, which again is independent of the total phantom thickness. Therefore, to account for the SNR reduction observed between Fig. 5.6A and 5.6B, we have to consider the fact that a small portion of the excitation light back-reflects from the luminal surface and propagates towards the exterior surface as illustrated in Fig. 5.10. After adding the 3 mm thick porcine skin, such back propagating excitation light would induce additional autofluorescence from the porcine skin, which would reduce the overall system SNR. In fact, many effects may induce such back-propagating light. Several examples are the Fresnel reflection at the air / MIC interface, photon scattering at the interface of the MIC and the PDLLA scaffold, and light back-scattering within the turbid PDLLA scaffold, i.e., similar to what occurs in optical coherence tomography. As discussed in Section 5.3.4, the resolution of our imaging system is closely linked to the FWHM of the excitation spot on the luminal surface. The size of the pump spot is in turn determined by the scaffold optical properties as well as the distance between the MIC and the luminal surface, both of which are largely independent of the total phantom thickness. Therefore, as long as the FWHM of the excitation light remains the same and the system SNR is sufficiently large (˜2 or higher), the resolution of the fluorescence mapped images should not depend critically on the overall thickness of the optical phantom, as can be seen from Fig. 5.4.

A significant advantage of our imaging system is that we do not require a high numerical aperture objective lens to capture the signal responses, since fluorescence mapping only requires total fluorescence intensity. As a result, the imaging system can provide more than 10 cm in working distance, which is more than sufficient for the geometrical constraints imposed by most bioreactors

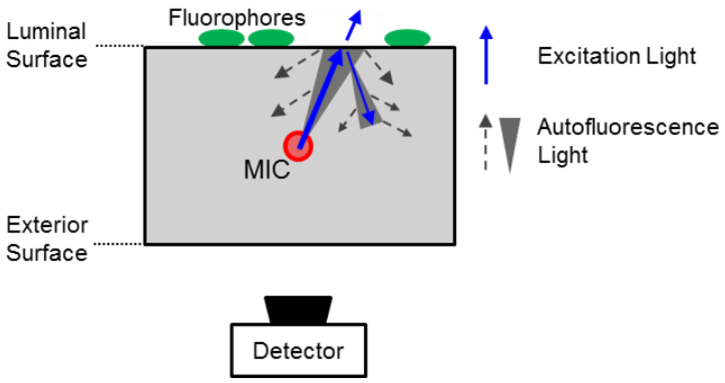


Figure 5.10: A schematic showing the potential sources for imaging system noise.

currently in use. We point out that this practical constraint is actually very stringent in tissue engineering practices. For example, most of the commercial two-photon microscopes require focusing excitation light within a sub-μm spot, which can only be achieved by using high numerical aperture objectives [6]. Such a high numerical aperture, however, generally leads to a much shorter working distance, which makes it cumbersome to integrate a functional bioreactor with a commercial two-photon or confocal microscope. A few recent examples of these types of work can be found in Refs. [10, 11]. We point out the systems described in both references are very complex. Such complexity is mainly due to the conflict between the large geometrical dimension of a functional bioreactor and the extremely short working distance of a confocal or a two-photon microscope.

The experimental results shown in this chapter suggest that as long as the fluorescent signal is significantly stronger than scaffold autofluorescence, the resolution of our imaging system does not depend critically on system SNR and does not degrade significantly as the imaging depth increases. For example, fluorescence mapped images in Figs. 5.4 have almost identical image resolution despite the fact that their SNRs are quite different. Our result and analysis indicate that in order to achieve maximal imaging depth, which is very important for future *in vivo* studies, we should select a fluorophore whose emission spectrum has minimal overlap with scaffold or tissue autofluorescence. Given the spectral data in Fig. 5.6, it is clear that using a biomarker such as near-infrared quantum dots (QDs) with emission peak above 650 nm would be ideal. Such quantum dots can be excited by the blue laser (473 nm) used in this work. Due to the very weak autofluorescence noise at the excitation wavelength of 473 nm, we should be able to further improve imaging depth to be greater than 3 mm while maintaining 20-30 μm image resolution. The fluorophores we used in this study unfortunately have significant spectral overlap with scaffold autofluorescence.

Consequently, it is very difficult to precisely determine how much of the system noise is generated by the fluorophores and how much is caused by scaffold autofluorescence. Using the QD-labeled ECs may also enable us to more accurately quantify the behaviors of system SNRs under different tissue / scaffold thicknesses.

# Chapter 6

# Dynamic Imaging

## 6.1 Overview

The static imaging experiments have shown that we can image at the depths required for imaging ECs *through* the vessel wall. These tests were performed using microspheres and cells at single time points. In this chapter, we discuss moving from static imaging to our first results involving multiple time points on the same sample. By extracting a mapped image of the luminal surface at a defined interval over the course of several hours, we combined the images into time-lapse data that shows specific cellular activity including proliferation and migration. Further, we show that dynamic information can be assessed such as cytokinesis (cell splitting) and the relative migration and movement of cells. To increase our imaging resolution, we fabricated a new scaffold-MIC composite with the MIC closer to the luminal surface by 50 $\mu$m.

In order to image the same sample over multiple time points, we required to provide the necessary components for cellular growth. Besides providing a sterile growth environment with the appropriate culturing media, the right temperature was needed as well. We solved this by supplying heat through the imaging system's stage.

The quantify the reconstruction accuracy of the scanning fiber method, we compared the mapped images with direct-line-of-sight control images using statistical analysis. To further solidify that our method is superior to state of the art tissue imaging techniques in terms of imaging depth, we compared our results to confocal microscopy. The tests in this chapter provide further proof

that our method can be applied to *in vitro* experiments and allow us to finally move to full vessel imaging, which is presented in the next chapter.

## 6.2 Pump Spot Characterization

A new planar scaffold was fabricated using the method in Section 3.1.4. The scaffold thickness was 500 μm and a MIC was embedded 200 μm from the luminal surface as illustrated in Fig. 6.1A. Compared to the scaffold in Chapter 5, the MIC was now embedded 50 μm closer to the luminal surface, with the expectation that this further increased the reconstruction resolution. Prior to the experiment, the scaffold was soaked in EGM-2 and then placed onto a microscope slide on top of the imaging platform. After inserting the fiber mirror, the filters on the control image camera were removed and images of the luminal surface were captured while varying the fiber launching angle $\vartheta$ from -45° to 45° in five-degree increments. This was repeated at five random locations on the scaffold. The FWHM was then extracted from each successive image and plotted as a function of launching angle $\vartheta$ (Fig. 6.1). As before, the angle $\vartheta$ = 0° denotes the case where the excitation light was launched directly towards the luminal surface and produced a FWHM of 16.5 ± 0.5 μm. At ± 45°, the FWHM roughly doubled to 31.6 ± 3.7 μm. Since the spatial profile of the pump spot directly determines the resolution of the imaging method, the imaging system can achieve an effective resolution in the order of 16.5 to 31.6 μm. The plot in Fig. 6.1 indicates that the resolution of the imaging system was highest at 0° and decreased with fiber mirror rotation.

## 6.3 Temperature Control

To enable cell imaging over an extended time period, we required to provide the ideal growth temperature for ECs to the luminal surface – the internal body temperature of 37°C. This was accomplished by adding a flat heating element (Ningbo Proway Optics & Electronics, China) to the imaging system's sample stage. The heated stage then kept the media inside the bioreactor warm as illustrated in Fig. 6.2. However, due to the heat exchange between the bioreactor and the 25°C ambient air temperature, the heated stage had to be set to 44°C. This setting was calibrated and monitored using a thin film temperature probe (TFP, Omega.com) that was placed on an unused section of the luminal section. On average, the temperature at the luminal surface was 37°C ±1°C,

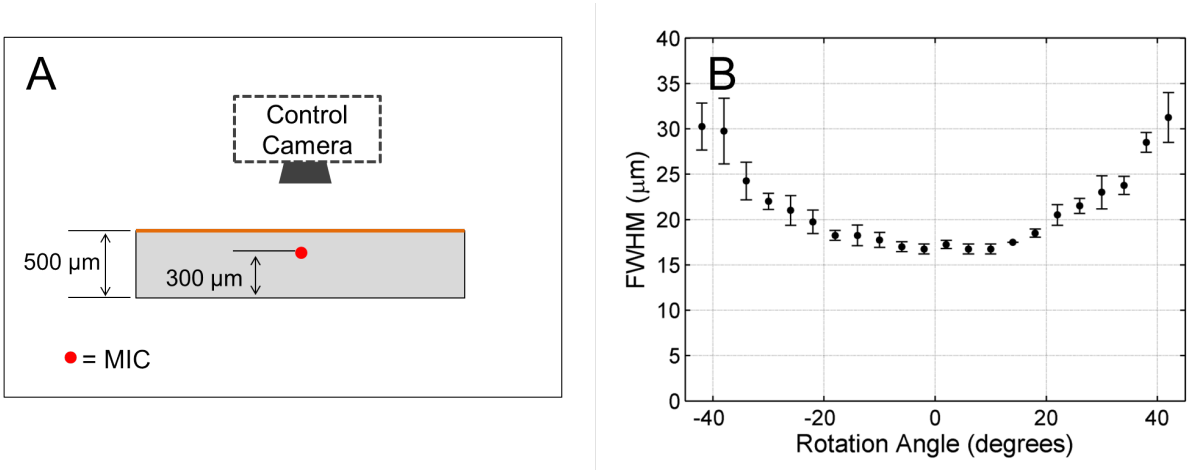


Figure 6.1: (A) The scaffold configuration used for the dynamic imaging experiments is shown. (B) The pump spot was characterized by sweeping the fiber launching angle while recording with the control camera. The reconstruction resolution of this scaffold-MIC composite is measured by the FWHM of the excitation spot on the luminal surface for fiber mirror launching angles $\vartheta$ = - 45° to + 45° (mean ± std. dev. of n = 5 trials). This plot indicates that the resolution of the system is best when the excitation light is launched directly towards the luminal surface ($\vartheta$ = 0) and deteriorates by ˜1/2 when the fiber micro-mirror is rotated to $\vartheta$ = ± 45°.

which is sufficient for long term cell culturing. Note: We did not exchange the media during experimentation; therefore, the limiting factor for long term imaging was no longer temperature, but the lack of media replenishment and proper gas supply (i.e. CO2 and O2).

## 6.4 Dynamic Image Mapping of Endothelial Cells

### 6.4.1 Procedure

For the dynamic imaging study, a total of 3 scaffold-MIC planar scaffolds were fabricated with an average thickness of 513 ± 21 µm. These scaffolds were used to conduct the imaging study with the configuration illustrated in Fig. 6.3A. The top surface of the scaffold represents the luminal surface of a blood vessel. As discussed in the previous chapters, the planar configuration allowed a direct-line-of-sight access to the luminal surface for the control camera to take images for quantitative image comparison and validation. For this experiment, we used a human microvascular endothelial cell line (hTIME). Before cell seeding, the scaffolds were sterilized using 70% ethanol for 30 min,

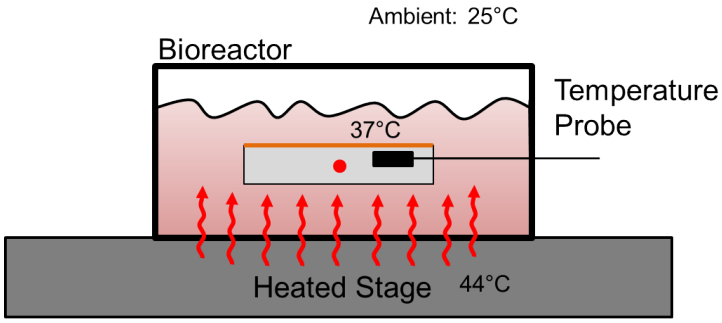


Figure 6.2: The parallel plate bioreactor was heated by a temperature regulated stage. The stage temperature was set to 44°C, so that after the heat exchange between the bioreactor and the ambient air, the temperature at the luminal surface was 37°C ±1°C. With the ideal temperature for cell growth at the luminal surface, we were able to perform dynamic imaging over a 24 hour time frame.

followed by three sterile phosphate buffered saline (PBS) washes for 10 min each. A 300 μL aliquot of media containing 100 μg / ml fibronectin (Sigma Aldrich, St. Louis, MO) was then added to the scaffold for 30 minutes to enhance cell adhesion. ECs were trypsinized and cell viability was determined using trypan blue stain (Vi-cell, Beckman Coulter, Brea, CA). Cells were then re-suspended in 100 μl of media and seeded onto the luminal surface of the scaffold at a density of 1 x 10^4 viable cells/cm^2. The scaffolds were placed in the incubator for 2 hours to allow cell attachment and then were washed gently with PBS to remove any unattached cells. The scaffolds were then placed in the parallel plate bioreactor with cell culture media for imaging experiments.

### 6.4.2 Results

After placing the bioreactor on the heated imaging platform, a 300 μm x 300 μm region of interest (ROI) on the luminal surface was selected using the control camera. Fig. 6.3B shows an image taken with the control camera with the ROI indicated in the red box. Afterwards, fiber scanning and fluorescence mapping was performed to image the GFP-labeled ECs. Fluorescence mapping was repeated every 30 minutes. After each scan, we took a control image of the same ROI to quantify the accuracy of our method. A selection of mapped images and the corresponding control images of Scaffold 1 are plotted in a false-color black-green in Fig. 6.3C, where the brightness of the green color represents the intensity of GFP fluorescence. When comparing the mapped images with the control images, we observe that the spatial distributions of the ECs are in good agreement

between the corresponding image sets. Furthermore, from the mapped images, it is evident that individual cells could be resolved through the ~500 μm thick scaffolds. In Fig. 6.4, we show a mapped image / control image pair for each of the three scaffolds.

### 6.4.3 Statistical Analysis

To quantify the accuracy and reliability of the dynamic imaging results, both the mean absolute error (MAE) and the root mean squared error (RMSE) were calculated between 25 pairs of mapped images and their corresponding control image for all three scaffold samples. Both the MAE and RMSE estimation method are widely accepted for comparing two sets of data obtained by intrinsically different methods [12]. The MAE is defined as:

$$MAE_i = \frac{1}{N}\sum_{n=1}^{N} |P_{i,n} - C_{i,n}| \tag{6.1}$$

The RMSE is defined as,

$$RMSE_i = \sqrt{\frac{1}{N}\sum_{n=1}^{N} (P_{i,n} - C_{i,n})^2} \tag{6.2}$$

In these equations, $i$ is the trial number that ranges from 1 to 25, $n$ is a specific pixel in each image, $C_{i,n}$ are the control images, $P_{i,n}$ are the fluorescence-mapped images and $N$ is the total number of pixels in the control as well as mapped images. Prior to error estimation, each $C_{i,n}$ / $P_{i,n}$ image pair was normalized to values between 0 and 100 such that MAE and RMSE represented percent error. It is critical that the mapped image and the control image pairs overlap precisely to allow accurate error estimation. Therefore, a custom MATLAB image registration script was written to calculate the best spatial fit between $C_i$ and $P_i$ prior to error estimation [13].

The MAE and RMSE results for each scaffold were plotted as histograms in Fig. 6.5, showing overall error deviation for both image comparison methods. The mean ± std. dev. of the MAE and RMSE between the three scaffolds was found to be 5.83% ± 0.88% and 10.26% ± 1.14%, respectively.

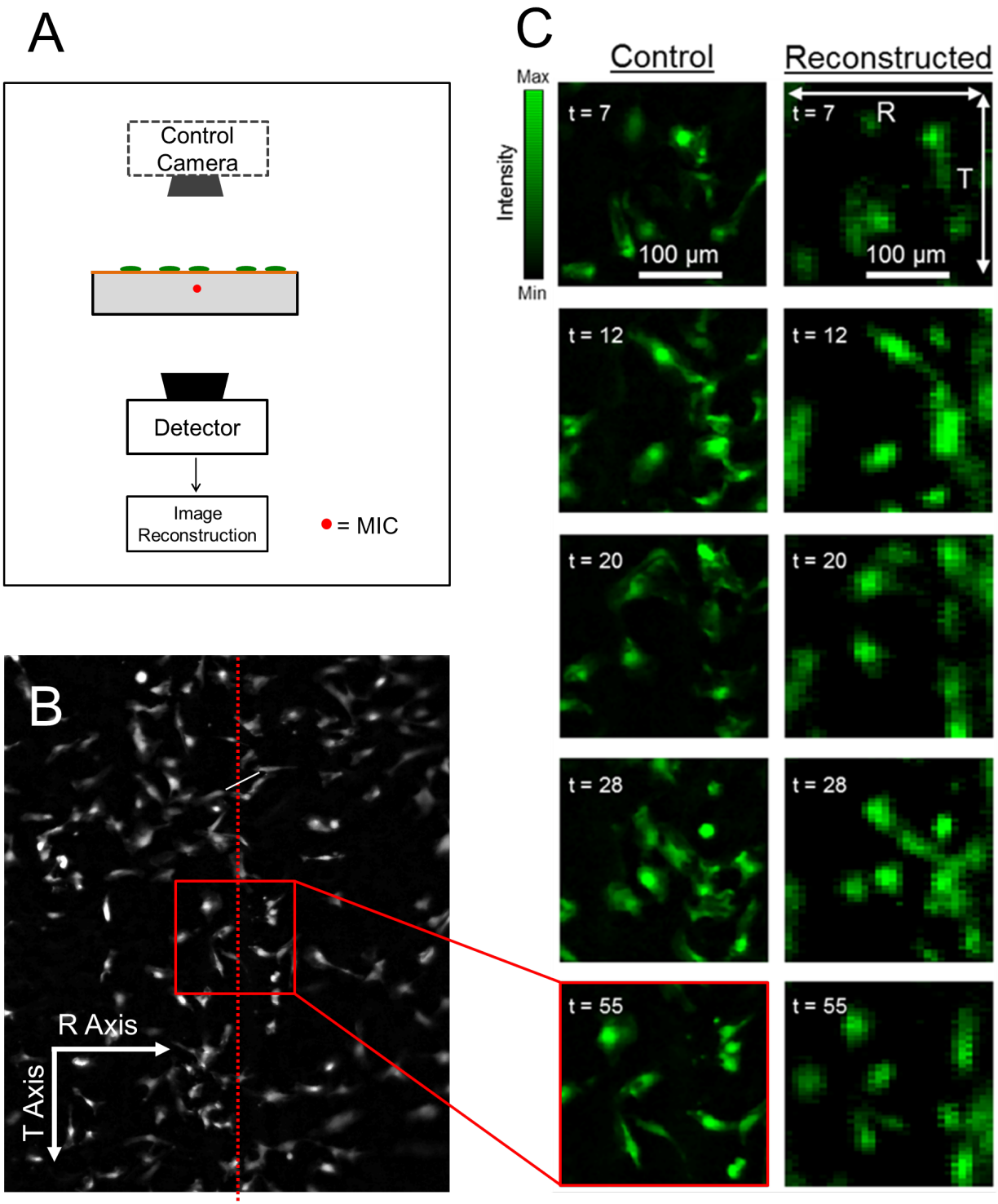


Figure 6.3: Imaging system configuration to perform the dynamic imaging experiments. After completing the scanning for a mapped image, an image with the control camera was taken for validation. (B) An example control image, showing the selected ROI. (C) A selection of mapped image / control image pairs for Scaffold 1 showing the accuracy of the reconstruction method. The t-value indicates the trial number. Trials were repeated every 30 minutes.

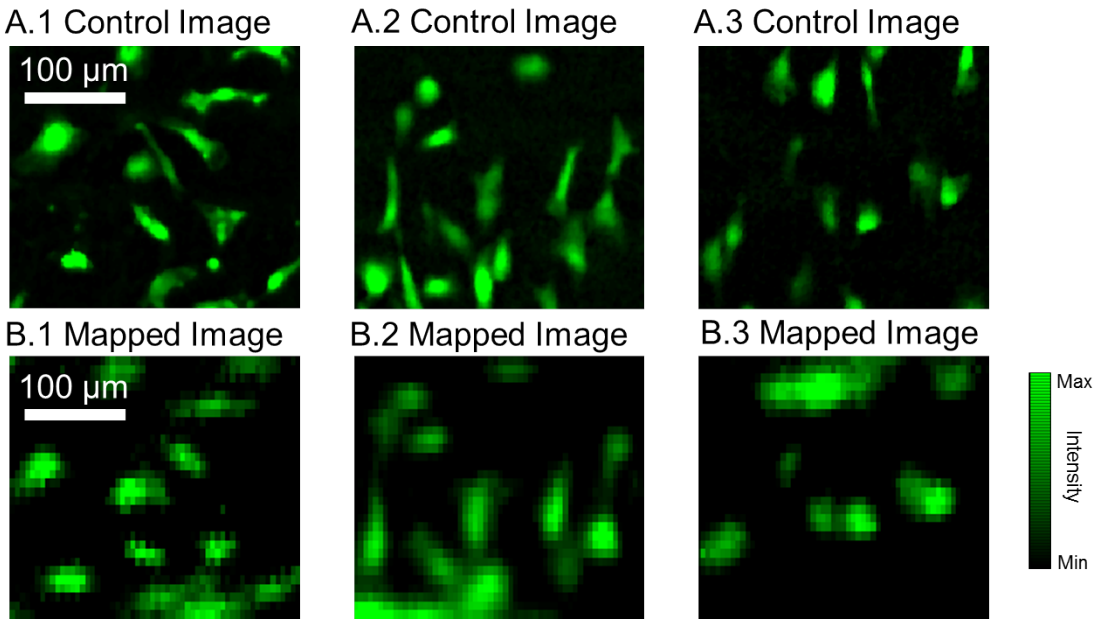


Figure 6.4: Fluorescence mapping results and comparison: (A.1-3) Control images obtained through direct line-of-sight (control) image acquisition. (B.1-3) An ROI measuring 300 x 300 µm above the MIC was selected on each scaffold and fluorescence-mapped image was obtained using the fiber-scanning algorithm. The fluorescence signals were captured on the exterior surface of the scaffold to demonstrate the capability of mapping cells through ˜500 µm thick PDLLA scaffolds. A total of 75 image pairs (25 pairs per scaffold) were obtained and evaluated for this experiment.

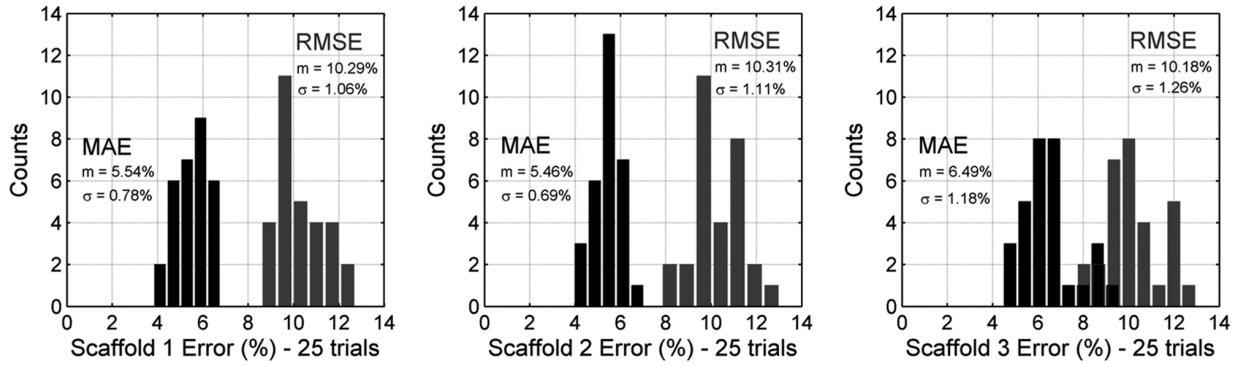


Figure 6.5: Statistical validation of the fluorescence-mapping method: Mean absolute error (MAE) and root mean squared error (RMSE) histograms for comparison between pairs of fluorescence-mapped and control images for each scaffold. The mean ± std. dev. of the MAE and RMSE between the three scaffolds was 5.83% ± 0.88% and 10.26% ± 1.14%, respectively.

### 6.4.4 Comparison with Confocal Laser Scanning Microscopy

The image reconstruction penetration depth through the scaffold was compared to that of confocal laser scanning microscopy (CLSM), which is widely used in tissue engineering to image through biologically thick tissues and scaffolds [5]. We used the experimental configuration shown in Fig. 6.6A,B to quantify the quality of the optical image when we attempt to image "through" the scaffold.

Three PDLLA scaffolds of varying thicknesses (100, 230, 460 μm) were fabricated using the electrospinning and sintering technique described in Section 3.1. GFP-labeled ECs were seeded onto one side (luminal surface) of the scaffolds at a density of 1 x 10^4 viable cells/cm^2, incubated for 2 hours to allow cell attachment, and then placed into a culture dish with a 170 μm glass coverslip bottom upon which the scaffold rested. The CLSM (Zeiss LSM510 META, Carl Zeiss Inc., Germany) equipped with a 10x Plan-Apochromat 0.45 NA objective (Carl Zeiss Inc., Germany) was then used to obtain a direct-line-of-sight image of cells on each scaffold and, subsequently, used in the attempt at "looking" through each scaffold to resolve the cells on the luminal surface.

First, the CLSM was used to obtain a direct-line-of-sight image of cells on each scaffold sample (Fig. 6.6A). Next, the scaffolds were reversed and the CLSM was used in the attempt to image the cells by "looking" through the scaffold (Fig. 6.6B). To obtain the sharpest possible image of cells on the luminal surface when imaging through the scaffold, a z-stack was performed at 5-micron increments until the luminal surface reached the imaging focal plane. This measurement is analogous to placing the confocal microscope outside of a blood vessel (i.e. exterior surface) and trying to image through the scaffold to capture EC distributions on the luminal surface.

GFP-ECs can easily be imaged if placed in direct-line-of-sight to the CLSM objective (Fig. 6.6C); however, the resolution of confocal images is greatly diminished when "seen" through the 100 μm thick PDLLA scaffold (Fig. 6.6D). Furthermore, confocal microscopy failed to visualize individual cells through the thicker 230 μm and 460 μm PDLLA scaffolds (Fig. 6.6E and 6.6F, respectively). In contrast, our imaging method was able to detect and accurately identify individual EC distributions through the ~500 μm thick PDLLA scaffold (Fig. 6.6H). The corresponding direct-line-of-sight image in Fig. 6.6G confirmed the accuracy of the fluorescence-mapped image in Fig. 6.6H.

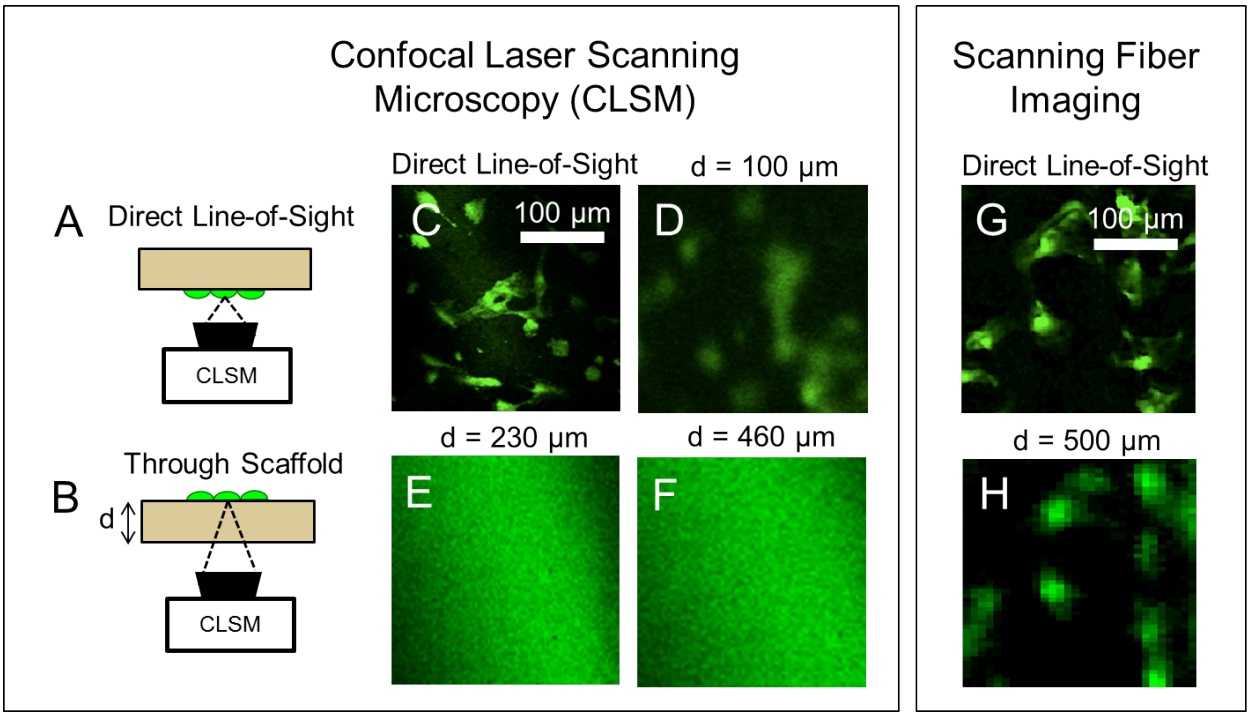


Figure 6.6: Imaging depth comparison to CLSM: (A) Diagram of direct-line-of-sight CLSM-image to visualize "actual" GFP EC distribution. (B) The sample is then reversed to image the luminal surface through the electrospun PDLLA scaffold with the CLSM. Three scaffolds with thickness d = 100, 230, and 460 µm were used. (C) Direct-line-of-sight CLSM-image of GFP ECs on the luminal surface. (D) ECs on the luminal surface when imaged through the thickness of a 100 µm-thick scaffold. Individual ECs could not be identified when imaging through (E) 230 µm and (F) 460 µm thick scaffolds. The imaging method could, however, detect ECs on the luminal surface through a ~500 µm thick scaffold (H). Comparison with a direct-line-of-sight image (G) confirms the accuracy of the fluorescence-mapped image.

### 6.4.5 Signal Versus Noise

To investigate the SNR of cell fluorescence versus the background noise produced by scaffold autofluorescence, the spectral response of the cells and the scaffold were measured from 450 nm - 750 nm using a spectrometer (S2000, Ocean Optics, Dunedin, FL). To quantify the background autofluorescence noise, the excitation spot was aimed towards a location on the scaffold that was void of cells. Conversely, the excitation spot was aimed directly at a cell to collect GFP fluorescence from the cells. The response signal was then collected through the scaffold by the detector and the excitation light was filtered out with a long pass filter with a cutoff at 490 nm (BLP01-488R, Semrock). By using a long pass filter, the spectral band with the largest SNR could be determined.

First, the optical spectrum of the fluorescent signals generated by the ECs and the autofluorescence (noise) produced by the scaffold was measured (Fig. 6.7A). To ensure that the measured fluorescence can correctly be attributed to either GFP-labeled ECs or scaffold autofluorescence, the control camera was used to identify the fluorescent source on the luminal surface. Fig. 6.7B shows the exterior surface image captured by the EM-CCD camera when: (1) an EC was illuminated by the excitation spot on the luminal surface and (2) the excitation spot did not encounter a GFP-labeled cell. The two images are clearly distinct in both spatial distribution as well as fluorescence intensity, which further corroborates the difference in spectral responses identified in Fig. 6.7A.

### 6.4.6 Dynamic Assessment of Cell Activity

To illustrate the dynamic capability of the our imaging method, the same ROI was scanned on the cell-seeded scaffold at an interval of 30 minutes over 24 hours producing a collection of 'time lapse' mapped images. By comparing successive images, we were able to track the relative cell movement in the ROI. Figure 6.8 shows four mapped images 30 minutes apart. These results demonstrate the ability to continuously and non-destructively track single cells in their scaffold microenvironment. Observing a different ROI (Fig. 6.8E-G) at a 30 minute interval, we were able to detect a single, localized fluorescent feature (red arrow) progressively separating into two spatially distinct fluorescent "spots" (double-headed red arrow). This behavior strongly suggests that the cell indicated by the red arrow had undergone cytokinesis.

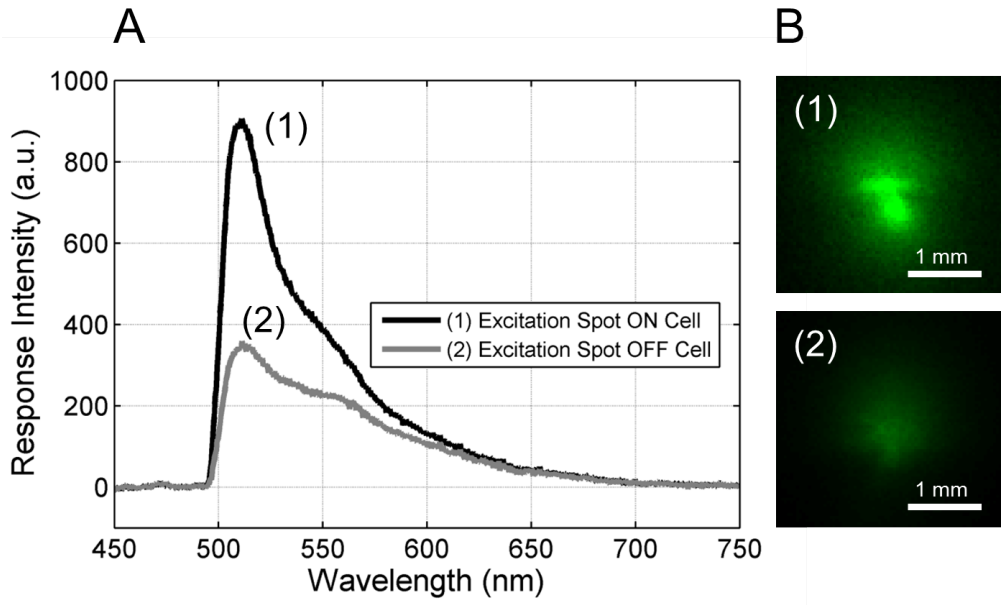


Figure 6.7: Signal-to-noise ratio characterization: (A) Comparison of the spectral emission response signal of the ECs and background noise caused by scaffold autofluorescence from 450-750 nm. Comparison of the cell response to the background noise gives the signal-to-noise ratio (SNR). (B) Representative EM-CCD camera images taken from the exterior surface when (1) the excitation spot was on a cell or (2) placed on an area void of cells (scaffold autofluorescence).

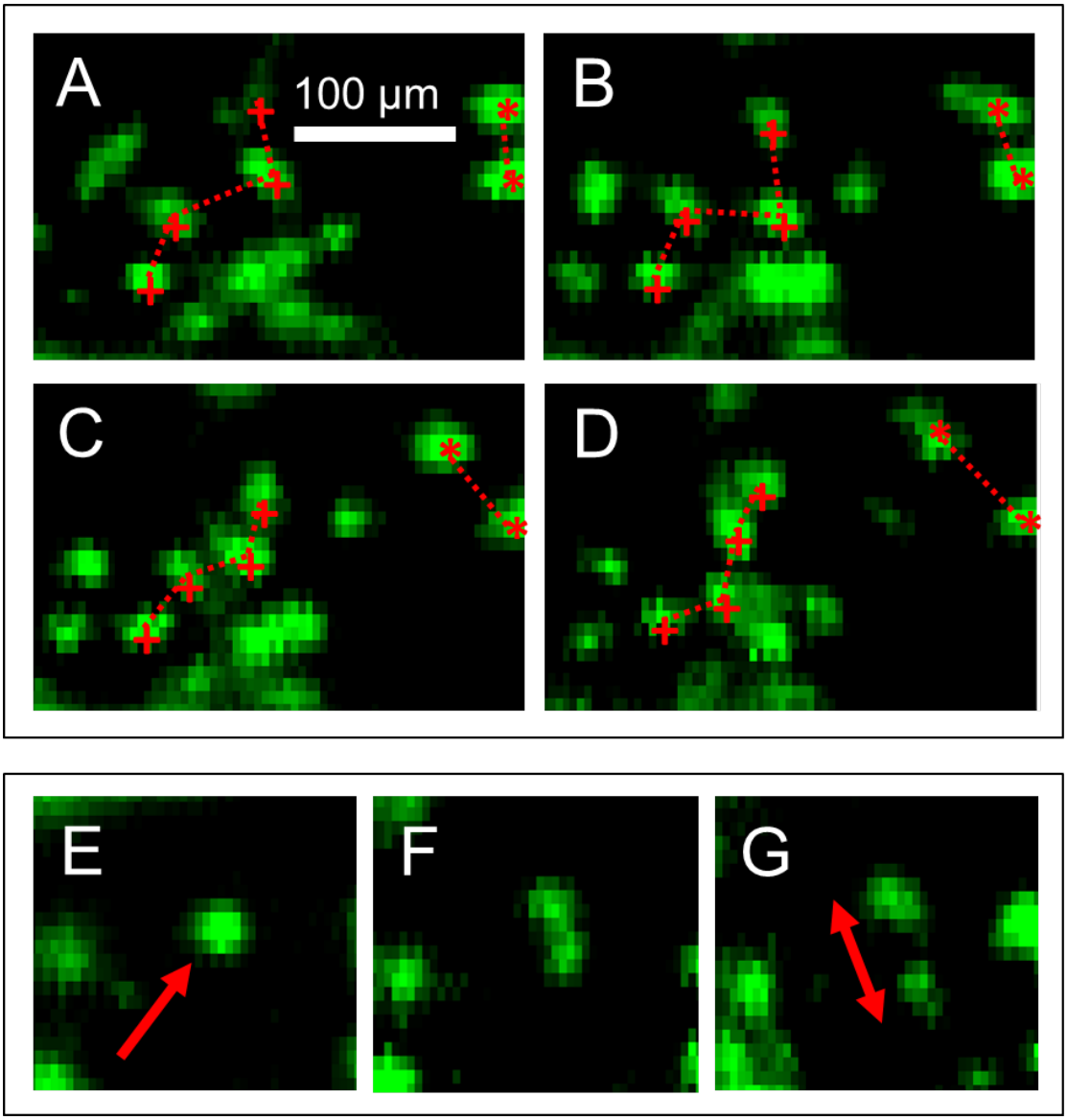


Figure 6.8: Dynamic imaging: (A) to (D): Four fluorescence-mapped images were taken in the same ROI at a 30 minute interval to demonstrate the dynamic imaging capability. The red lines serve as a visual aid to track the relative movement of cells between successive images. Images in (E) to (G), which are taken at a 30 minute time interval in another ROI, suggest that we can use our imaging method to monitor cell cytokinesis.

## 6.5 Discussion

With the "unwrapped" configuration in Fig. 6.1A, the planar scaffold enabled us to directly compare to standard fluorescence microscopy. In order to validate the imaging method, we performed a statistical comparison between the mapped images and control images using the ˜500 μm thick PDLLA scaffolds. In particular, the MAE and RMSE were calculated using 75 pairs of fluorescence-mapped images and their corresponding control images (25 pairs per scaffold). The MAE indicates that the mapped images are within 6% error compared to the control images and the RMSE shows that deviations are roughly around 10%. It should be noted that the RMSE comparison method is more sensitive to statistical outliers than the MAE and thus the preferred indicator of mapping accuracy [23]. Overall, both methods show that the error is consistent between scaffold groups and that the standard error within scaffold groups is small, thereby validating that the mapped images are a reliable estimation of the actual cell distribution.

Characterization of the excitation spot on the scaffold surface allowed estimation of the spatial resolution of the FOB imaging method. Once excitation light was delivered into the scaffold through the MIC, it experienced optical scattering as it traveled to the surface. Since the MIC-to-surface distance varied with respect to launching angle, the FWHM of the excitation spot at the scaffold surface varied accordingly. As a result, the system resolution decreased as the launching angle increased. According to the results in Fig. 6.1B, the imaging method has a spatial resolution in the range of 20 to 30 μm. Furthermore, the results in Fig. 6.3 and Fig. 6.4 showed that the imaging system can spatially resolve single GFP-labeled ECs on the scaffold's surface, which is consistent with 20-30 μm imaging resolution. Although the increasing FWHM presents a limitation along the field of view that is perpendicular to the MIC, the range is at least 300 μm according to Fig. 6.4. If higher resolution is desired in a larger field of view, we can always incorporate more MICs within the scaffold as demonstrated in Chapter 4. Furthermore, we also note that the field of view along the MIC direction is essentially unlimited.

Similar to other imaging methods, the results of the fiber-based imaging method are only accurate if the cell fluorescence signal is stronger than the scaffold autofluorescence noise. Given the spectral response in Fig. 6.7A, the signal-to-noise ratio (SNR) of the imaging system is found by dividing the signal curve (1) by the noise curve (2), which is equal to or greater than 2 at the peak GFP emission (510 - 530 nm). As can be seen from Fig. 6.3 and Fig. 6.4, a SNR of 2 is sufficient to separate the signal from the noise to obtain cell-level resolution images. In the future, we can

further improve the SNR by ensuring the fluorescently labeled ECs have minimal spectral overlap with scaffold autofluorescence.

We emphasize that the imaging method is dynamic and nondestructive, which means we can scan the same ROI multiple times over any desired time period. In fact, in Fig. 6.8, we have demonstrated that we can continuously monitor the movement of single GFP-labeled ECs through the ˜500 μm thick scaffold. The substantial increase in imaging penetration depth and flexibility in the placement of camera and objective lens enables us to address the pressing need for nondestructive, dynamic imaging of engineered tissue constructs in geometrically constrained configurations such as the vascular scaffold. With these results in mind, we were ready to move to full vessel imaging experiments, which are presented in the next chapter.

# Chapter 7

# Imaging the Vascular Lumen

## 7.1 Overview

This chapter present the culmination of this project, where we used vascular scaffolds to perform real-time nondestructive EC imaging using the scanning fiber method. After having confirmed in the previous chapter that the resolution, accuracy, and reliability of the imaging method has reached sufficiently high level, we performed the experiments on the full vessels in two steps. At first, the parallel plate bioreactor was used as an intermediate step before testing on the pulsatile-flow bioreactor began. Experimentation on the parallel plate bioreactor was well established from the previous experiments up to this point, so moving from a planar scaffold to a tubular scaffold is a relatively small step. In essence, the difference between the planar scaffold and the tubular scaffold in terms of the geometry of the vessel wall and the embedded MIC is virtually none. Although there is always a certain degree of unpredictability, we felt confident enough from the previous results to skip the optical characterization of the vascular scaffold and went straight to imaging reconstruction. Once it was confirmed that ECs could be imaged in the vascular scaffold, we moved towards using the pulsatile-flow bioreactor for imaging.

## 7.2 Vascular Scaffold in Parallel Plate Bioreactor

### 7.2.1 Experimental Procedure

A vascular scaffold was fabricated using to the method in Section 3.1.4.2. The scaffold thickness and MIC placement was identical to the composite used in Chapter 6. Specifically, the MIC was embedded 200 μm from the luminal surface and the scaffold wall was 500 μm thick. Using this configuration, we expected 20 - 30 μm based on the results shown in Fig. 6.4. After sterilizing the scaffold in 70% ethanol for 30 min, followed by three sterile PBS washes for 10 min each, we trypsinized hTIME cells and re-suspended them in 100 ul of media. The cell suspension was then seeded at a density of 1 x 10^4 viable cells/cm^2 on the luminal surface of the vessel. To ensure that the cells are present on the ROI of the embedded MICs, we let the cells float down and attach to the bottom vessel surface. The scaffold was then placed in an incubator for 2 hours to allow cell attachment and then the vessel interior was gently washed with PBS to remove any unattached cells. The scaffold was then housed in the parallel plate bioreactor, where subsequently culturing media was added to the growth chamber. The bioreactor was then placed on the heated platform to begin imaging. Figure 7.1 shows a photograph of the parallel plate bioreactor on the heated platform with the fiber mirror inserted into a MIC.

### 7.2.2 Results

Since we do not have direct-line-of-sight access to the luminal surface due to the tubular structure of the scaffold, we must rely on alternative methods to find an area with an appropriate concentration of cells to set as our ROI for imaging. After inserting the fiber mirror into the MIC, the EM-CCD camera response was carefully monitoring the as the fiber was being moving along the MIC. If several strong signals were detected by the EM-CCD camera in close proximity of the pump spot location (which is moved “blindly”), we knew that an interesting region was found for imaging. After deciding upon the ROI, we set the automated system to perform image mapping every 3 hours for a total of 21 hours. The results of this studys are shown in Fig. 7.2. Mapped images shows single ECs resolved at high enough resolution to distinguish the individual morphologies of cells. The images are placed side-by-side in successive order with a (purple) boarder surrounding an interesting area (the border aids in visualizing the difference between images). From simple

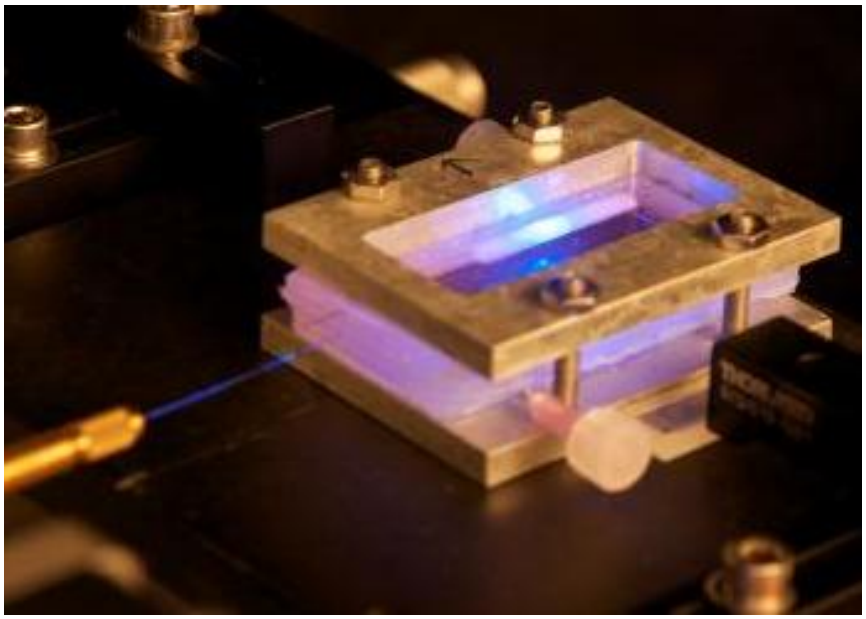

Figure 7.1: Photograph of a vascular vessel housed in a parallel plate bioreactor. The scanning fiber is inserted into the MIC and the mapping algorithm is run to produce images of ECs on the luminal surface of the vessel.

observation, we note that the cells have migrated and proliferated throughout the several-hour period. In essence, these are our first images proving that image reconstruction of ECs on the luminal surface inside a bioreactor is possible using our newly developed scanning fiber method.

## 7.3 Vascular Scaffold in Pulsatile-Flow Bioreactor

### 7.3.1 Experimental Procedure

A second vascular scaffold was fabricated with the same specifications as in Section 7.2.1 to be used inside the pulsatile-flow bioreactor. The scaffold was sterilized in 70% ethanol for 30 min, followed by three sterile PBS washes for 10 min each, and then assembled into the pulsatile bioreactor according to the procedure in Section 3.2.3.1. After applying the silicone glue to seal the notches from where the MICs extrude from the bioreactor, we trypsinized hTIME cells and re-suspended them into EBM-2 culture media. The cell suspension was poured into a syringe, which was then attached to one of the inlet. By pumping the cell suspension through the interior of the vessel

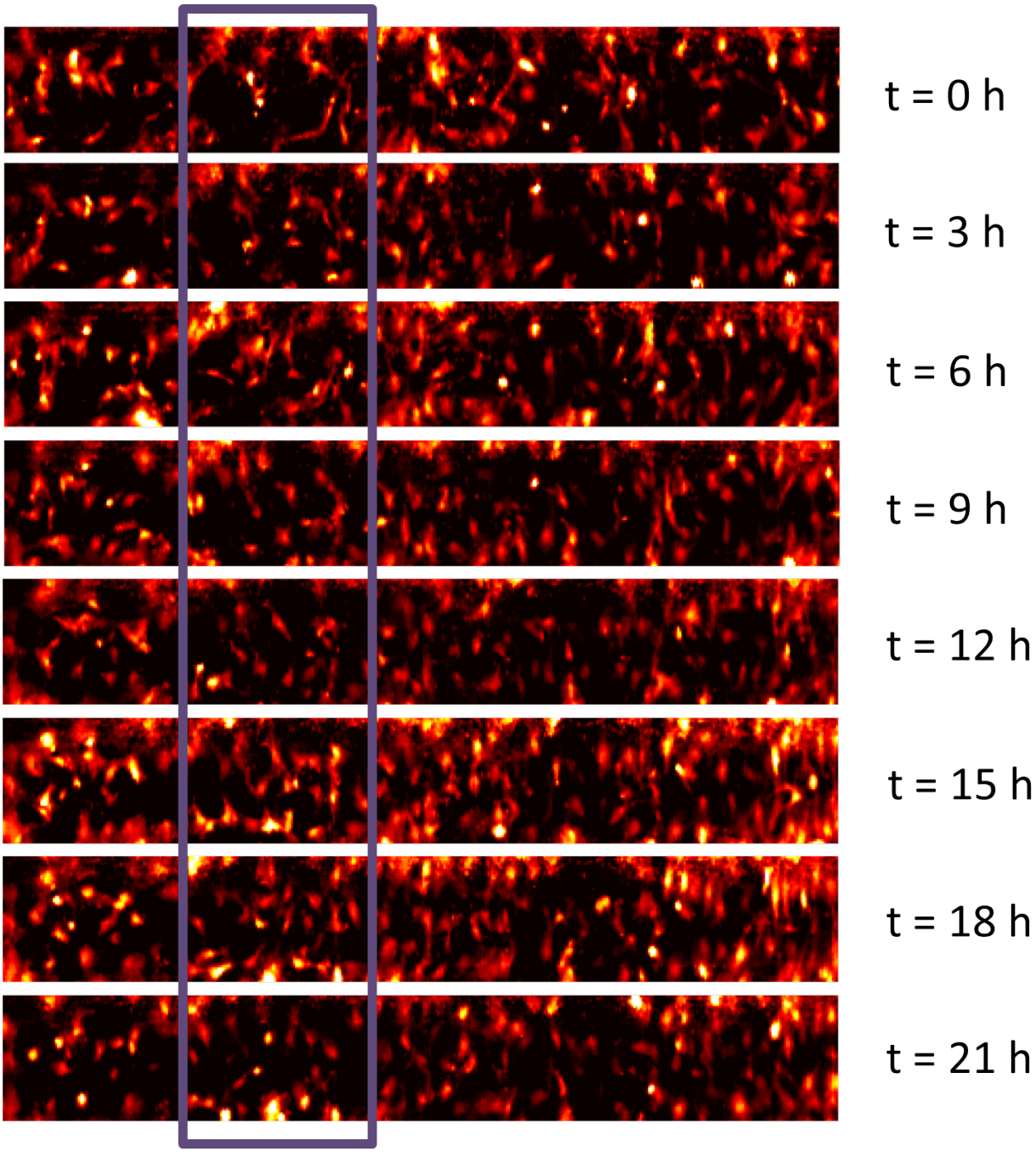


Figure 7.2:

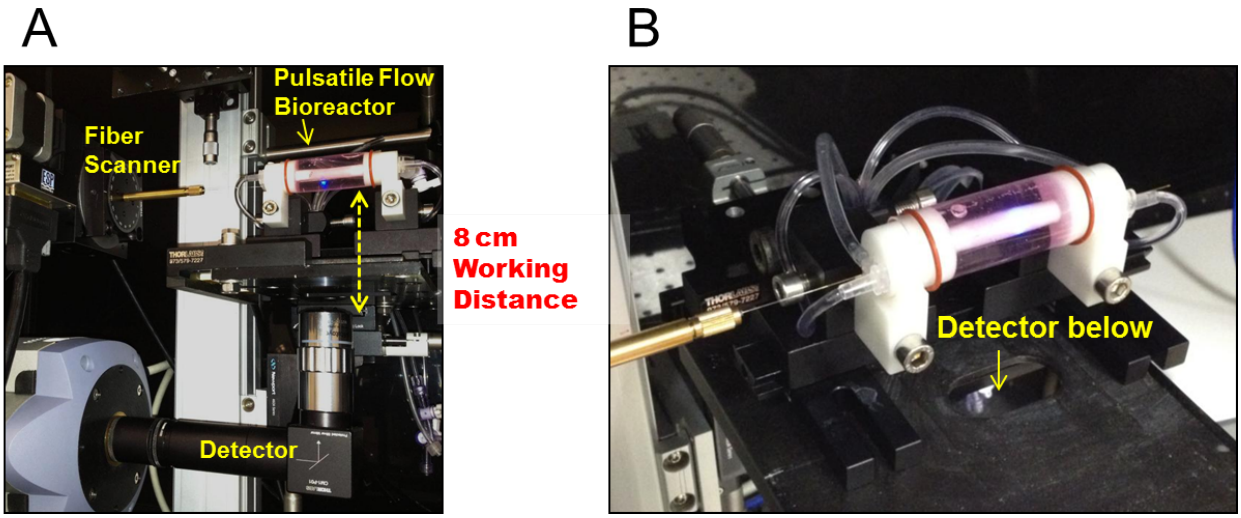


Figure 7.3: (A) Photograph of the pulsatile-flow bioreactor on the imaging platform. The fiber scanner is approximately 6 CMs away from the bioreactor and the working distance of the lens is 8 CMs. This shows that the imaging method is suited for various tissue engineering applications involving complicated bioreactors. (B) Close-up view of the pulsatile-bioreactor with a the fiber mirror inserted into the MIC. The detector is below the stage cutout.

and then clamping off both inlets, we effectively performed cell seeding post-bioreactor assembly. Next, the main bioreactor chamber was filled with EBM-2 and the bioreactor was placed into an incubator for 2 hours so that cells could attach. Performing the cell seeding after the bioreactor was assembled was favored due to the risk of contamination during assembly. Finally, sterile PBS was pumped through the interior inlets to wash out the media and unattached cells. The bioreactor was then placed onto the system platform as shown in Fig. 7.3(A,B).

### 7.3.2 Results

A similar procedure was used as with the parallel plate bioreactor to scan the luminal surface of the vascular scaffold inside the pulsatile-flow bioreactor. After focusing the lens and detector onto the exterior surface on the bottom of the vessel as show in Fig. 7.3A, we probed for a decent concentration of cells using the EM-CCD output as a guide when moving the fiber mirror inside the MIC. Once the desired ROI was chosen, we turned on the automated fiber scanning algorithm to image two time points 6 hours apart. The results are shown in Fig. 7.4. The mapped images show that we could resolve single ECs and detect a significant change over the course of 6 hours.

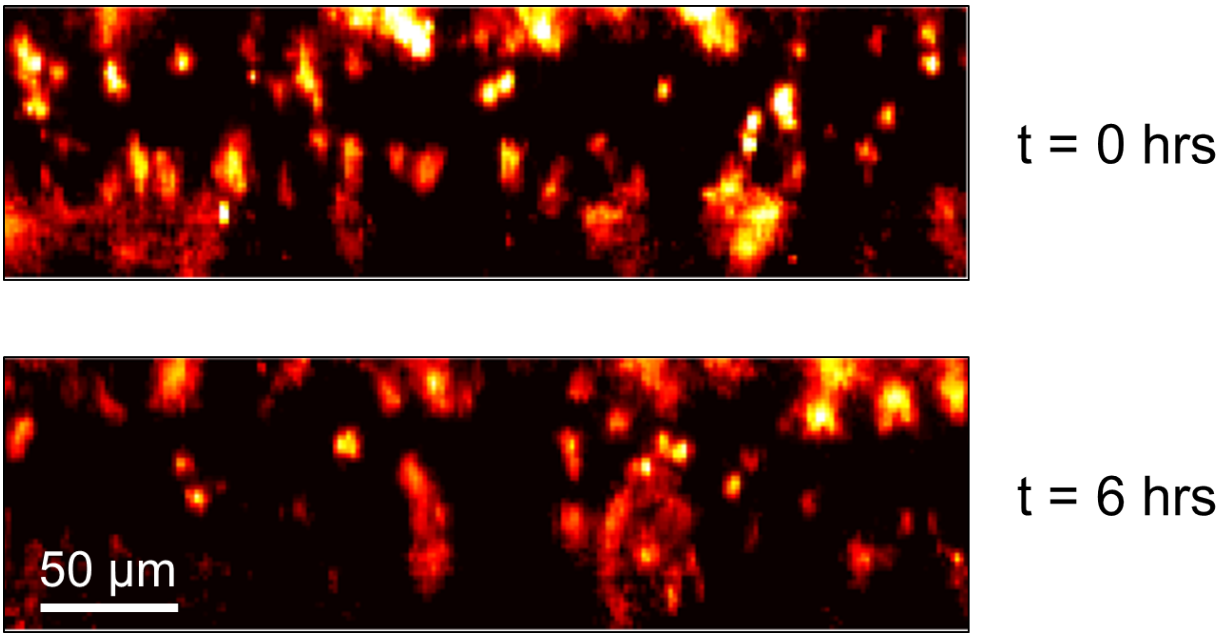


Figure 7.4: Two successive mapped images of ECs on the luminal surface 6 hours apart. The images were taken using the scanning fiber method inside a specialized pulsatile-flow bioreactor.

These results prove that we can image ECs inside a specialized pulsatile-flow bioreactor at single cell resolutions over an extended period. Further, we demostrate that the imaging depth of thick and opaque scaffold wall was overcome, while doing so with a working distance of 8 cm!

## 7.4 Conclusion

We have produced the first real-time nondestructive images of cellular activity inside a vascular scaffold and proven that our method is well suited for tissue engineering. Given the advantages offered by a significantly enhanced imaging depth and working distance, this imaging method may find numerous *in vitro* or *in vivo* applications in other tissue-engineered constructs that contain epithelial tissues.

# Chapter 8

# Discussion & Future Work

**The need for nondestructive imaging in tissue engineering:** For tissue engineers, it is critical to assess the neo-tissue's maturation progress in response to external stimuli such as mechanical stimulation, specific growth factors, and overall culturing conditions. These parameters have a major effect on tissue maturation, viability and function after in vivo implantation. Similarly, tuning scaffold properties such as porosity, topography, mechanical properties and chemistry can have a significant impact on cell attachment, viability, differentiation potential and ECM production [55]. Therefore, evaluation of cell-seeded tissue-engineered constructs in response to these conditions and scaffold properties in vitro can provide valuable information on the suitability of scaffold design and predict the overall regenerative capacity of the construct *in vivo*. Evaluating specific parameters of engineered tissue maturation is equally important for the optimization of tissue engineering techniques.

Current methodologies used to evaluate tissue development *in vitro* employ either destructive or nondestructive techniques. However, there are significant limitations with both approaches. Destructive techniques such as fixation, staining, and/or histological sectioning can provide valuable information on cellular interactions within the scaffold, albeit at a limited number of time points. Perhaps more importantly, destructive methods do not permit real-time monitoring of cells under physiological conditions within their intact microenvironment. As an example, it would be impossible to apply standard histological methods to continuously monitor cell proliferation and differentiation within an intact scaffold housed in a bioreactor. Nondestructive techniques, such as microscopy-based optical methods, can be used to image individual cells by labeling them with

fluorescent markers including fluorescent proteins, fluorescent dyes, or quantum dots [39]. However, optical waves in the visible or near-infrared spectrum experience significant scattering and absorption in most tissues and scaffolding materials. Consequently, most optical imaging systems have a limited penetration depth and cannot fully capture the underlying biological processes that occur deep within the tissue scaffold [26].

**Comparison with other optical imaging modalities:** Current optical imaging modalities used to assess tissue-engineered constructs include confocal and nonlinear microscopy [37, 38, 40]. These techniques have become ubiquitous in the field due to their ability to nondestructively image cells and their surrounding matrices through biologically thick tissues. While these techniques are typically applied to cells or scaffolds under standard culturing conditions, several research groups are currently using these methods to perform non-destructive in situ imaging of scaffolds undergoing preconditioning in bioreactors. Kluge et al. recently introduced a bioreactor system capable of applying mechanical stretch to a porous silk fibroin sponge while allowing access to non-destructively image GFP-tagged fibroblasts with a penetration depth of up to 162 μm in the scaffold using confocal microscopy and collagen deposition at a penetration depth of up to 200 μm using nonlinear microscopy [12]. In a similar manner, Nicklason et al. used a nonlinear optical microscope to assess collagen deposition at penetration depths of up to 135 μm within smooth muscle cell-seeded poly (glycolic acid) vessel scaffolds housed within a specialized pulsatile bioreactor undergoing preconditioning [41]. These studies demonstrate that while various advanced microscopy methods can be used for non-destructive scaffold assessment, such imaging modalities cannot maintain single-cell-level resolution beyond the limit of 100-200 μm in turbid biological tissues and scaffolds. Fundamentally, this constraint is due to the fact that engineered tissue scaffolds typically require very high porosities (i.e. electrospun scaffolds [55, 47, 56, 57]) for cell migration and overall colonization of the scaffold. As a result, scaffolds tend to induce very strong optical scattering and are consequently highly opaque. With a limited imaging depth, the methods reported in Ref. [12, 41] may not be suitable for the evaluation of a clinically relevant vascular graft, where the graft must possess sufficient thickness to maintain structural integrity in the presence of pulsatile blood flow.

The imaging method presented in this demonstrates the potential of using fiber-guided light to locally excite fluorescent cells to produce mapped images in highly scattering scaffolds. Our study using GFP-tagged ECs on electrospun PDLLA scaffolds showed that the penetration depth and the

imaging resolution of the scanning fiber method compared favorably with confocal microscopy. More specifically, the confocal microscopy results in Fig. 6.6 displayed a greatly diminished resolution at a scaffold thickness of 100 μm. Furthermore, at imaging depths of 230 and 460 μm, the confocal microscope was unable to identify fluorescent cells through the scaffold and failed to generate the spatial distribution of GFP-labeled ECs on scaffold lumen. Therefore, in terms of imaging depth, our imaging method is superior to confocal laser scanning microscopy, which is one of the state of the art imaging methods for tissue engineering research.

Current optical imaging methodologies are not only limited by penetration depth, but also by the short working distances of their optical objectives, which typically range from hundreds of microns to a few millimeters. With such short working distances, it requires a specialized bioreactor design in order to place a tissue scaffold close enough to the objective to perform imaging. The scanning fiber imaging method has a very large working distance that can reach up to 8 cm. This distance can be easily extended using commercially available long distance objectives, since the method is based on collecting diffused fluorescence light emitted from the scaffold. This practical advantage can be particularly useful for preconditioning studies that require a larger distance between the objective and the tissue scaffold. In contrast, advanced imaging methods such as confocal and non-linear microscopy depend critically on using high numerical aperture objectives with very short working distances. For example, the 10X objective we used for confocal imaging in this study has a short working distance of 2 mm and could not be used to image the PDLLA scaffold sealed within the parallel plate bioreactor. Consequently, the results of imaging studies in Fig. 6.6 had to be carried out in a petri dish with a 170 micron glass slide. Only in this configuration could the sample be placed close enough to the objective for imaging.

**Future work:** The data presented here shows that currently, the imaging method can monitor fluorescent-labeled cells in vascular scaffolds only in a two-dimensional configuration. This technique is appropriate for endothelium and epithelium monolayers, seen in a large number of other tissues and organs, and critical for their proper functions. Consequently, our method is uniquely suited for the study of hollow cavity organs and structures such as blood vessels, intestine, urogenital tract, etc. However, this limitation is not a fundamental constraint and can potentially be circumvented by using more sophisticated signal processing and tomographical reconstruction techniques. For example, we have developed several fluorescence tomography techniques capable of reconstructing three-dimensional distributions of fluorophores in various scaffolds and animal

models. Such methods can potentially be combined with signal processing reported in Ref. [58] to achieve three-dimensional tomographical reconstruction. For tissues and scaffolds that possess significant heterogeneity, we may account for complex scaffold geometry and non-uniform optical parameters by using the tomographical technique discussed in Ref. [59].

# Conclusion

In this work, we have developed a novel imaging method that is capable of nondestructive and dynamic imaging of fluorescent cells located inside an optically opaque vascular scaffold housed within bioreactors. The scanning fiber imaging method is based on the targeted excitation of individual cells, capturing the emitted fluorescence through the scaffold, and producing a mapped image based on the position of the excitation light. Extensive testing has been performed to ensure that the mapped images provide cellular distribution and morphological information with high accuracy while imaging *through* the optically opaque scaffold. Furthermore, the method demonstrates an imaging penetration depth of greater than 3 TMFPs through the electrospun PDLLA scaffold, which significantly exceeded what can be achieved using confocal microscopy. We envision that this imaging modality will advance our understanding of the complex process of neotissue development and remodeling *in vitro* in a nondestructive manner. Building upon the dynamic imaging capabilities, we intend to further develop this technology to assess bioengineered vascular grafts during *in vivo* tissue engineering studies.

# Bibliography


[1] R.M. Nerem and A. Sambanis. Tissue engineering: from biology to biological substitutes. *Tissue Engineering*, 1(1):3–13, 1995.

[2] A. Atala, S.B. Bauer, S. Soker, J.J. Yoo, and A.B. Retik. Tissue-engineered autologous bladders for patients needing cystoplasty. *The Lancet*, 367(9518):1241–1246, 2006.

[3] C.T. Laurencin and J.W. Freeman. Ligament tissue engineering: an evolutionary materials science approach. *Biomaterials*, 26(36):7530–7536, 2005.

[4] A. Raya-Rivera, D.R. Esquiliano, J.J. Yoo, E. Lopez-Bayghen, S. Soker, and A. Atala. Tissue-engineered autologous urethras for patients who need reconstruction: an observational study. *The Lancet*, 2011.

[5] D.L. Elbert. Bottom-up tissue engineering. *Current Opinion in Biotechnology*, 2011.

[6] S. Yang, K.F. Leong, Z. Du, and C.K. Chua. The design of scaffolds for use in tissue engineering. part ii. rapid prototyping techniques. *Tissue Engineering*, 8(1):1–11, 2002.

[7] I. Martin, D. Wendt, and M. Heberer. The role of bioreactors in tissue engineering. *TRENDS in Biotechnology*, 22(2):80–86, 2004.

[8] R. Sodian, T. Lemke, C. Fritsche, S.P. Hoerstrup, P. Fu, E.V. Potapov, H. Hausmann, and R. Hetzer. Tissue-engineering bioreactors: a new combined cell-seeding and perfusion system for vascular tissue engineering. *Tissue engineering*, 8(5):863–870, 2002.

[9] A.S. Goldstein and G. Christ. Functional tissue engineering requires bioreactor strategies. *Tissue Engineering Part A*, 15(4):739–740, 2009.

[10] Laura E. Niklason Angela H. Huang. Engineering biological-based vascular grafts using a pulsatile bioreactor. *J Vis Exp*, (52), 2011.

[11] P. Thevenot, A. Nair, J. Dey, J. Yang, and L. Tang. Method to analyze three-dimensional cell distribution and infiltration in degradable scaffolds. *Tissue Engineering Part C: Methods*, 14(4):319–331, 2008.

[12] J.A. Kluge, G.G. Leisk, R.D. Cardwell, A.P. Fernandes, M. House, A. Ward, A.L. Dorfmann, and D.L. Kaplan. Bioreactor system using noninvasive imaging and mechanical stretch for biomaterial screening. *Annals of biomedical engineering*, pages 1–13, 2011.

[13] S.K. Yazdani, B.W. Tillman, J.L. Berry, S. Soker, and R.L. Geary. The fate of an endothelium layer after preconditioning. *Journal of Vascular Surgery*, 51(1):174–183, 2010.

[14] V.L. Roger, A.S. Go, D.M. Lloyd-Jones, E.J. Benjamin, J.D. Berry, W.B. Borden, D.M. Bravata, S. Dai, E.S. Ford, C.S. Fox, et al. Executive summary: Heart disease and stroke statistics–2012 update: A report from the american heart association. *Circulation*, 125(1):188, 2012.

[15] DT Priest, J. Cheetham, AL Regner, L. Mitchell, LV Soderholm, Y. Tamzali, and NG Ducharme. Dynamic respiratory endoscopy of standardbred racehorses during qualifying races. *Equine Veterinary Journal*, 2012.

[16] Y. Uchida. Coronary angioscopy: From tissue imaging to molecular imaging. *Current Cardiovascular Imaging Reports*, 2(4):284–292, 2009.

[17] D.H. Bagley. Ureteroscopic diagnosis and treatment of upper urinary tract neoplasms. *Smith's Textbook of Endourology*, pages 436–452, 2012.

[18] K. Lin, W. Zheng, and Z. Huang. Integrated autofluorescence endoscopic imaging and pointwise spectroscopy for real-time in vivo tissue measurements. *Journal of biomedical optics*, 15:040507, 2010.

[19] V.X.D. Yang, M. Gordon, S. Tang, N. Marcon, G. Gardiner, B. Qi, S. Bisland, E. Seng-Yue, S. Lo, and J. Pekar. High speed, wide velocity dynamic range doppler optical coherence tomography (part iii): in vivo endoscopic imaging of blood flow in the rat and human gastrointestinal tracts. *Optics Express*, 11(19):2416–2424, 2003.

[20] D. Moussata, M. Goetz, A. Gloeckner, M. Kerner, B. Campbell, A. Hoffman, S. Biesterfeld, B. Flourie, J.C. Saurin, and P.R. Galle. Confocal laser endomicroscopy is a new imaging modality for recognition of intramucosal bacteria in inflammatory bowel disease in vivo. *Gut*, 60(1):26–33, 2011.

[21] M.T. Myaing, D.J. MacDonald, and X. Li. Fiber-optic scanning two-photon fluorescence endoscope. *Optics letters*, 31(8):1076–1078, 2006.

[22] C.J. Engelbrecht, R.S. Johnston, E.J. Seibel, and F. Helmchen. Ultra-compact fiber-optic two-photon microscope for functional fluorescence imaging in vivo. *Optics Express*, 16(8):5556–5564, 2008.

[23] P. Kim, E. Chung, H. Yamashita, K.E. Hung, A. Mizoguchi, R. Kucherlapati, D. Fukumura, R.K. Jain, and S.H. Yun. In vivo wide-area cellular imaging by side-view endomicroscopy. *Nature methods*, 7(4):303–305, 2010.

[24] W. Drexler. Ultrahigh-resolution optical coherence tomography. *Journal of Biomedical Optics*, 9:47, 2004.

[25] C. Xu, J. Ye, D.L. Marks, and S.A. Boppart. Near-infrared dyes as contrast-enhancing agents for spectroscopic optical coherence tomography. *Optics letters*, 29(14):1647–1649, 2004.

[26] V. Ntziachristos. Going deeper than microscopy: the optical imaging frontier in biology. *Nature methods*, 7(8):603–614, 2010.

[27] H.F. Zhang, K. Maslov, G. Stoica, and L.V. Wang. Functional photoacoustic microscopy for high-resolution and noninvasive in vivo imaging. *Nature biotechnology*, 24(7):848–851, 2006.

[28] X. Wang, Y. Pang, G. Ku, X. Xie, G. Stoica, L.V. Wang, et al. Noninvasive laser-induced photoacoustic tomography for structural and functional in vivo imaging of the brain. *Nature biotechnology*, 21(7):803–806, 2003.

[29] L.V. Wang. Multiscale photoacoustic microscopy and computed tomography. *Nature photonics*, 3(9):503–509, 2009.

[30] R. Ma, A. Taruttis, V. Ntziachristos, and D. Razansky. Multispectral optoacoustic tomography (msot) scanner for whole-body small animal imaging. *Optics express*, 17(24):21414–21426, 2009.

[31] L.V. Wang. Prospects of photoacoustic tomography. *Medical physics*, 35:5758, 2008.

[32] RW Resandt, HJB Marsman, R. Kaplan, J. Davoust, EHK Stelzer, and R. Stricker. Optical fluorescence microscopy in three dimensions: microtomoscopy. *Journal of microscopy*, 138(1):29–34, 1985.

[33] E. Betzig, JK Trautman, TD Harris, JS Weiner, and RL Kostelak. Breaking the diffraction barrier: optical microscopy on a nanometric scale. *Science*, 251(5000):1468–1470, 1991.

[34] A. Corlu, R. Choe, T. Durduran, M.A. Rosen, M. Schweiger, S.R. Arridge, M.D. Schnall, and A.G. Yodh. Three-dimensional in vivo fluorescence diffuse optical tomography of breast cancer in humans. *Optics Express*, 15(11):6696–6716, 2007.

[35] J. Sharpe, U. Ahlgren, P. Perry, B. Hill, A. Ross, J. Hecksher-Sørensen, R. Baldock, and D. Davidson. Optical projection tomography as a tool for 3d microscopy and gene expression studies. *Science*, 296(5567):541–545, 2002.

[36] G. Wang, Y. Li, and M. Jiang. Uniqueness theorems in bioluminescence tomography. *Medical physics*, 31:2289, 2004.

[37] J.T. Keyes, D.G. Haskett, U. Utzinger, M. Azhar, and J.P.V. Geest. Adaptation of a planar microbiaxial optomechanical device for the tubular biaxial microstructural and macroscopic characterization of small vascular tissues. *Journal of biomechanical engineering*, 133:075001, 2011.

[38] I. Georgakoudi, W.L. Rice, M. Hronik-Tupaj, and D.L. Kaplan. Optical spectroscopy and imaging for the noninvasive evaluation of engineered tissues. *Tissue Engineering Part B: Reviews*, 14(4):321–340, 2008.

[39] V. Ntziachristos. Fluorescence molecular imaging. *Annu. Rev. Biomed. Eng.*, 8:1–33, 2006.

[40] K. Schenke-Layland, I. Riemann, U.A. Stock, and K. König. Imaging of cardiovascular structures using near-infrared femtosecond multiphoton laser scanning microscopy. *Journal of biomedical optics*, 10:024017, 2005.

[41] L.E. Niklason, A.T. Yeh, E.A. Calle, Y. Bai, A. Valentin, and J.D. Humphrey. Enabling tools for engineering collagenous tissues integrating bioreactors, intravital imaging, and biomechanical modeling. *Proceedings of the National Academy of Sciences*, 107(8):3335, 2010.

[42] LD Wright, RT Young, T. Andric, and JW Freeman. Fabrication and mechanical characterization of 3d electrospun scaffolds for tissue engineering. *Biomedical Materials*, 5:055006, 2010.

[43] L. Ji and K. Gallo. An agreement coefficient for image comparison. *Photogrammetric engineering and remote sensing*, 72(7):823, 2006.

[44] L.E. Freed, G. Vunjak-Novakovic, R.J. Biron, D.B. Eagles, D.C. Lesnoy, S.K. Barlow, and R. Langer. Biodegradable polymer scaffolds for tissue engineering. *Nature Biotechnology*, 12(7):689–693, 1994.

[45] D.W. Hutmacher. Scaffolds in tissue engineering bone and cartilage. *Biomaterials*, 21(24):2529–2543, 2000.

[46] S.J. Hollister. Porous scaffold design for tissue engineering. *Nature materials*, 4(7):518–524, 2005.

[47] W.J. Li, C.T. Laurencin, E.J. Caterson, R.S. Tuan, and F.K. Ko. Electrospun nanofibrous structure: a novel scaffold for tissue engineering. *Journal of biomedical materials research*, 60(4):613–621, 2002.

[48] S.J. Lee, J.J. Yoo, G.J. Lim, A. Atala, and J. Stitzel. In vitro evaluation of electrospun nanofiber scaffolds for vascular graft application. *Journal of Biomedical Materials Research Part A*, 83(4):999–1008, 2007.

[49] S.J. Lee, J. Liu, S.H. Oh, S. Soker, A. Atala, and J.J. Yoo. Development of a composite vascular scaffolding system that withstands physiological vascular conditions. *Biomaterials*, 29(19):2891–2898, 2008.

[50] B.W. Tillman, S.K. Yazdani, S.J. Lee, R.L. Geary, A. Atala, and J.J. Yoo. The in vivo stability of electrospun polycaprolactone-collagen scaffolds in vascular reconstruction. *Biomaterials*, 30(4):583–588, 2009.

[51] V. Barron, E. Lyons, C. Stenson-Cox, PE McHugh, and A. Pandit. Bioreactors for cardiovascular cell and tissue growth: a review. *Annals of biomedical engineering*, 31(9):1017–1030, 2003.

[52] G. Orlando, K.J. Wood, P. De Coppi, P.M. Baptista, K.W. Binder, K.N. Bitar, C. Breuer, L. Burnett, G. Christ, and A. Farney. Regenerative medicine as applied to general surgery. *Annals of Surgery*, 2012.

[53] P. Macchiarini, P. Jungebluth, T. Go, M. Asnaghi, L.E. Rees, T.A. Cogan, A. Dodson, J. Martorell, S. Bellini, and P.P. Parnigotto. Clinical transplantation of a tissue-engineered airway. *The Lancet*, 372(9655):2023–2030, 2008.

[54] M.R. Kreke and A.S. Goldstein. Hydrodynamic shear stimulates osteocalcin expression but not proliferation of bone marrow stromal cells. *Tissue engineering*, 10(5-6):780–788, 2004.

[55] MP Lutolf and JA Hubbell. Synthetic biomaterials as instructive extracellular microenvironments for morphogenesis in tissue engineering. *Nature biotechnology*, 23(1):47–55, 2005.

[56] Z. Ma, M. Kotaki, R. Inai, and S. Ramakrishna. Potential of nanofiber matrix as tissue-engineering scaffolds. *Tissue Engineering*, 11(1-2):101–109, 2005.

[57] B.M. Whited, J.R. Whitney, M.C. Hofmann, Y. Xu, and M.N. Rylander. Pre-osteoblast infiltration and differentiation in highly porous apatite-coated plla electrospun scaffolds. *Biomaterials*, 2010.

[58] A.X. Cong, M.C. Hofmann, W. Cong, Y. Xu, and G. Wang. Monte carlo fluorescence microtomography. *Journal of Biomedical Optics*, 16:070501, 2011.

[59] A. Cong and G. Wang. A finite-element-based reconstruction method for 3d fluorescence tomography. *Optics Express*, 13(24):9847–9857, 2005.